LEAST-SQUARES JOINT IMAGING OF MULTIPLES AND PRIMARIES

A DISSERTATION
SUBMITTED TO THE DEPARTMENT OF GEOPHYSICS
AND THE COMMITTEE ON GRADUATE STUDIES
OF STANFORD UNIVERSITY
IN PARTIAL FULFILLMENT OF THE REQUIREMENTS
FOR THE DEGREE OF
DOCTOR OF PHILOSOPHY

Morgan Parker Brown
May 2004

I certify that I have read this dissertation and that in my opinion it is fully adequate, in scope and quality, as a dissertation for the degree of Doctor of Philosophy.

Biondo L. Biondi
(Principal Adviser)

I certify that I have read this dissertation and that in my opinion it is fully adequate, in scope and quality, as a dissertation for the degree of Doctor of Philosophy.

Jon F. Claerbout

I certify that I have read this dissertation and that in my opinion it is fully adequate, in scope and quality, as a dissertation for the degree of Doctor of Philosophy.

Gary Mavko

Approved for the University Committee on Graduate Studies:

Abstract

Current exploration geophysics practice still regards multiple reflections as noise, although multiples often contain considerable information about the earth's angle-dependent reflectivity that primary reflections do not. To exploit this information, multiples and primaries must be combined in a domain in which they are comparable, such as in the prestack image domain. However, unless the multiples and primaries have been pre-separated from the data, crosstalk leakage between multiple and primary images will significantly degrade any gains in the signal fidelity, geologic interpretability, and signal-to-noise ratio of the combined image. Moreover, by dividing the joint imaging process into individual separation and combination steps, each of which may produce biased results, it is difficult to ensure that the combined image honors the recorded data in any quantitative sense.

In this thesis, I present a global linear least-squares algorithm which simultaneously separates multiples from primaries and combines their information. The algorithm, denoted LSJIMP (Least-squares Joint Imaging of Multiples and Primaries), takes as input reflection seismic data with multiples, and outputs a set of images, each of which ideally contains energy only from the primaries or from one type of pegleg multiple. The novelty of the method lies in the three model regularization operators which both discriminate between crosstalk and signal and extend information between multiple and primary images. The LSJIMP method represents generalizations both of prestack algorithms which separate multiples and primaries and those which compensate for incomplete illumination. To better accomplish both goals, the method exploits another, hitherto ignored, source of redundancy in the data – that between primaries and multiples.

While many different types of multiple imaging operators are well-suited for use with the LSJIMP method, in this thesis I utilize an efficient prestack time imaging strategy for multiples which sacrifices accuracy in a complex earth for computational speed and convenience. I derive a variant of the normal moveout (NMO) equation for multiples, called HEMNO, which can image "split" pegleg multiples which arise from a moderately heterogeneous earth. I also derive a series of prestack amplitude compensation operators which when combined with HEMNO, transform pegleg multiples into events are directly comparable – kinematically and in terms of amplitudes – to the primary reflection.

I test my implementation of LSJIMP on two real datasets from the deepwater Gulf of Mexico. The first, a 2-D line in the Mississippi Canyon region, exhibits a variety of strong surface-related pegleg multiples – generated by shallow reflectors and by a tabular salt body – which strongly inhibit interpretation. The second dataset, consisting of portions of two sail lines extracted from a 3-D dataset acquired in the Green Canyon region, contains surface-related multiples which stacking mostly suppresses, but which nontheless inhibit prestack amplitude analysis. In both cases, LSJIMP excellently and non-destructively separates primaries from multiples, and moreover, reliably reconstructs missing traces and illumination gaps.

Preface

All of the figures in this thesis are marked with one of the three labels: [ER], [CR], and [NR]. These labels define to what degree the figure is reproducible from the data directory, source code and parameter files provided on the web version of this thesis [1].

ER denotes Easily Reproducible. The author claims that you can reproduce such a figure from the programs, parameters, and data included in the electronic document. We assume you have a UNIX workstation with Fortran, C, X-Window system, and the software on our CD-ROM at your disposal. Before the publication of the electronic document, someone other than the author tests the author's claim by destroying and rebuilding all ER figures.

CR denotes Conditional Reproducibility. The author certifies that the commands are in place to reproduce the figure if certain resources are available. SEP staff have not attempted to verify the author's certification. To find out what the required resources are, you can inspect a corresponding warning file in the document's result directory. For example, you might need a large or proprietary data set. You may also need a super computer, or you might simply need a large amount of time (20 minutes or more) on a workstation.

NR denotes Non-Reproducible. This class of figure is considered non-reproducible. Figures in this class are scans and artists' drawings. Output of interactive processing are labeled NR.

[1] http://sepwww.stanford.edu/public/docs/sep116

Acknowledgements

When I told my dad (also a geophysicist) of my acceptance to SEP, he warned me that the ride wouldn't be easy. Indeed! To outsiders, many aspects of the group may appear draconian: six SEP seminars per week, two SEP reports per year, computer maintenence/programming, 3-D real data requirement for the Ph.D. However, SEP alumni continually distinguish themselves as researchers, communicators, and independent problem-solvers; all would agree that Jon Claerbout's management formula explains why. I learned the equations of least-squares estimation in college, but Jon taught me how to make it *work*. Jon's a great theoretical mind, but long ago he realized that real data teaches important lessons to theoreticians. Synthetic data can be constructed to de-emphasize any inconvenient aspect of the earth's physics. Real data applies a crucial "reality filter" to research. Jon's insistence that SEP theses contain real data examples adds to student tenures, but it undoubtedly explains the group's long-term success.

Biondo Biondi has a tough job! Our field is fairly mature, corporate research efforts (and dollars) continue to wane, and we have no Arab oil embargo to reinforce the societal importance of finding new reserves (though oil now hovers above $40/barrel). Still, since taking a leadership role at SEP, Biondo has maintained the group's prestige and funding and fostered a diversity of research topics, while distinguishing himself as a world expert in 3-D seismic imaging. Biondo uses an impressive breadth of knowledge to push SEP into fruitful collaborative efforts in geostatistics, earthquake seismology, and environmental geophysics, to name a few. Much of the initial motivation for my thesis project arose from our joint work with Clement Kostov on the imaging of sub-basalt converted shear waves.

Every SEP student has contributed to my thesis, whether through a tough question in seminar or a comment at lunch. Still, I would like to especially thank Bob Clapp for his friendship, geophysical insights, and unprecedented efforts to improve SEP's computer resources. Antoine Guitton has been a good friend and collaborator in classes, research projects, and on many outdoor adventures. Paul Sava kindly provided the depth migration code used in Section 3.0.1. Sergey Fomel's contributions to SEP's inversion and filtering libraries greatly enhanced my ability to generate results. I believe that some of the most fruitful and unexpected scientific discoveries occur when we communicate problems and insights that we would otherwise internalize at our computers. For me, much of that communication came on coffee breaks with many past and present SEP students: Sean Crawley, James Rickett, Antoine Guitton, Alejandro Valenciano, Gabriel Alvarez, Jesse Lomask, Brad Artman, and Bill Curry.

Alfonso Gonzalez suggested I apply to SEP and proved a thoughtful supervisor and mentor at Western Geophysical. Kurt Marfurt helped me considerably to prepare my Ph.D. proposal. Clement Kostov of WesternGeco planted the seed in my head to use "noise" like shear conversions and multiples as signal. Necati Gulunay of CGG expedited the release of the Green Canyon IV 3-D data. Diane Lau deserves special mention for her kindness and eminently competent work as SEP administrator. Professor John Scales of Colorado School of Mines provided encouragement at a critical juncture. I thank Professor Gary Mavko for serving on my reading committee and Professors Norm Sleep and Jef Caers for serving on my defense committee. Norm's insightful comments and careful reading of my thesis proved quite helpful.

I thank my parents for holding their tongues through my grad school rants. Advice from authority figures is cheap, and often destructive. Better to give young minds the resources to figure things out for themselves than to tell them exactly what to do. For thirty years, my parents have given me the love and support which fosters the self-confidence that in turn allows me to make my own decisions. It is odd that I delay my acknowledgement of my wife, Kimberly, to the end, because I sincerely believe that if not for Kim's love and support, this document would not exist! I can only imagine how the peculiar and stressful realities of SEP have percolated down from me down to her. I thank her for having the strength and patience to stick with me through this long, strange trip. Still, we have managed to grow so much as individuals and as a couple over the last five and half years. I look forward to the next fifty!

Contents

Chapter 1

Introduction

Prospecting by the seismic reflection method has revolutionized hydrocarbon exploration. Accurate 3-D reflection seismic imaging of complex structures (along with horizontal drilling) has increased success rates to the point where exploration and production in thousands of feet of water is now often economically feasible. This success, however, appears to fly in the face of common sense. Despite an inherently noisy earth, weak reflected signal, deep reservoirs, and a complex wavefield, seismic images constructed with singly-reflected P-waves (henceforth, "primary reflections" or "primaries") alone often suffice to plan drilling activities.

Modern marine seismic acquisition generally yields higher quality recorded data than terrestrial acquisition. Marine towed-streamer surveys sample the wavefield densely, regularly, and at a relatively low cost. Marine data is immune from a variety of factors which combine to degrade terrestrial data quality: a non-flat acquisition datum, near-surface inhomogeneity, and strong surface waves. However, the water column's relative homogeneity and the near-perfect reflectivity at the water's surface almost always produce observable multiply-reflected P-waves (henceforth, "multiple reflections" or "multiples"). Multiples often erect the most significant impediment to the successful construction and interpretation of an image of the primaries, especially in regions with anomalously strong reflectors (e.g., "hard" water bottom or salt bodies). Multiple suppression techniques have, by necessity, advanced contemporaneously with reflection imaging for fifty years.

Despite its nuisance, however, energy from multiples penetrates deeply enough into the earth to illuminate the prospect zone. In this sense, the multiples can be viewed as perfectly viable signal, rather than as noise. Moreover, since they illuminate different angular ranges and reflection points, a primary and its multiples are more than simply redundant. In theory and in practice, multiples provide subsurface information not found in the primaries.

To actually exploit the information provided by multiples, the multiples and primaries must first be mapped into a domain where they are directly comparable, and then combined in some fashion. Imaging algorithms like migration reduce the signal to a compact form by removing the effects of wave propagation through a the overburden. Additionally, if the prestack images are arranged in angle-domain common-image gathers (see Sava and Fomel (2003) for a review), the events can be analyzed for angle-dependent phenomenon. We conclude, therefore that the prestack image domain, and in particular, the angle domain, is the best one in which to integrate the information contained in the multiples and primaries.

An important class of multiple suppression techniques create from the data a "model" of the multiples, which may then be adaptively subtracted from the data. Many of these algorithms use wavefield extrapolation to "add a multiple bounce" to recorded data, and thus transform primaries into an estimate of the multiples (Morley, 1982; Berryhill and Kim, 1986; Wiggins, 1988; Lu et al., 1999; Riley and Claerbout, 1976; Tsai, 1985; Verschuur et al., 1992). The imaging of multiples can be viewed roughly as the reverse process of modeling. Prestack imaging of multiples "removes a multiple bounce" from the data and transforms multiples into pseudo-primary events (Berkhout and Verschuur, 2003; Shan, 2003) which can then be imaged using conventional imaging techniques.

Existing migration techniques for multiples perform the reverse modeling process either implicitly or explicitly. Reiter et al. (1991) imaged pegleg multiples with Kirchhoff prestack depth migration. He and Schuster (2003) present a least-squares joint imaging scheme for multiples that uses poststack Kirchhoff depth migration. Yu and Schuster (2001) and Guitton (2002) migrate peglegs with shot-profile depth migration, while Berkhout and Verschuur (1994) used a similar crosscorrelation technique. Shan (2003) uses source-geophone migration after crosscorrelation at the surface. In many ways, however, these techniques fail to fully leverage the valuable information contained in the multiples.

In effect, primaries and each mode of multiple constitute semi-independent measurements of the earth's reflectivity at depth. Unfortunately, these independent measurements are embedded in a single data record. We would like to improve signal-to-noise ratio or fill illumination gaps by averaging the images. However, simple averaging of the raw images (Reiter et al., 1991; Berkhout and Verschuur, 1994; Shan, 2003) encounters two problems, illustrated by Figures 1.1 and 1.2. First, unless the multiple images have undergone an appropriate amplitude correction, the signal events are incommensurable. Secondly, just as multiples constitute noise on the primary image, primaries and higher order multiples constitute noise on the first-order multiple image. The unmodeled events on each image are called "crosstalk" (Claerbout, 1992). Because corresponding crosstalk events on the primary and multiple images are kinematically quite consistent, especially at near offsets, averaging the images may not increase the signal-to-noise ratio or improve signal fidelity.

The previous paragraph underscores the main obstacle facing algorithms which attempt to jointly image multiples and primaries: while multiples provide additional information about the earth's reflectivity, we cannot exploit it unless we separate the individual modes. Cleanly separating a variety of different multiple modes from prestack data is both expensive and difficult. Moreover, by casting mode separation as a preprocessing step, as is the norm, we may bias the amplitudes in the separated modes and thus inhibit the integration of primaries and multiples.

In this thesis I introduce the LSJIMP (Least-squares Joint Imaging of Multiples and Primaries) method, which solves the separation and integration problems simultaneously, as a global least-squares inversion problem. The model space of the inverse problem, as illustrated in Figure 1.3, contains a collection of images, with the energy from each mode partitioned into one, and only one image. Moreover, each image has a special form: because the forward modeling operator contains appropriate amplitude correction operators, the signal events in multiple and primary images are directly comparable, in terms of both kinematics and amplitudes.

Minimization of the modeling error ($\mathbf{d} - \mathbf{d}_{\text{mod}}$ in Figure 1.3) alone is an ill-posed problem. Forward-modeled crosstalk is indistinguishable from forward-modeled signal. I devise three model regularization operators which discriminate between crosstalk and signal and thereby

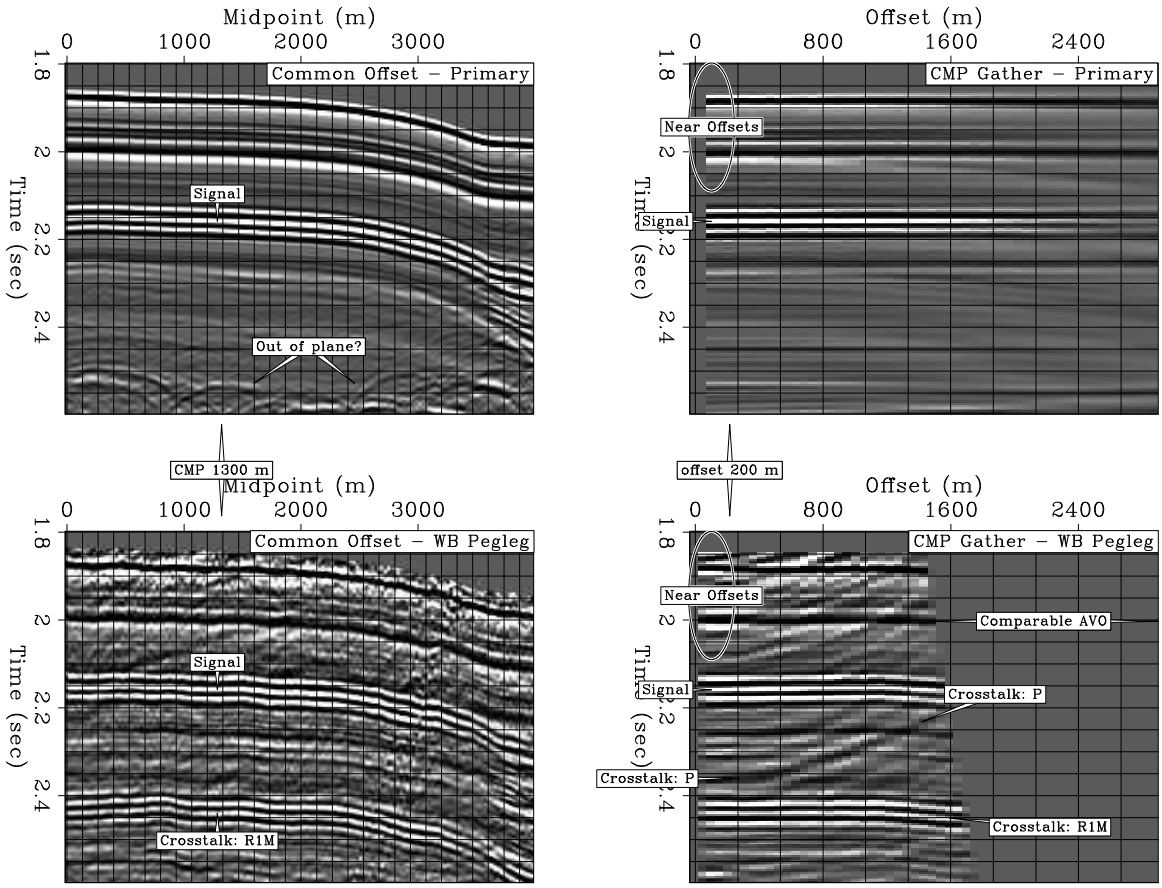

Figure 1.1: Common-offset section and common-midpoint (CMP) gather from 2-D field data example after normal moveout (NMO) for primaries (left panels) and a particular prestack, true relative amplitude imaging method for pegleg multiples (Section 2.2). Signal events are consistent between all panels, both kinematically and in terms of amplitudes. The multiples provide near offset information not found in the primaries. However, the multiple image contains crosstalk events – overcorrected primaries ("P") and multiples from other reflectors ("R1M") – that inhibit simple averaging of the multiple and primary images. The crosstalk events shown here are, however, inconsistent between images, and to some extent curved with respect to offset, and can thus be distinguished from signal events, which are both flat and consistent between images. intro-gulf-schem [CR,M]

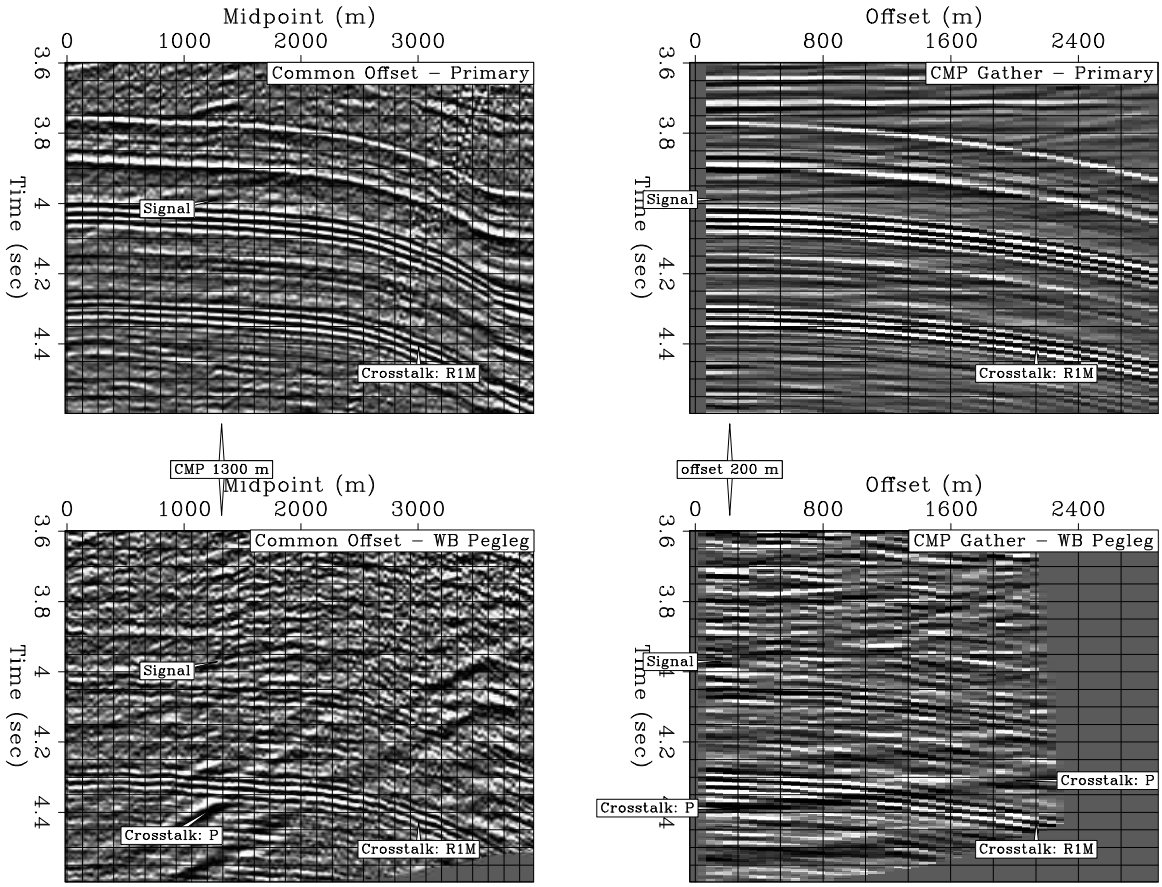

Figure 1.2: Same format as Figure 1.1, but taken from deeper in the section, after the arrival of the first seabed multiple. Weak signal events are visible on both images, but corresponding crosstalk events (e.g., "R1M") are generally consistent between images and would greatly inhibit the effectiveness of simple image averaging. However, they are curved with respect to offset, while signal events are flat. intro-gulf-schem-deep [CR,M]

properly segregate energy from each modeled wave mode into its respective image. Figure 1.4 illustrates these discriminants on a field data example. The model regularization operators serve a higher purpose than crosstalk suppression alone, however. By applying differential operators along reflection angle and between images, we can "spread" signal from other angles or images to fill illumination gaps and increase signal fidelity. Furthermore, by exploiting an additional, and hitherto ignored dimension of data redundancy – that between primaries and multiples – we can, with a degree of rigor, solve the integration problem and rightly claim to have solved a "joint imaging" problem.

1.1 Thesis Outline

Chapter 2 introduces the LSJIMP method. The chapter is divided into three sections. In section 2.1 I motivate the LSJIMP inverse problem in general. Generally, as the non-regularized LSJIMP inverse problem is underdetermined, it suffers from non-uniqueness. I describe three model regularization operators which "steer" the LSJIMP minimization toward an optimally crosstalk-free solution which still fits the data. In Section 2.2, I go on to outline my particular implementation of LSJIMP. In section 2.2.2, I show how, in a laterally-homogeneous earth, to create prestack time-domain images of pegleg multiples that are directly comparable, both in terms of kinematics and amplitudes, to the image of the primaries. In a heterogeneous earth, peglegs "split" into multiple arrivals. To account for this phenomenon, in section 2.2.6 I introduce the HEMNO (Heterogeneous Earth NMO Operator), which can independently image each leg of split peglegs in a moderately heterogeneous earth. HEMNO images with a vertical stretch, sacrificing accuracy in a complex earth for the efficiency required to make iterative solutions to the LSJIMP inverse problem computationally tractable.

In Chapter 3 I apply my implementation of LSJIMP to a 2-D seismic line, donated by WesternGeco, and acquired in the deepwater Mississippi Canyon region of the Gulf of Mexico. The data exhibit strong surface-related multiples from a variety of multiple generators, and prove challenging for all existing methods to attenuate. LSJIMP demonstrates the ability to cleanly separate multiples and primaries, even in regions with moderate geologic complexity.

In Chapter 4 I outline the extension of the LSJIMP method to 3-D data. To minimize

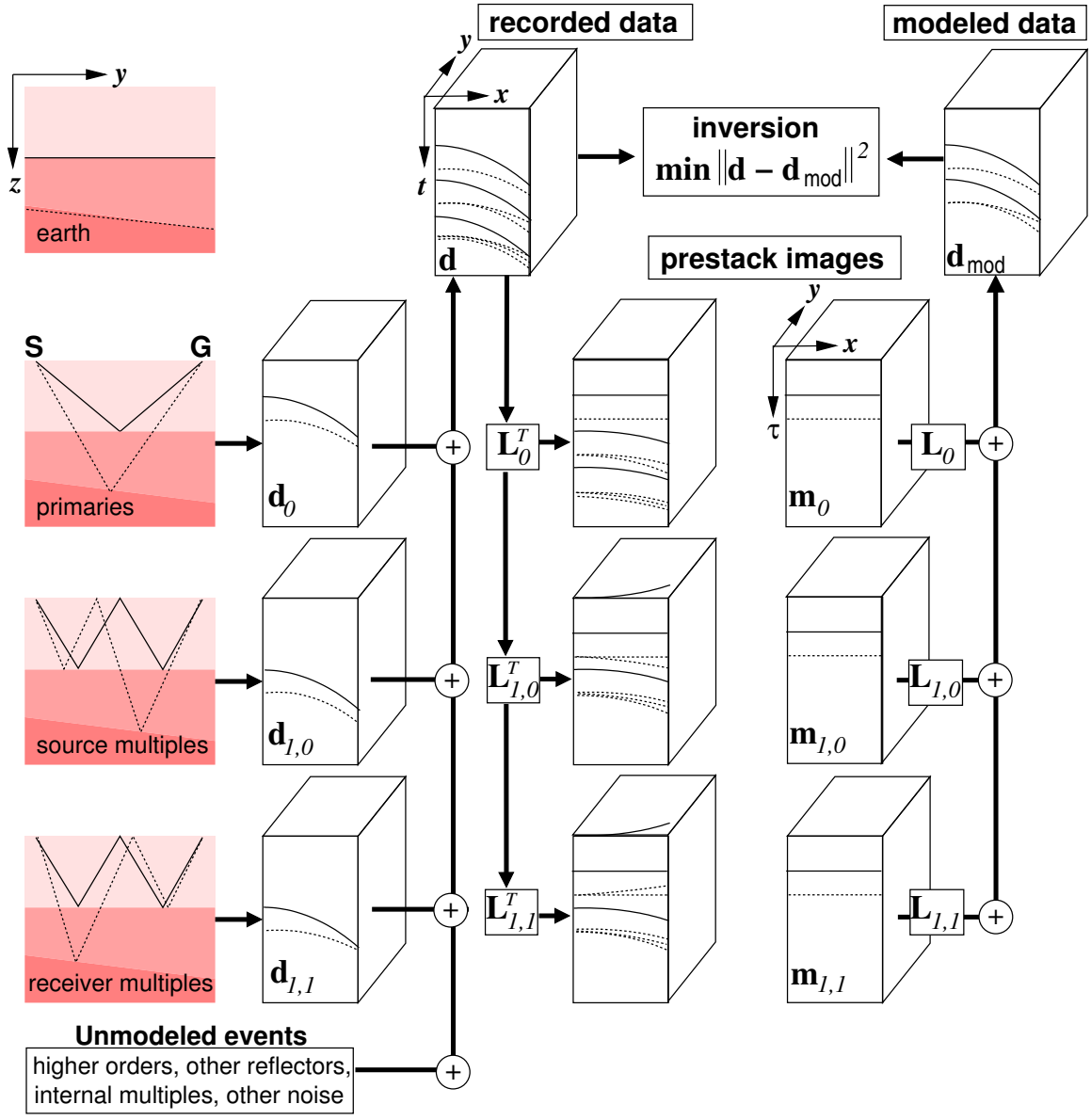

Figure 1.3: LSJIMP schematic. Assume that the recorded data consist of primaries and pegleg multiples. Prestack imaging alone (applying adjoint of modeling operator $\mathbf{L}_{i,k}$) focuses signal events in zero-offset traveltime (or depth) and offset (or reflection angle), but leaves behind crosstalk events. If the $\mathbf{m}_{i,k}$ images contain only signal, then we can model all the events in the data that we desire. The LSJIMP inversion suppresses crosstalk and endeavors to fit the recorded data in a least-squares sense. The model regularization operators used to suppress crosstalk simultaneously enable LSJIMP to exploit the intrinsic redundancy between and within the images to increase signal fidelity. intro-schem-LSJIMP-seg [NR]

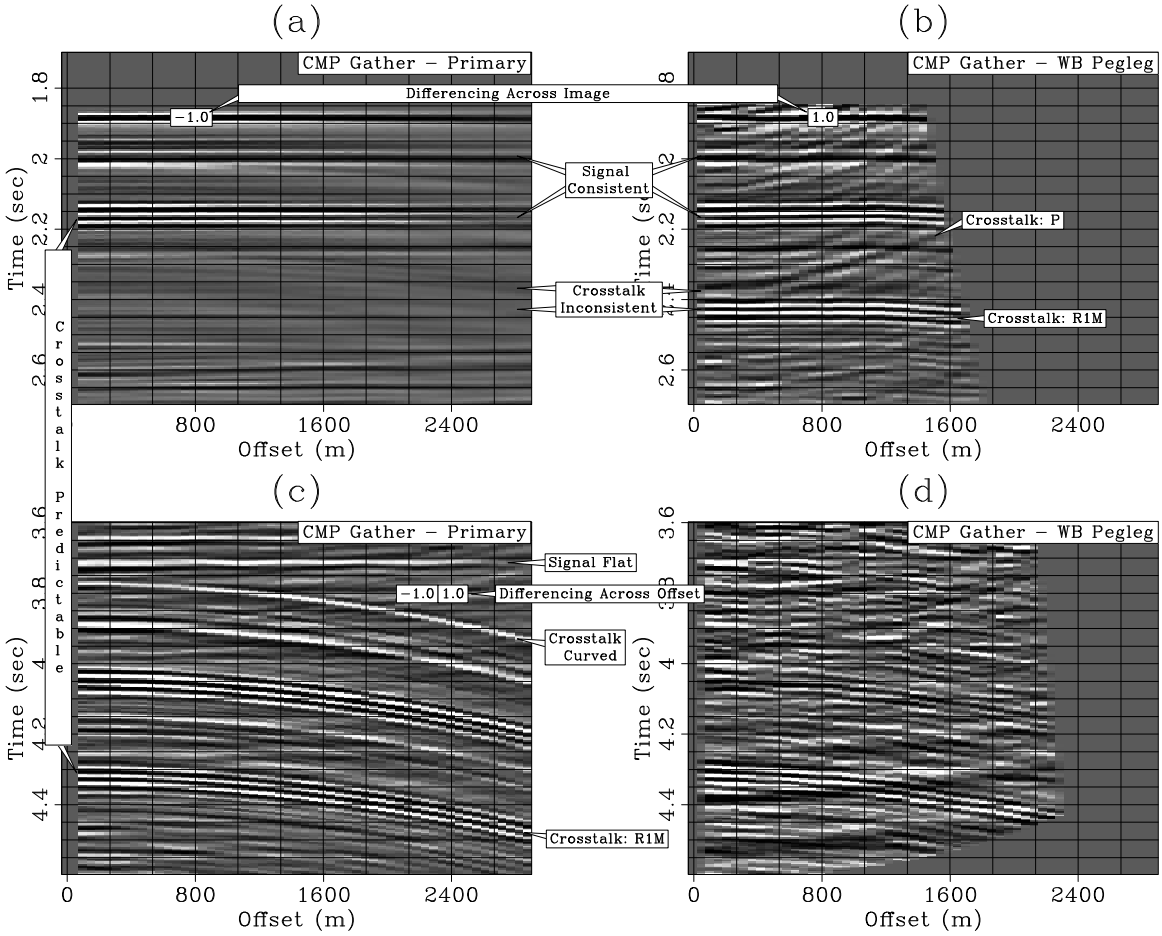

Figure 1.4: Illustration of intrinsic redundancy within and between prestack images of primaries (panels (a) and (c)) and peglegs (panels (b) and (d)), and the regularization schemes used by LSJIMP to exploit this redundancy to suppress crosstalk, increase signal fidelity, and fill illumination gaps. All panels are CMP gathers from the same midpoint, but the upper and lower panels zoom into small portions of the time axis for viewing purposes. Between panels (a) and (b), notice how signal events are consistent (kinematics and amplitudes) between images, while crosstalk events are not. A differencing operator between images increases signal consistency and penalizes crosstalk. On panel (c), notice that signal events are flat with offset, while crosstalk events are generally curved. Differencing between adjacent offsets increases signal fidelity and suppresses crosstalk. Lastly, from panels (a) and (c), notice how we can use signal to predict crosstalk events. The predicted crosstalk can be used as a model penalty weight which penalizes crosstalk. intro-gulf-schem-redun-geo [CR]

acquisition costs, most 3-D marine data are sampled quite sparsely along the crossline source axis, and this sparsity severely hampers some multiple attenuation methods which otherwise excel in 2-D. Because HEMNO images multiples with a vertical stretch, my implementation of LSJIMP is more immune from the crossline sparsity issue.

In Chapter 5 I apply my implementation of LSJIMP to a real 3-D dataset from the Green Canyon region of the Gulf of Mexico. The data were acquired by CGG and contain surface-related multiples, although they are not as strong as those seen in the 2-D Mississippi Canyon data. However, the reflectors in the study area contain fairly strong crossline dips, which challenge many multiple suppression algorithms when the crossline geometry is sparse. Again, my implementation of LSJIMP cleanly separates multiples from primaries. Additionally, this data example showcases LSJIMP's ability to act as an interpolation operator. Due to fast ship speed, the inline offset resolution of common midpoint gathers is coarse. I demonstrate how LSJIMP uses the multiples to simultaneously separate modes, interpolate missing traces, and improve amplitude analysis. A comparison of LSJIMP with least-squares Hyperbolic Radon demultiple illustrates that LSJIMP is an effective and computationally tractable option for 3-D prestack multiple separation.

Chapter 2

2-D Theory

In this chapter I introduce the theory behind the LSJIMP method. The chapter is divided into three sections. In section 2.1 I motivate the LSJIMP inverse problem in general. In Section 2.2, I go on to outline my particular implementation of LSJIMP. In section 2.2.2, I show how, in a laterally-homogeneous earth, to create prestack time-domain images of pegleg multiples that are directly comparable, both in terms of kinematics and amplitudes, to the image of the primaries. In a heterogeneous earth, peglegs "split" into multiple arrivals. To account for this phenonmenon, in section 2.2.6 I introduce the HEMNO (Heterogeneous Earth NMO Operator) equation, which can independently image each leg of split peglegs in a moderately heterogeneous earth.

2.1 The LSJIMP Inverse problem

Figure 1.3 motivates LSJIMP. The Figure assumes that the recorded data is the superposition of primary events and pegleg multiples from the seabed. In effect, the images constructed from the primaries and from each mode of multiple constitute independent measurements of the earth's reflectivity at depth. Unfortunately, these independent measurements are embedded in a single data record. We would like to improve signal-to-noise ratio or fill illumination gaps by averaging the images. However, simple averaging of the raw images encounters two problems.

First, unless the multiple images have undergone an appropriate amplitude correction, the signal events are incommensurable. Secondly, corresponding crosstalk events on the primary and multiple images are kinematically quite consistent, especially at near offsets, meaning that averaging the images will do little to increase the signal-to-noise ratio or signal fidelity.

The previous paragraph underscores the main obstacle facing algorithms which attempt to jointly image multiples and primaries: while multiples provide additional information about the earth's reflectivity, we cannot exploit it unless we separate the individual modes. Cleanly separating a variety of different multiple modes from prestack data is both expensive and difficult. Moreover, by casting mode separation as a preprocessing step, as is the norm, we risk biasing the amplitudes in the separated modes, which could inhibit the integration.

LSJIMP solves the separation and integration problems simultaneously, as a global least-squares inversion problem. The model space, as illustrated in Figure 1.3, contains a collection of images, with the energy from each mode partitioned into one, and only one image. Moreover, each image has a special form: because the forward modeling operator contains appropriate amplitude correction operators the signal events in multiple and primary images are directly comparable, in terms of both kinematics and amplitudes. In order to solve the integration problem, we can apply a model regularization operator which penalizes inconsistency between images, and thus "spreads" signal from one model panel to another, using the multiples to fill gaps in the primary illumination and to increase signal fidelity.

LSJIMP models the recorded data as the superposition of primary reflections and p orders of pegleg multiples from n_{surf} multiple-generating surfaces. An i^{th} order pegleg splits into $i+1$ legs. If we denote the primaries as $\mathbf{d}_0$ and the k^{th} leg of the i^{th} order pegleg from the m^{th} multiple generator as $\mathbf{d}_{i,k,m}$, the modeled data takes the following form:

$$\mathbf{d}_{\text{mod}} = \mathbf{d}_0 + \sum_{i=1}^{p} \sum_{k=0}^{i} \sum_{m=1}^{n_{\text{surf}}} \mathbf{d}_{i,k,m}. \tag{2.1}$$

Figure 1.3 illustrates a simple case, where we model only first-order peglegs from a the seabed ($p = n_{\text{surf}} = 1$).

Other authors have solved a similar least-squares problem. Nemeth et al. (1999) jointly imaged and separated compressional waves and various (non-multiple) embedded coherent noise modes. Guitton et al. (2001) used nonstationary prediction-error filters to model primaries and surface-related multiples, but cast the problem purely in terms of wavefield separation, rather than joint imaging of multiples and primaries.

If we have designed an imaging operator that produces primary and multiple images with consistent signal (kinematics and angle-dependent amplitudes), then we assume that we can model the important events in the data. Let us denote the modeling operator (adjoint to imaging) for primaries $\mathbf{L}_0$ and the image of the primaries $\mathbf{m}_0$. Similarly, for the k^{th} leg of the i^{th} order pegleg from the m^{th} multiple generator, we denote the modeling operator and image $\mathbf{L}_{i,k,m}$ and $\mathbf{m}_{i,k,m}$, respectively. Following Figure 1.3, we can rewrite equation (2.1):

$$\mathbf{d}_{\text{mod}} = \mathbf{L}_0\mathbf{m}_0 + \sum_{i=1}^{p}\sum_{k=0}^{i}\sum_{m=1}^{n_{\text{surf}}}\mathbf{L}_{i,k,m}\mathbf{m}_{i,k,m} \tag{2.2}$$

$$= \mathbf{L}\mathbf{m} \tag{2.3}$$

2.1.1 LSJIMP: Least-squares minimization

The LSJIMP method seeks to optimize the primary and multiple images, $\mathbf{m}$, by minimizing the ℓ_2 norm of the data residual, defined as the difference between the recorded data, $\mathbf{d}$, and the modeled data, $\mathbf{d}_{\text{mod}}$ [equation (2.3)]:

$$\min_{\mathbf{m}} \|\mathbf{d} - \mathbf{L}\mathbf{m}\|^2. \tag{2.4}$$

Minimization (2.4) is under-determined, for many choices of prestack imaging operator, which implies an infinite number of least-squares-optimal solutions. Practically speaking, this problem manifests itself as crosstalk leakage. If (for instance) $\mathbf{m}_0$ contains residual first-order pegleg multiple energy, equation (2.1) will map this energy back into data space, at the position of a first-order multiple. Minimization (2.4) alone cannot distinguish between crosstalk and signal.

Of this infinity of possible $\mathbf{m}$'s, we seek the one which not only fits the recorded data, but

which also has minimum crosstalk leakage and maximum consistency between signal events on different images. In section 2.1.3 I introduce model regularization operators to accomplish both goals.

After the minimization of equation (2.4), theory dictates that the data residual should be independent and identically distributed (iid), or more intuitively, uncorrelated and evenly scaled. Correlated events in the residual imply that the forward model, $\mathbf{L}$, poorly models or fails to model events in the data. Examples of poor scaling might be the loss of reflection strength for deep reflectors, or empty traces. In general we compensate for a correlated or poorly scaled data residual by adding a residual weighting operator, $\mathbf{W_d}$:

$$\min_{\mathbf{m}} \ \|\mathbf{W_d}\,[\mathbf{d}-\mathbf{L}\mathbf{m}]\,\|^2, \tag{2.5}$$

where strictly speaking,

$$\left(\mathbf{W_d}^T\mathbf{W_d}\right)^{-1} = \mathrm{cov}[\mathbf{d}], \tag{2.6}$$

although in my implementation of LSJIMP, outlined in section 2.2, a far simpler choice for $\mathbf{W_d}$ is used.

2.1.2 LSJIMP: Choice of Imaging Operator

The exact form of the modeling operators, $\mathbf{L}_{i,k,m}$, shown in equation (2.3) has not yet been discussed. Any candidate prestack imaging operator for multiples must accomplish two tasks: focus the multiples in time/depth and offset/angle at the position of the primary and correct their amplitude to make the multiples directly comparable to the corresponding primary.

The literature contains many multiple modeling techniques which use wavefield extrapolation to "add a multiple bounce" to recorded data, and thus transform primaries into a model of the multiples, which is then generally adaptively subtracted from the data. These modeling techniques can roughly be divided into earth-model-based (Morley, 1982; Berryhill and Kim, 1986; Wiggins, 1988; Lu et al., 1999) and autoconvolutional (Riley and Claerbout, 1976; Tsai, 1985; Verschuur et al., 1992) approaches. It is possible to reverse the multiple modeling process–in other words, to "remove a multiple bounce" from the data and transform multiples

into pseudo-primary events, which can then be imaged as primaries (Berkhout and Verschuur, 2003; Shan, 2003).

Existing migration techniques for multiples perform the reverse modeling process either explicitly (i.e., using an earth model) or implicitly. Reiter et al. (1991) imaged pegleg multiples with Kirchhoff prestack depth migration. He and Schuster (2003) present a least-squares joint imaging scheme for multiples that uses poststack Kirchhoff depth migration. Yu and Schuster (2001) and Guitton (2002) migrate peglegs with shot-profile depth migration, while Berkhout and Verschuur (1994) used a similar crosscorrelation technique. Shan (2003) uses source-geophone migration after crosscorrelation at the surface. None of these techniques explicitly addresses the issue of amplitudes, beyond a polarity flip.

In this thesis, I use an earth-model-based multiple modeling strategy to simulate the kinematics and angle-dependent amplitude behavior of pegleg multiples. In section 2.2.1 I derive an extension to the normal moveout (NMO) equation for pegleg multiples. In section 2.2.6 I introduce HEMNO (Heterogeneous Earth Multiple NMO Operator), an extension of the NMO equation for multiples, which independently images split peglegs in a moderately heterogeneous earth. In Sections 2.2.2-2.2.5 I derive a series of amplitude correction operators to normalize the angle-dependent reflectivity of imaged multiples to be commensurable with their imaged primaries.

I postpone giving the full motivation for my particular choice of multiple imaging operator, as well as many implementation details until section 2.2. However, we can at this early stage state some important facts which have bearing on how the problem is regularized and how it is implemented computationally. The prestack multiple image, $\mathbf{m}_{i,k,m}$, shown in Figure 1.3, is parameterized by zero-offset traveltime, τ, offset, x, and midpoint, y. However, one important feature of the my combined imaging operator is the fact that it operates on a CMP-by-CMP basis. This underscores the fact that HEMNO applies a vertical stretch, and does not move information across midpoint. The regularization schemes I present also do not operate across midpoint. This implementation allows a coarse-grained parallelization scheme, enabling straightforward parallel computation on a Linux cluster.

2.1.3 Regularization of the LSJIMP Problem

In Sections 2.1.4-2.1.6, I exploit three discriminants between crosstalk and signal to devise model regularization operators. The raw LSJIMP minimization [equation (2.5)] suffers from non-uniqueness. The model regularization operators choose the particular set of primary and multiple images which are optimally free of crosstalk, from an infinite number of possible combinations. Moreover, these operators exploit signal multiplicity–within and between images–to increase signal fidelity and fill illumination gaps/missing traces. Some existing regularized least-squares prestack migration schemes exploit signal multiplicity across reflection angle (Kuehl and Sacchi, 2001; Prucha and Biondi, 2002; Wang et al., 2003). LSJIMP's additional use of multiples to regularize the least-squares imaging problem is novel.

As mentioned in the previous section, my particular implementation of LSJIMP processes each CMP location independently. Therefore, without loss of generality, the regularization terms described in the following sections assume that the prestack multiple images, $\mathbf{m}_{i,k,m}$, are functions of zero-offset traveltime (τ) and offset (x), but not of midpoint. The same logic applies to an image parameterized by depth and reflection angle.

2.1.4 Regularization 1: Differencing between images

Corresponding signal events on all $\mathbf{m}_{i,k,m}(\tau,x)$ are focused at a single τ for all x, and by design, have directly comparable amplitudes. Conversely, corresponding crosstalk events on two model panels (e.g. residual first-order multiples on $\mathbf{m}_0$ and residual second-order multiples on $\mathbf{m}_{1,k,m}$) generally have different residual moveout. While the exact magnitude of the moveout differences depend on the choice of imaging operator, Figure 2.1 illustrates that they generally are small at near offsets, but more pronounced in the presence of subsurface complexity, and at far offsets/reflection angles.

We therefore conclude that at fixed (τ,x), the difference between two $\mathbf{m}_{i,k,m}$ will be relatively small where there is signal, but large where there is crosstalk noise. We now write this

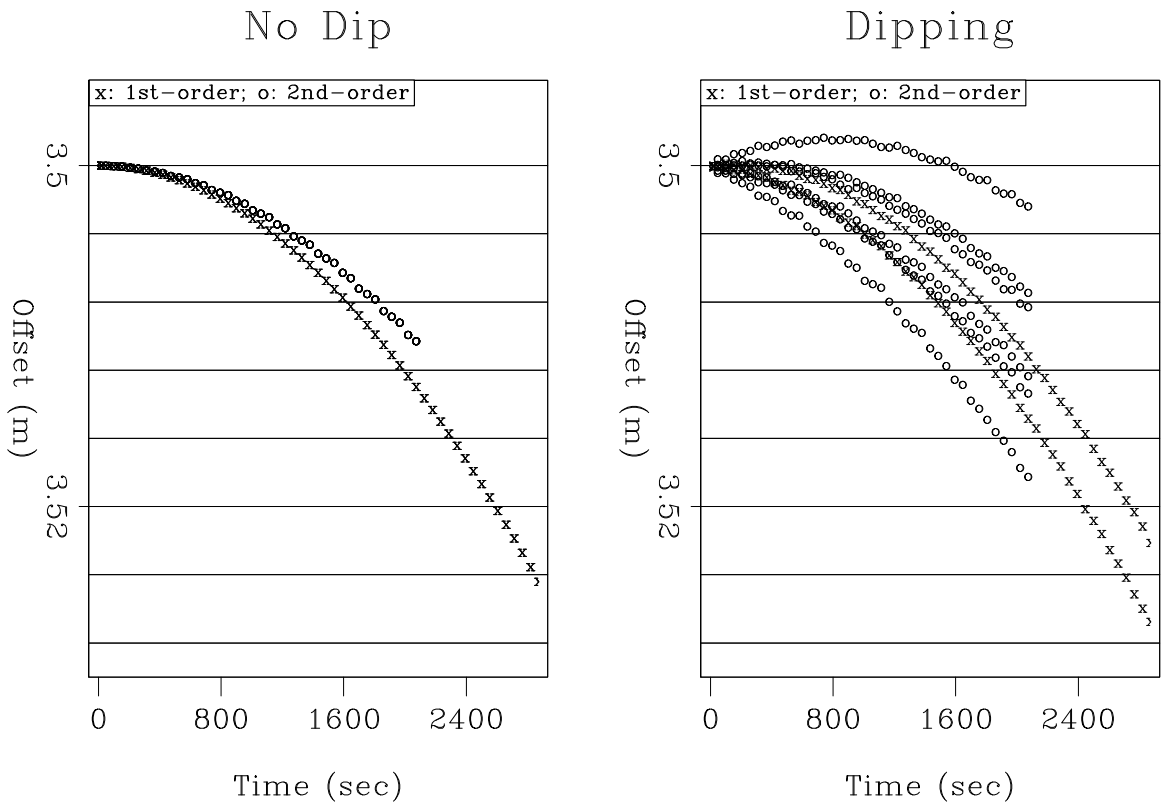

Figure 2.1: Comparison of crosstalk events on primary and first-order multiple images, for my particular choice of multiple imaging operator. "X" indicates position of split first-order pegleg on primary image, $\mathbf{m}_0$. "o" indicates position of the three second-order pegleg events on both $\mathbf{m}_{1,0,1}$ and $\mathbf{m}_{1,1,1}$. Left panel is with no subsurface dip, right has seabed and target reflector dip of 4°. With no dip, corresponding crosstalk events have little differential moveout. A small amount of dip quickly increases differential moveout. theory2d-crossdiff2.gulf [ER]

difference as a model residual:

$$\mathbf{r}_m^{[1]}[j](\tau,x) = \mathbf{m}_j(\tau,x) - \mathbf{m}_{j+1}(\tau,x), \quad \text{where} \quad j = [0, p(p+3)/2]. \tag{2.7}$$

p is the maximum order of multiple included in equation (2.2). Here I have modified the notation a bit and written $\mathbf{m}_j$ rather than $\mathbf{m}_{i,k,m}$ because the difference (2.7) is blind to the order or leg of the pegleg corresponding to $\mathbf{m}_j$; it is simply a straight difference across all the model panels.

As mentioned early in this thesis, a central motivation for LSJIMP is the desire to combine information from the multiple and primary images by averaging. In addition to discriminating against crosstalk, equation (2.7) provides a systematic framework for this averaging. If a signal event on one image is obscured by noise, the noise may not be present on an adjacent image, and equation (2.7) will attenuate it. This regularization enforces a degree of smoothness and consistency between images.

2.1.5 Regularization 2: Differencing across offset

After imaging with the correct velocity, signal events on all $\mathbf{m}_{i,k,m}$ are flat, while crosstalk events have at least some residual curvature, especially at far offsets and in regions with a strong velocity gradient. Provided that the AVO response of the signal changes slowly with offset, the difference (in offset) between adjacent samples of any $\mathbf{m}_{i,k,m}$ will be relatively small where there is signal, but large where there is crosstalk noise. We again cast this difference as a model residual:

$$\mathbf{r}_m^{[2]}[i,k,m](\tau,x) = \mathbf{m}_{i,k,m}(\tau,x) - \mathbf{m}_{i,k,m}(\tau,x+\Delta x). \tag{2.8}$$

2.1.6 Regularization 3: Crosstalk penalty weights

The third and final discriminant between crosstalk and signal exploits the inherent predictability of the crosstalk to suppress it. If we have an estimate of the signal, we can directly model

the expected crosstalk events on each $\mathbf{m}_{i,k,m}$, and construct a model-space weighting function to penalize crosstalk. Unfortunately, unless we employ a nonlinear iteration (see section 2.1.8), we do not, a priori, have this signal estimate. However, between the seabed reflection and the onset of its first multiple, the recorded data contains only primaries (inter-bed multiples and locally-converted shear waves are generally weak), and it is these strong, shallow events that often spawn the most troublesome crosstalk events. Therefore, we can directly model any pegleg multiple arising from a multiple generator with traveltime less than that of the first seabed multiple.

If we define $\mathbf{M}_0$ as an operator that applies a flat mute below twice the zero-offset traveltime of the seabed, and $\mathbf{M}_i$ as a similar operator that mutes above the zero-offset traveltime of the i^{th} multiple generator, then

$$\mathbf{z}_{i,k,m} = \mathbf{L}_{i,k,m}\mathbf{M}_{i,m}\mathbf{M}_0\mathbf{L}_0^T\mathbf{d} \tag{2.9}$$

is a model of the k^{th} leg of the i^{th} order multiple from the m^{th} multiple generator. Each $\mathbf{m}_{i,k,m}$ in equation (2.2) should ideally contain only the k^{th} leg of the i^{th}-order multiple from the m^{th} multiple generator – all other energy is crosstalk. To simulate crosstalk noise in $\mathbf{m}_{i,k,m}$, we apply $\mathbf{L}_{i,k,m}$ to all multiple model panels $\mathbf{z}$ (except $\mathbf{z}_{i,k,m}$) and sum:

$$\mathbf{c}_{l,n,q} = \sum_{j=l_0}^{p}\sum_{k=0}^{j}\sum_{m=1}^{n_{\text{surf}}}\mathbf{L}_{l,n,q}^T\mathbf{z}_{j,k,m}, \text{ where } k \neq n,\ m \neq q \text{ and } l_0 = \begin{cases} 1 & \text{if } l = 0 \\ l & \text{otherwise} \end{cases} \tag{2.10}$$

$\mathbf{c}_{i,k,m}$ is a kinematic model of crosstalk for $\mathbf{m}_{i,k,m}$. It could be used as a traditional multiple model (see section 3.1) and subtracted from the data, but I instead convert each $\mathbf{c}_{i,k,m}$ into a weighting function by taking the absolute value. We can write the model residual corresponding to the third model regularization operator:

$$\mathbf{r}_m^{[3]}[i,k,m](\tau,x) = \left|\mathbf{c}_{i,k,m}(\tau,x)\right|\ \mathbf{m}_{i,k,m}(\tau,x). \tag{2.11}$$

Although the crosstalk weights will likely overlap (and damage) signal to some extent, the signal's flatness and self-consistency between images ensures that regularization operators (2.7) and (2.8) will "spread" redundant information about the primaries from other $\mathbf{m}_{i,k,m}$ and

other offsets to compensate for any losses. Figure 2.2 illustrates the application of the crosstalk weights for the primary image and a multiple image. On panel (a), the primary image, the crosstalk is the obviously curving events. On panel (c), the seabed pegleg image, the crosstalk events are multiples from other multiple generators (e.g., R1M and R2M). Notice that in both cases the unwanted multiples are picked cleanly out of the data, leaving the underlying signal intact.

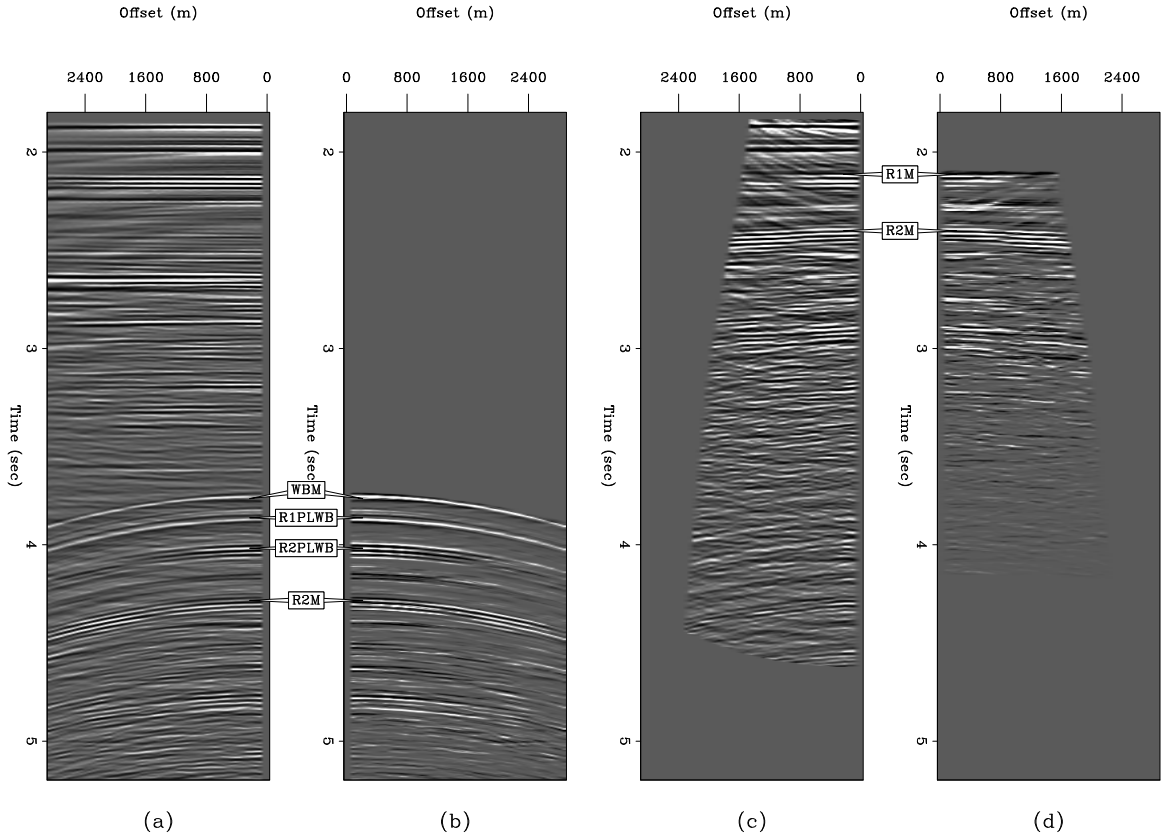

Figure 2.2: Application of crosstalk weights to real CMP after prestack imaging. Panel (a): primary image, $\mathbf{L}_0^T\mathbf{d}$. Panel (b): weighted primary image, $|\mathbf{c}_0|\mathbf{L}_0^T\mathbf{d}$. Panel (c): seabed pegleg image, $\mathbf{L}_{1,0,1}^T\mathbf{d}$. Panel (d): weighted seabed pegleg image, $|\mathbf{c}_{1,0,1}|\mathbf{L}_{1,0,1}^T\mathbf{d}$. $n_{\text{surf}} = 4$ in this case. Prominent crosstalk events are labeled on the various panels. theory2d-crosstalk.gulf [CR,M]

2.1.7 Combined LSJIMP Data and Model Residuals

To effect the final step of LSJIMP, the estimation of the optimal set of $\mathbf{m}_{i,k,m}$, we minimize a quadratic objective function which consists of the sum of the weighted ℓ_2 norms of the data residual [equation (2.5)] and of the three model residuals [equations (2.7), (2.8), and (2.11)]:

$$\min_{\mathbf{m}} Q(\mathbf{m}) = \|\mathbf{W_d}\,[\mathbf{Lm}-\mathbf{d}]\|^2 + \epsilon_1^2\|\mathbf{r}_m^{[1]}\|^2 + \epsilon_2^2\|\mathbf{r}_m^{[2]}\|^2 + \epsilon_3^2\|\mathbf{r}_m^{[3]}\|^2. \qquad (2.12)$$

ϵ_1, ϵ_2, and ϵ_3 are scalars which balance the relative weight of the three model residuals with the data residual. For the large scale problems endemic to seismic imaging, the conjugate gradient method is a logical choice to minimize $Q(\mathbf{m})$.

2.1.8 LSJIMP Nonlinear Iterations

Proponents of so-called "full-waveform inversion" (Tarantola, 1984) seek to solve an ambitious nonlinear inverse problem. In the context of reflection seismology, full-waveform techniques seek to invert a relation of the following qualitative form:

$$\text{recorded data} \quad = \quad \mathcal{L}\,(\text{density, velocity})$$

Most generally, the operator $\mathcal{L}$ is elastic two-way wave equation modeling, although making the acoustic assumption simplifies matters. In both cases, the modeling operator is nonlinearly dependent on the earth model to be estimated. For many reasons (including, but not limited to: computational expense, model non-uniqueness/nullspace, and sensitivity to starting model), full-waveform techniques are rarely applied successfully in today's conventional seismic processing environment. The LSJIMP method can be abstracted in a similar qualitative fashion, using the notation of the previous sections:

$$\begin{aligned} \mathbf{L} &\Leftarrow \text{velocity, reflection coefficient, crosstalk model} \\ \mathbf{d} &= \mathbf{Lm} \end{aligned}$$

Quantities like imaging velocity, the measured reflection coefficient of the multiple generators, and the crosstalk model are assumed to be fixed. Some LSJIMP implementations might depend only implicitly on velocity or reflection coefficient. For the sake of argument, however, let us assume that the LSJIMP operator, $\mathbf{L}$, is a non-linear function of these parameters, which the basic LSJIMP inversion makes no attempt to optimize. A multiple-free estimate of the primaries obviously enhances our ability to estimate imaging velocity, regardless of the method, and also permits us to model crosstalk noise from primaries that are below the onset of the seabed pure multiple. Thus the simplest nonlinear iteration of the LSJIMP method would proceed as follows, where the superscript k denotes that an operator or model vector is attached to the k^{th} nonlinear iteration:

iterate {

$\mathbf{L}^{[k]} \quad \Leftarrow \quad$ velocity, reflection coefficients, crosstalk model

$\mathbf{d} \quad = \quad \mathbf{L}^{[k]}\mathbf{m}^{[k]}$

$\mathbf{m}^{[k]} \quad \Rightarrow \quad$ updated velocity, crosstalk model

}

Nonlinear updating of the reflection coefficients of the multiple generators is in general a more difficult, and potentially more valuable, problem. If a multiple generator's pure multiple is obscured by other events, the reflection coefficient estimation scheme outlined in section 2.2.5 may produce inaccurate estimates, which the spatial regularization may not account for. For example, in the 2-D field data example shown in Chapter 3, the pure multiple for one multiple generator happens to be overlapped over almost the entire line by a prominent pegleg from another multiple generator.

I propose a nonlinear reflection coefficient updating scheme which obtains perturbations by fitting unmodeled events in the LSJIMP data residual, $\mathbf{r}_d$. If the initial reflection coefficient is perfect, then after convergence, $\mathbf{r}_d$ will contain only uncorrelated noise. If it is imperfect, then we also expect to see correlated events left over in the residual. Because LSJIMP separates each multiple mode indpendently in the model space ($\mathbf{m}_{i,k,m}$), we can simply apply the forward model for that mode ($\mathbf{L}_{i,k,m}$) to obtain an estimate of the particular multiple in data space, $\mathbf{d}_{i,k,m}$.

The main idea of my updating scheme is to compute a scalar update to the reflection coefficient of the m^{th} multiple generator, $\Delta\alpha_m$, such that

$$\|\mathbf{r}_d - \Delta\alpha_m\, \mathbf{d}_{i,k,m}\|^2 \tag{2.13}$$

is minimized. Since $\mathbf{r}_d$ may contain correlated events from primaries and other multiple modes, I suggest using $\mathbf{d}_{i,k,m}$ to compute a residual weight which is large where $\mathbf{d}_{i,k,m}$ is energetic, small where it is not. Using the absolute value of $\mathbf{d}_{i,k,m}$ is one possibility:

$$\left\| \left|\mathbf{d}_{i,k,m}\right| \left(\mathbf{r}_d - \Delta\alpha_m\, \mathbf{d}_{i,k,m}\right) \right\|^2. \tag{2.14}$$

In the implementation of minimization (2.14) used in this thesis, $\Delta\alpha_m$ is computed independently at each midpoint location, y. The updated reflection coefficient, $\alpha_m^{[k]}(y)$, is related simply to $\Delta\alpha_m$ and the previous reflection coefficient $\alpha_m^{[k-1]}(y)$:

$$\alpha_m^{[k]}(y) = \alpha_m^{[k-1]}(y)(1 + \Delta\alpha_m), \tag{2.15}$$

where the superscripts again represent nonlinear iteration index.

2.2 Particular Implementation of LSJIMP

In Section 2.1 I introduced the LSJIMP method in general. In the following section, I outline my particular implementation of the LSJIMP method. I start in Section 2.2.1 by extending the normal moveout (NMO) equation to image pegleg multiples in a prestack sense. In Sections 2.2.6-2.2.7 I introduce HEMNO (Heterogeneous Earth Multiple NMO Operator), a model-based multiple imaging operator which images peglegs in moderately heterogeneous geologic environments. In Sections 2.2.2-2.2.5 I present amplitude correction operators which model multiple events in the data from an image of the multiples. Finally, in Section 2.2.9, I outline how this particular imaging methodology for multiples fits into the LSJIMP methodology.

2.2.1 Kinematic imaging of pegleg multiples in a laterally-homogeneous earth

In a "1-D Earth" (horizontally-stratified, $v(z)$ medium), the normal-moveout (NMO) equation (Taner and Koehler, 1969) describes the prestack traveltime curve of a primary reflection at relatively short source-receiver offset:

$$t = \sqrt{\tau + \frac{x^2}{V_{\text{rms}}^2(\tau)}}. \tag{2.16}$$

Applied as an offset-dependent vertical time shift to a CMP gather, the NMO equation flattens an arbitrary primary to its zero-offset traveltime τ, where (half) offset is denoted x and the root-mean-square (RMS) velocity, $V_{\text{rms}}(\tau)$, is defined in a laterally-homogeneous earth as:

$$V_{\text{rms}}^2 = \frac{1}{\tau} \sum_{i=1}^{n_\tau} v_i^2 \Delta\tau \tag{2.17}$$

The earth is parameterized by n_τ layers of time thickness $\Delta\tau$, with constant interval velocity v_i in each layer.

Analogously, a modified NMO equation can image pegleg multiples in a 1-D Earth, as motivated graphically by Figure 2.3. From the figure, we see that kinematically, a first-order pegleg can be conceptualized as a "pseudo-primary" with the same offset, but with an additional two-way zero-offset traveltime to the multiple generator, τ^*. In equation form, let us extend this intuition to the general case of a j^{th}-order pegleg to write an NMO equation for peglegs:

$$t = \sqrt{(\tau + j\tau^*)^2 + \frac{x^2}{V_{\text{eff}}^2}}. \tag{2.18}$$

V_{eff} is the effective RMS velocity of the pseudo-primary shown in Figure 2.3. To derive an expression for V_{eff}, we modify the definition of RMS velocity, equation (2.17), to reflect a

j^{th}-order pegleg multiple's additional travel between the surface and multiple generator:

$$V_{\text{eff}}^2 = \frac{1}{\tau + j\tau^*}\left(j\sum_{i=1}^{n_{\tau^*}} v_i^2 \Delta\tau + \sum_{i=1}^{n_\tau} v_i^2 \Delta\tau\right). \tag{2.19}$$

Analogously, n_{τ^*} is the number of assumed layers between the earth's surface and the multiple generator. Notice that the two terms inside the parentheses of equation (2.19) are simply the definition of RMS velocity at τ^* and τ, respectively. We can substitute equation (2.19) accordingly to derive the final expression for $V_{eff}(\tau)$:

$$V_{\text{eff}}^2 = \frac{\left(j\tau^* V_{\text{rms}}^2(\tau^*) + \tau V_{\text{rms}}^2(\tau)\right)}{\tau + j\tau^*}. \tag{2.20}$$

Wang (2003) derives a similar series of expressions.

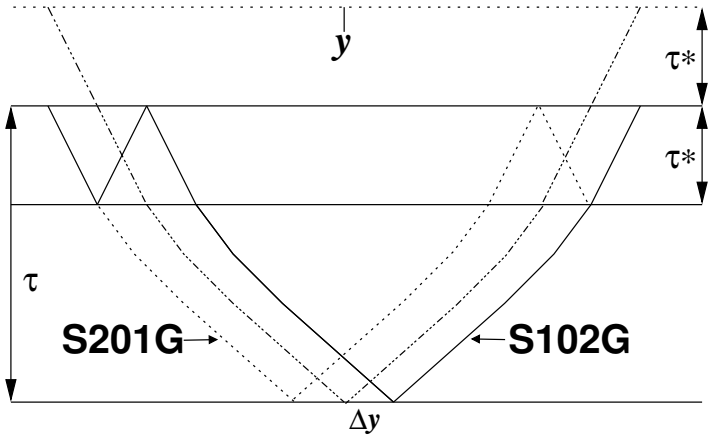

Figure 2.3: Pegleg multiples "S201G" and "S102G" have the same traveltimes as "pseudo-primary" with the same offset and an extra zero-offset traveltime τ^*. theory2d-schem [NR]

2.2.2 Amplitude corrections for pegleg multiples

It is tempting, but false, to believe that after scaling a pegleg by the reflection coefficient of the multiple generator, the event is directly comparable to a primary reflection. Primaries and their respective multiples traverse different raypaths between source and receiver, and thus exhibit different amplitude-versus-offset (AVO) behavior and suffer different anelastic attenuation and geometric spreading losses. In section 2.2.3 I derive the time- and offset-dependent

"Snell Resampling" operator to normalize peglegs to their primary with respect to AVO and attenuation. In section 2.2.4 I present a differential geometric spreading correction for peglegs, and finally, in section 2.2.5 I present an algorithm to estimate and apply the multiple generator's spatially-variant reflection coeffiecient.

2.2.3 Snell Resampling Normalizes AVO/Attenuation

Figure 2.4 illustrates the fact that in a $v(z)$ medium, there exists a single offset x_p such that a pegleg with offset x and primary with offset x_p are physically invariant with respect to AVO behavior and, assuming perfect elasticity in the top layer (often water), to anelastic attenuation. Since the pegleg multiple and primary in Figure 2.4 have the same emergence angle, θ, the time dip, or "stepout" of the two events is the same at x and x_p. In Appendix B, I derive the following expression for x_p, where V_{rms}, τ^*, and V_{eff} were defined in Section 2.2.1:

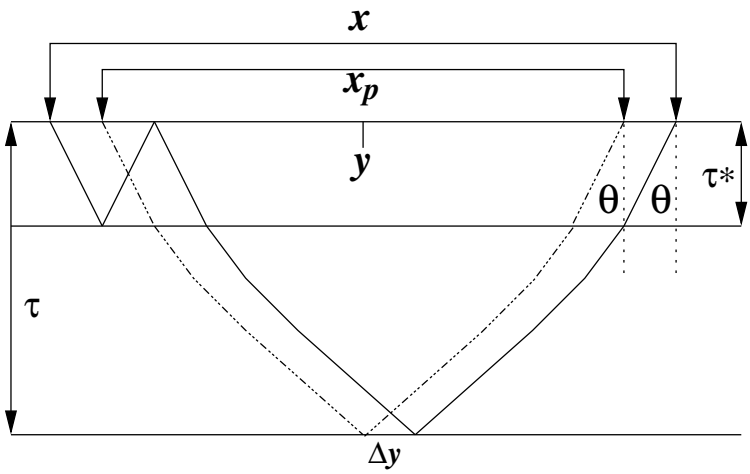

Figure 2.4: A primary and pegleg multiple with the same emergence angle (θ) and midpoint (y). Note different offsets (x and x_p) and a shift (Δy) in reflection point. theory2d-schem-snell [NR]

$$x_p = \frac{x\tau V_{\text{rms}}^2}{\sqrt{(\tau + j\tau^*)^2\ V_{\text{eff}}^4\ +\ x^2(V_{\text{eff}}^2 - V_{\text{rms}}^2)}}. \tag{2.21}$$

Equation (2.21) defines, for a j^{th}-order pegleg, a time-variable compression of the offset axis, which I denote "Snell Resampling". The name is derived from Ottolini's (1982) "Snell Traces" – a resampling of multi-offset reflection data along curves of constant stepout. Note that in

a constant velocity medium, $V_{\text{eff}} = V_{\text{rms}} = V$, and equation (2.21) reduces to the radial trace resampling used by Taner (1980) for the long-period deconvolution of peglegs.

Figure 2.5 illustrates application of Snell Resampling to a synthetic CMP gather. From the Figure, we see that Snell Resampling is an important vehicle for the exploitation of the additional information contained in the multiples. Notice how energy from the multiples is spread into the coverage gaps at near offsets and at 1.0 km offset. Snell Resampling moves energy from the multiples to the offset corresponding to its reflection angle at the target.

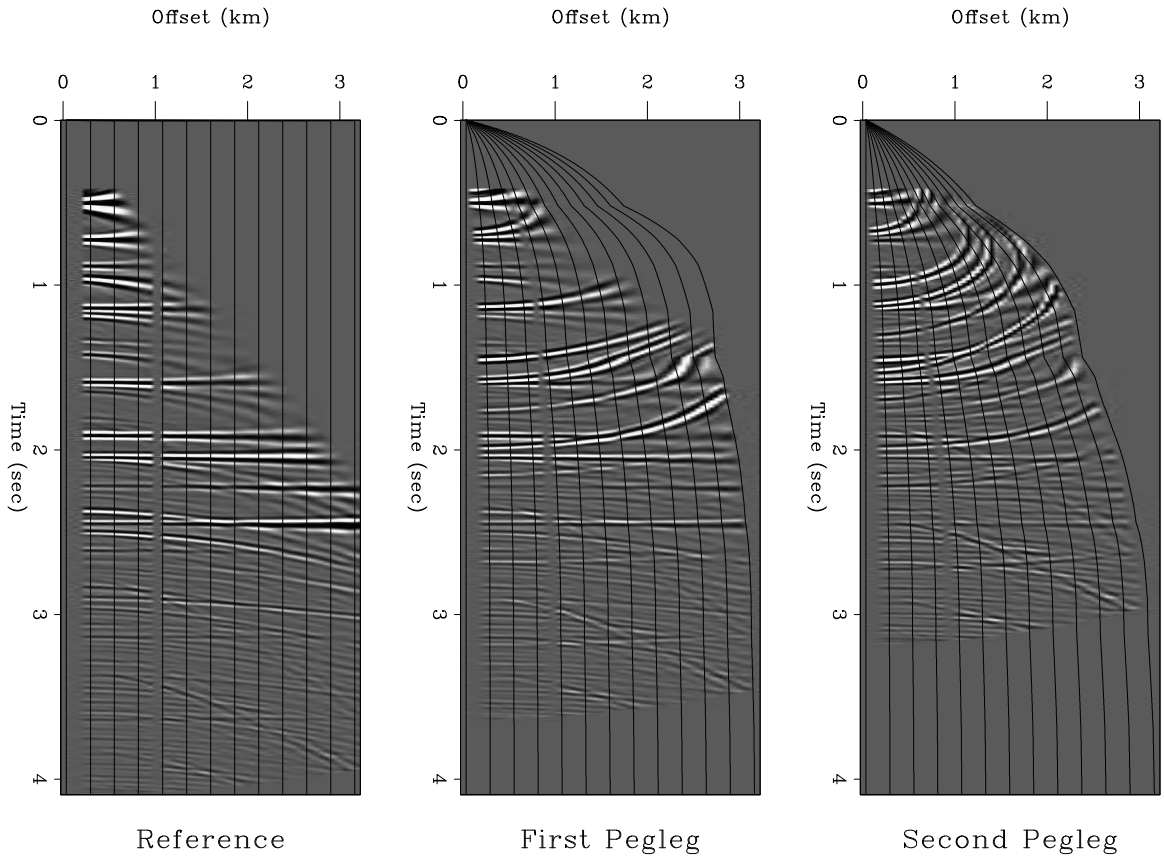

Figure 2.5: Snell Resampling demonstration. Left to right: a synthetic CMP gather after NMO for primaries and for first- and second-order peglegs, respectively. Snell Resampling (plus normalization to account for offset axis compression) was applied to the right two panels. The black lines illustrate the transformation's horizontal compression. The raw data has five unrecorded near offset traces and two dead traces at medium offsets. theory2d-snell.hask [CR,M]

Graphically (Figure 2.4), we may infer that the shift in midpoint, Δy, of the reflection points of the primary and first-order pegleg is:

$$\Delta y = \left(x - x_p\right)/2. \tag{2.22}$$

As a function of time, Δy decreases asymptotically to zero at infinite depth from a maximum of $x/4$ at the seabed. The deeper the reflector, the smaller Δy becomes. Similar expressions may be easily derived for multiples of other types and orders.

For peglegs arising from sub-seabed reflectors, the assumption of perfect elasticity for the multiple bounce breaks down. To some extent, however, the additional attenuation suffered by the multiple can, to first order, be treated as a decrease in reflection coefficient.

2.2.4 Differential Geometric Spreading

To correct peglegs for the effects of greater geometric spreading losses, I follow previous authors (Ursin, 1990; Lu et al., 1999) and write offset-dependent geometric spreading corrections for a primary (g_{prim}) and its pegleg multiples (g_{mult}) in the following notation:

$$g_{\text{prim}} = v^* t_{\text{prim}}(x) = \sqrt{(\tau v^*)^2 + \left(\frac{x v^*}{V}\right)^2} \tag{2.23}$$

$$g_{\text{mult}} = v^* t_{\text{mult}}(x) = \sqrt{[(\tau + j\tau^*)v^*]^2 + \left(\frac{x v^*}{V_{\text{eff}}}\right)^2}. \tag{2.24}$$

v^* is the velocity at the surface. After scaling by $g_{\text{mult}}/g_{\text{prim}}$ and Snell resampling, the amplitudes of an imaged pegleg multiple and its associated primary are consistent, to within a reflection coefficient.

2.2.5 Estimation/Application of Seabed Reflection Coefficient

After a pegleg multiple has been imaged, and undergone Snell Resampling and the differential geometric spreading correction, it is consistent with its primary to within the reflection coefficient of the multiple generator. In practice, the reflection coefficient always varies with space and reflection angle, though in many geologic environments these variations are both spatially smooth and small in magnitude.

In this thesis, I assume that the reflection coefficient varies in space, but does not vary with reflection angle. Assume that $\mathbf{p}(t,x,y)$ and $\mathbf{m}(t,x,y)$ are, respectively, small windows in time, offset, and midpoint of dimension $nt \times nx \times ny$, around a primary reflection and its first pure multiple after normalized Snell Resampling and differential geometric spreading correction. The reflection coefficients, $\mathbf{r}(y)$, are chosen to minimize the following quadratic functional:

$$\min_{\mathbf{r}(y)} \sum_{k=1}^{ny} \sum_{j=1}^{nx} \sum_{i=1}^{nt} \mathbf{w}(k)^2 \left[\mathbf{r}(k)\, \mathbf{p}(i,j,k) - \mathbf{m}(i,j,k)\right]^2 + \epsilon^2 \sum_{k=2}^{ny} [\mathbf{r}(k) - \mathbf{r}(k-1)]^2 . \quad (2.25)$$

The second term, a finite-difference first derivative applied to the unknown $\mathbf{r}(y)$, enforces a degree of smoothness across midpoint. The scalar term ϵ balances data fitting with model smoothness. The vector of residual weights, $\mathbf{w}(y)$, reflect the "quality" of the data at y.

Recall from Figure 2.4 that for a multiple and primary recorded at the same midpoint, there exists a shift in the target reflection point, Δy, described by equation (2.22) for a first-order pegleg. In my LSJIMP implementation, variations in reflection strength of the target reflector are ignored, but not those in the multiple generator. A first justification of this assumption is convenience: the strength of the target reflection is, after all, unknown. Secondly, since the target reflection points of all legs of a pegleg are symmetric about the midpoint, the average of the reflection stregths is the same as the primary's if the true reflection strength is locally linear with midpoint. Δy decreases with target depth, so for deep targets the local linearity assumption is likely to hold to first-order accuracy. Thirdly, ignoring target reflector variation implies that the model space of the LSJIMP inversion consists of one midpoint location only, which reduces memory usage and permits coarse-grained computer parallelization over midpoints. Therefore, when applying the reflection coefficient, we apply the coefficient at the assumed

reflection point for the particular multiple being imaged. Second order multiples would be scaled by reflection coefficients from two locations, and so on.

2.2.6 HEMNO: Imaging of pegleg multiples in a heterogeneous earth

In Sections 2.2.1-2.2.5 I developed a methodology, valid in a laterally-homogenous earth, to image pegleg multiples and make their amplitudes comparable to their primary. From Figure 2.3, recall that a first-order pegleg consists of two unique arrivals: the event with a multiple bounce over the source ("source-side" pegleg), and the event with a bounce over the receiver ("receiver-side" pegleg). When reflectors dip, the arrivals have different traveltimes on a CMP gather, and "split" into two separate events. Figure 2.6 illustrates the splitting phenomenon on the 2-D Gulf of Mexico dataset which will be used extensively in Chapter 3. The strong events in the "crosshairs" of the Figure are the first-order source-side and receiver-side seabed pegleg multiples from the top of salt reflection.

On CMP gathers, primary reflection hyperbolas generally have apexes at zero offset. Levin and Shah (1977) show that the apexes of split pegleg multiples shift away from zero offset, raising the apparent velocity of one leg (on one-sided marine data), which can hamper velocity analysis and Radon multiple suppression. Hargreaves et al. (2003) use an apex-shifted Radon transform for demultiple.

Even if reflectors dip only mildly, a prestack imaging method for peglegs must account for splitting. Mild variations in reflector depth over a cable length can introduce considerable destructive interference between the legs of a pegleg multiple at far offsets. This interference, is impossible to model with a 1-D theory, introduces false amplitude-versus-offset (AVO) behavior in the multiples, and certainly would hamper any attempts to use multiples as a constraint on the AVO signature of the primaries (Levin, 1996).

Levin and Shah (1977) deduced analytic kinematic moveout equations for split 2-D pegleg multiples, and Ross et al. (1999) extended the work to 3-D. Both approaches assume constant velocity and locally planar reflectors – depending on local geology, this may be unrealistic in practice. In this thesis, my particular implementation of LSJIMP relies on a simplified

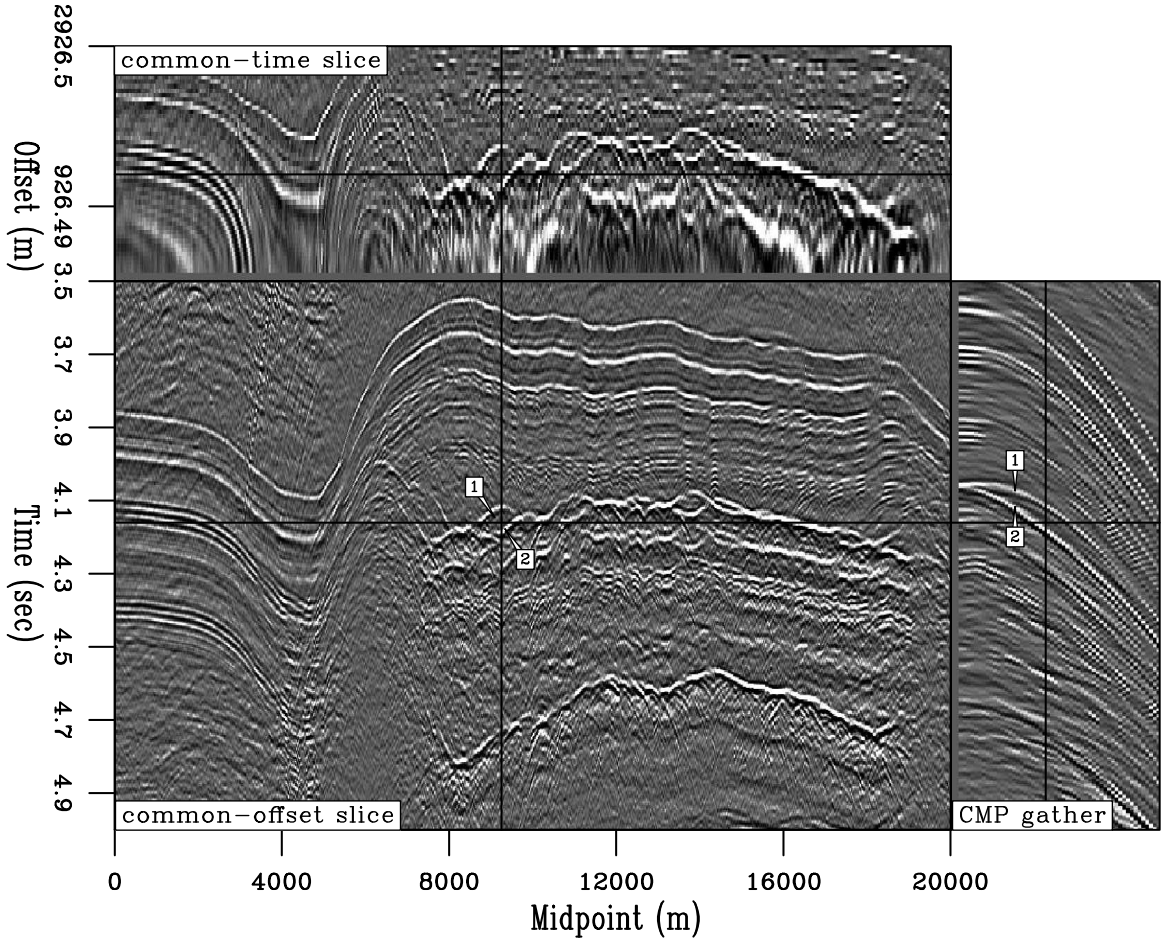

Figure 2.6: Splitting phenomenon observed on 2-D prestack field data from the Gulf of Mexico (used in Chapter 3). The seabed pegleg from the top of salt reflection splits noticeably into two distinct events (labels "1" and "2"). On the CMP gather the apexes of the two legs are shifted away from zero offset. theory2d-gulf.split [ER]

moveout equation based upon a more practically realizable conceptual model, which I call HEMNO (Heterogeneous Earth Multiple NMO Operator). In Appendix A I prove that for small reflector dips, the HEMNO traveltime equation reduces to Levin and Shah's moveout equations.

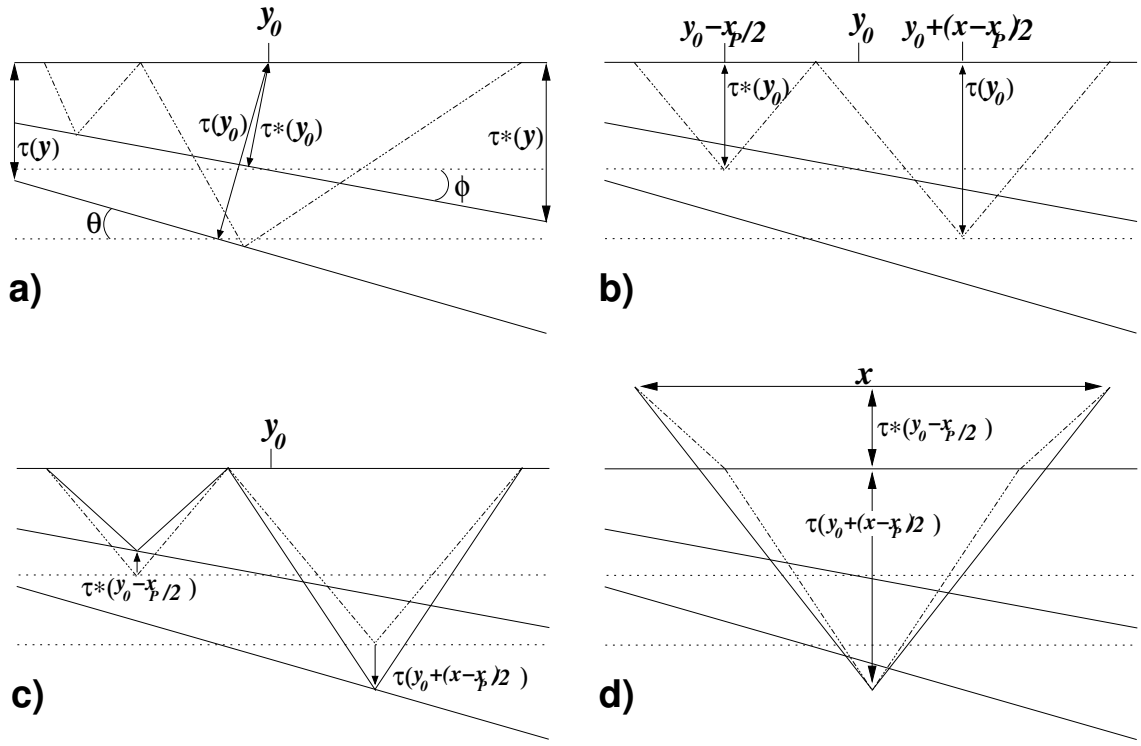

Figure 2.7: HEMNO operator schematic. (a) True raypath in constant-velocity earth. The zero-offset traveltimes to the seabed and subsea reflector are $\tau^*(y_0)$ and $\tau(y_0)$, respectively. (b) Assumed reflection points under flat-earth assumption. x_p is defined in equation (2.21). (c) Stretch legs of raypath vertically to match measured $\tau^*(y_0 - x_p/2)$ and $\tau(y_0 + (x - x_p)/2)$. Panel (d) Connect legs of raypath. The solid line that connects the reassembled raypath is the final result. theory2d-schem-pegleg-dip2 [NR]

Figure 2.7 graphically illustrates the HEMNO derivation in a constant-velocity earth. Panel a) illustrates the raypath of the "S102G" pegleg where the multiple generator and target reflector dip. Panel b) illustrates the raypath implied by the 1-D multiple imaging theory derived in Section 2.2.1: the primary leg of the multiple has offset x_p [equation (2.21)] and the zero-offset traveltime to both reflectors is spatially invariant. Panel c) illustrates the HEMNO strategy: we account for spatially-variant reflector geometry by vertically stretching the 1-D

raypath to match the zero-offset traveltime at the reflection points. However, the solid raypath in panel c) disobeys Snell's Law, so to obtain the final result in panel d), the tails of the legs of the ray are simply connected to produce a valid raypath, which has the equation of a hyperbola with offset x and zero-offset traveltime $\tau^*(y_0 - x_p/2) + \tau(y_0 + (x - x_p)/2)$. We first define for simplicity

$$\tau_m = \tau^*(y_0 - x_p/2) \quad \text{and} \quad \tau_p = \tau(y_0 + (x - x_p)/2), \tag{2.26}$$

and then write the HEMNO equation:

$$t^2 = \left(\tau_m + \tau_p\right)^2 + \frac{x^2}{V_{\text{eff}}^2}. \tag{2.27}$$

Equation (2.27) flattens one leg of a first-order pegleg in offset and shifts the event to the zero-offset traveltime of the primary. By using V_{eff}, we ignore lateral velocity variations, which is consistent with the assumption of small dips. Similar expressions may be derived for other multiple events, but I omit the derivations for brevity. Figure 2.8 illustrates application of the HEMNO equation to the split top of salt pegleg shown in Figure 2.6.

2.2.7 HEMNO Implementation Issues

To implement equation (2.27) on a computer, we must obtain two quantities. The first, the zero-offset traveltime of the multiple generator, τ_m, may be obtained by hand- or auto-picking, and optionally refined by cross-correlation. However, the second quantity, the zero-offset traveltime to an arbitrary target reflector, τ_p , cannot realistically be picked. I obtain τ_p automatically by event tracking, using a smooth estimate of reflector dip obtained from a zero-offset section, in a fashion similar to Lomask's (2003) data flattening method.

How to best obtain this dip estimate is a question still open to debate. Automatic dip estimation techniques like Fomel's (2002) yield good results in regions where reflectors are densely packed, coherent, and do not cross. Unfortunately, below the onset of the first seabed multiple, a zero-offset section will contain crossing events. While previous authors have developed methods to simultaneously estimate two crossing dips (Fomel, 2001; Brown, 2002),

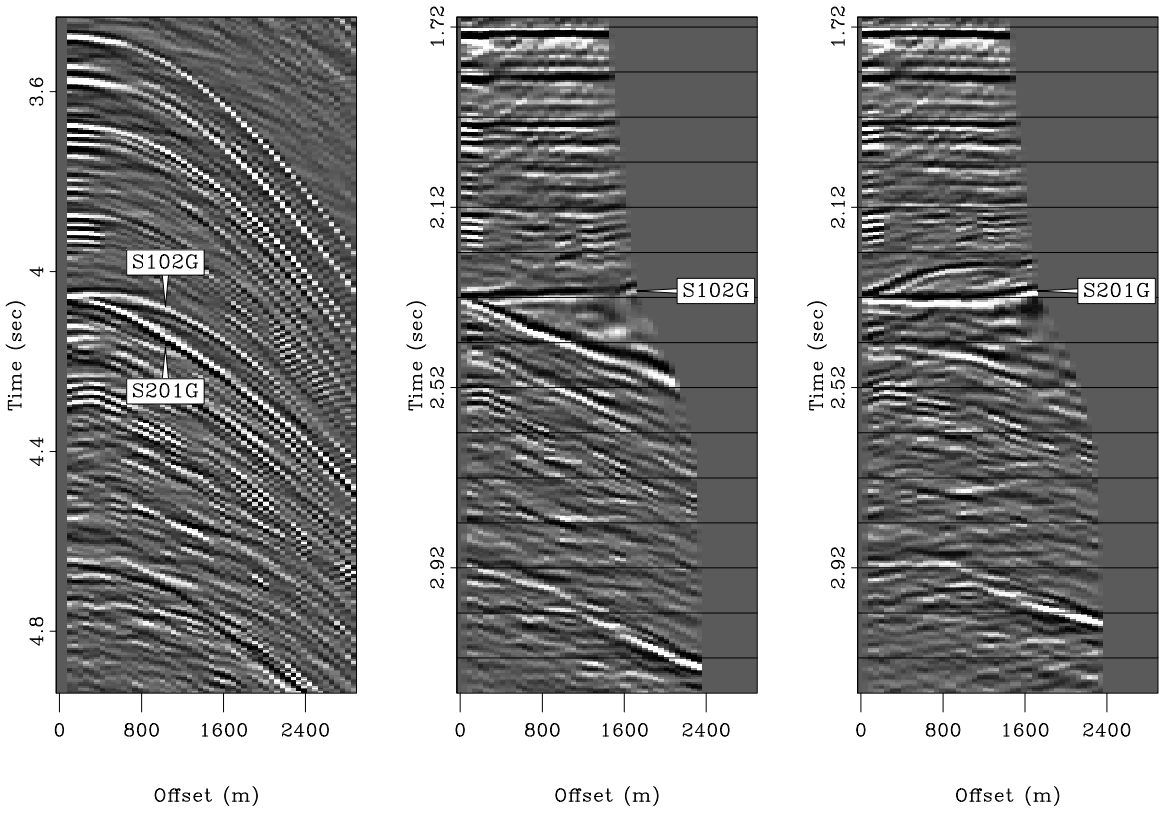

Figure 2.8: Left: CMP gather extracted from midpoint 9200 m of the Mississippi Canyon data cube shown in Figure 2.6. Notice the split top of salt pegleg at $\tau = 4.05s$. Center and Right: HEMNO equation applied to two splits. Notice how the events are independently focused in time and offset. The images panels have also undergone normalized Snell Resampling, differential geometric spreading correction, and application of the seabed reflection coefficient. theory2d-gulf.hemno.split [CR]

the problem is highly nonlinear, and it is difficult to unambiguously associate one dip with the primaries, and the other with multiples.

I have had greater success with a different technique which exploits cubic smoothing splines (Hutchinson and De Hoog, 1985). On 2-D data, it is easy to pick important reflectors on a zero-offset section, even weak events buried under the multiples. The reflectors are first fit with a cubic smoothing spline, from which the dip, simply the first derivative, can be computed analytically. These computed dips are finally interpolated in time, again using a cubic smoothing spline. This method is somewhat manually intensive, but gives reliable results. In 3-D, the spline technique may have value when crossline aliasing renders automatic dip estimation schemes ineffective. If the data contain many important reflectors, though, the picking may entail considerable manual labor.

2.2.8 Velocity-Depth Ambiguity in the Imaging of Multiples

As shown in Figure 2.7, the HEMNO approach for imaging pegleg multiples that I introduced in section 2.2.6 assumes that the reflection points of multiples do not move in midpoint from their "1-D Earth" position. This assumption is violated in the presence of nonzero reflector dip or lateral velocity variation. Reflector dip affects the kinematic properties of multiples in two ways, which were quantified by Levin (1971) in a seminal paper. First, dip always leads to a negative shift in the zero-offset traveltime of multiples relative to the 1-D case. Second, multiples from dipping reflectors always have a higher apparent velocity than those from flat reflectors.

Prestack migration methods naturally and automatically unravel the mystery of dip to correct seismic data for the effects of nonzero offset. However, HEMNO is a more mechanical operation. To image a multiple, it requires an estimate of zero-offset traveltime and the multiple's stacking velocity. Unfortunately, these quantities are inherently coupled. The goal of HEMNO is to "best" align a multiple and its primary as a function of offset. A small perturbation in τ^* may better align the multiple and primary at zero offset, but will change the multiple's apparent velocity and possibly worsen alignment at far offsets. Conversely, if a multiple is nonflat after imaging, a small velocity perturbation may improve far-offset alignment

but will not change near-offset alignment.

In this thesis I take a pragmatic view of the velocity-depth ambiguity problem. Pure multiples do not split. If a primary is flat after imaging, but its pure multiple is not, then any residual moveout in the multiple is due to dip and/or lateral velocity variation. I use a two-step process to handle the nonlinear coupling of velocity and reflector position:

1. Compute perturbation in τ^* by aligning near-offset stacks of primary and its pure multiple with a cross-correlation approach (Rickett and Lumley, 2001).

2. Compute perturbation in multiple velocity by performing residual stacking velocity analysis for the (pure) multiple event of interest. The velocity perturbation is applied for all τ in V_{eff} [equation (2.20)].

2.2.9 Solving the particular LSJIMP problem

Now that we have derived appropriate imaging and amplitude correction operators, we are ready to translate the general LSJIMP modeling equation (2.2) to my particular implementation. The primary image, $\mathbf{m}_0$, is mapped into data space primary events by NMO, $\mathbf{N}_0$. Similarly, a given pegleg image, $\mathbf{m}_{i,k,m}$, is mapped into data space by sequentially applying the differential geometric spreading correction ($\mathbf{G}_{i,m}$), Snell resampling ($\mathbf{S}_{i,m}$), HEMNO ($\mathbf{N}_{i,k,m}$), and finally, a reflection coefficient ($\mathbf{R}_{i,k,m}$). Let us rewrite equation (2.2) accordingly:

$$\mathbf{d}_{\text{mod}} = \mathbf{N}_0\mathbf{m}_0 + \sum_{i=1}^{p}\sum_{k=0}^{i}\sum_{m=1}^{n_{\text{surf}}} \mathbf{R}_{i,k,m}\mathbf{N}_{i,k,m}\mathbf{S}_{i,m}\mathbf{G}_{i,m}\mathbf{m}_{i,k,m}\,. \tag{2.28}$$

We see that in equation (2.28), the analog to $\mathbf{L}_{i,k,m}$ in equation (2.2) is $\mathbf{R}_{i,k,m}\mathbf{N}_{i,k,m}\mathbf{S}_{i,m}\mathbf{G}_{i,m}$.

The data residual weight in equation (2.5), $\mathbf{W_d}$, can often strongly influence the success of the inversion. Technically, $\mathbf{W_d}$ carries a heavy burden: it must decorrelate and balance the residual. However, I have found that a simpler form for $\mathbf{W_d}$ nontheless pays dividends. I set $\mathbf{W_d}$, which has the same dimension as a CMP gather, to zero where the data, $\mathbf{d}$, has an empty trace, and also above the onset of the seabed reflection.

Chapter 3

2-D Field Data Results

In 1997, WesternGeco distributed a 2-D dataset, acquired in the Mississippi Canyon region of the Gulf of Mexico, for the testing of multiple suppression algorithms. As illustrated on the CMP-stacked section, Figure 3.1, the data contain a variety of strong surface-related multiples which hamper primary imaging, and enough geologic complexity to render one-dimensional multiple suppression methods ineffectual.

In this chapter, I show the results of testing my particular implementation of the LSJIMP technique on 750 CMP locations of the Mississippi Canyon dataset, modeling four multiple generators–the seabed, two strong shallow reflectors, and the top of salt–as labeled by the picks on Figure 3.1. Only first order multiples are included in the inversion. Thus in equation (2.28), $n_{\text{surf}} = 4$ and $p = 1$.

Estimation of a multiple generator's reflection coefficient is a crucially important step in my implementation of LSJIMP. Figures 3.2-3.5 illustrate the result of applying the reflection coefficient methodology outlined in Section 2.2.5 to each of the four multiple generators shown in Figure 3.1. Each Figure shows a stack of the local windows around the primary reflection and first pure multiple after alignment with cross-correlation, weighted by a user-defined residual weight which is set to zero where the data appear incoherent, and to one elsewhere. The seabed and R1 reflections (Figures 3.2 and 3.3) have the greatest coherency, with fairly consistent estimated reflection coefficients across all midpoints, although the R1

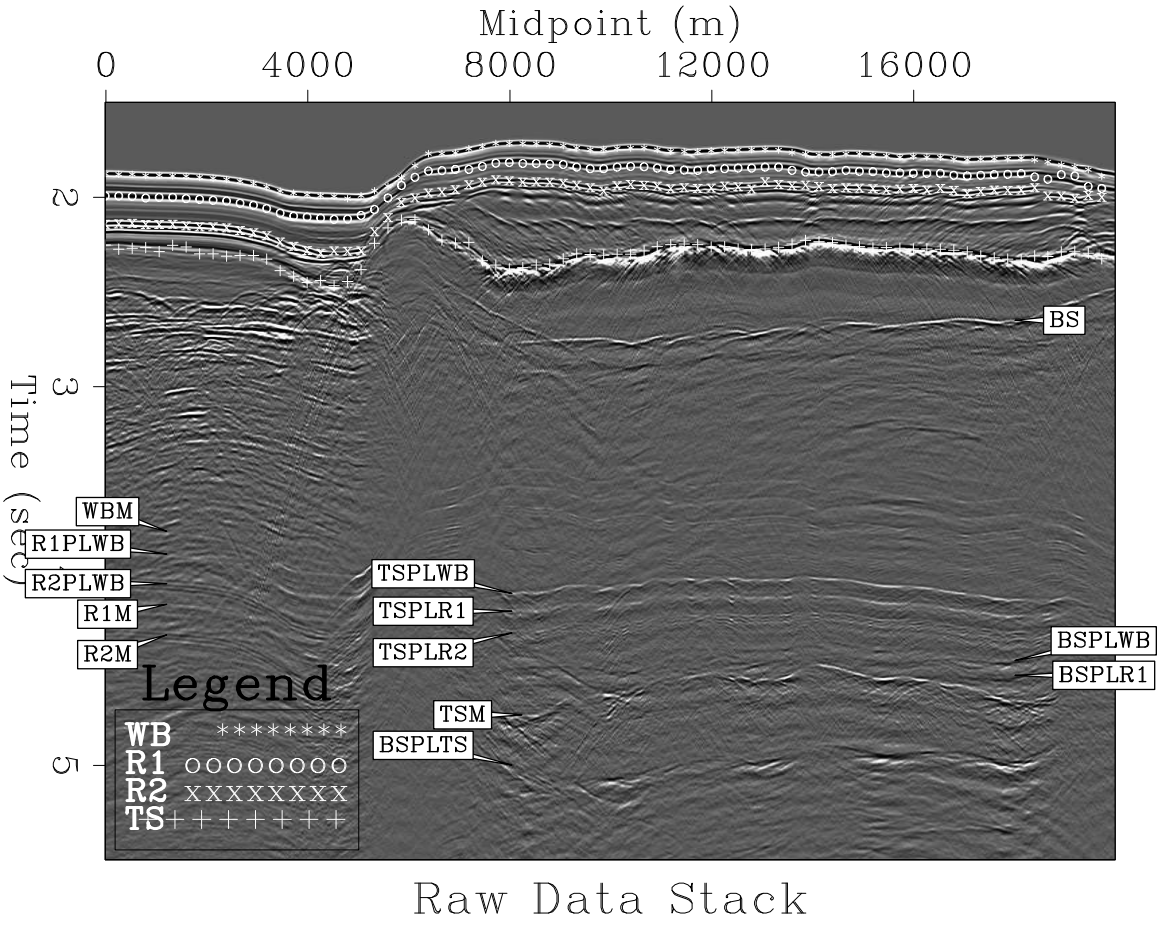

Figure 3.1: Stacked Mississippi Canyon 2-D dataset (750 midpoints), annotated with important multiple-generating horizons and multiples, after application of t^2 gain. Four multiple generators were modeled in the LSJIMP inversion: WB - seabed; R1,R2 - strong shallow reflections; TS - top of salt. Bottom of salt – BS, is also shown. Naming convention for pure first-order multiples: (*reflector*)M, e.g., R1M. Naming convention for first-order pegleg multiples: (*target*)PL(*multiple generator*), e.g., BSPLWB. results2d-gulf.stackraw [CR]

pure multiple partially overlaps the strong R2 seabed pegleg and tends to bias the estimated R1 reflection coefficient upward. The short wavelength of the multi-peaked R2 reflection (Figure 3.4) cause offset-dependent tuning effects that somewhat degrades our ability to reliably estimate a reflection coefficient. Lastly, strong head waves and a rugose salt top degrade the coherency of the top-of-salt reflection and its multiple (Figure 3.5), although we can get a fairly reliable estimate between midpoints of about 12000 and 18000 meters.

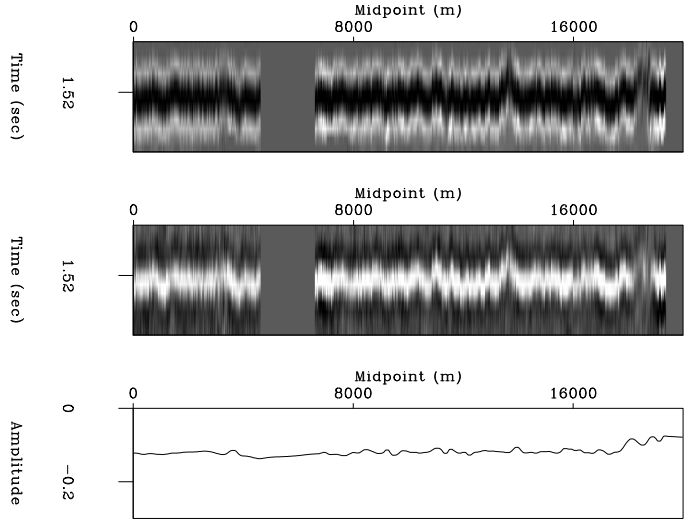

Figure 3.2: Top: Stack of window around seabed reflection (WB). Center: Stack of window around seabed pure multiple (WBM). Bottom: estimated WB reflection coefficient. results2d-rc.1.gulf [CR]

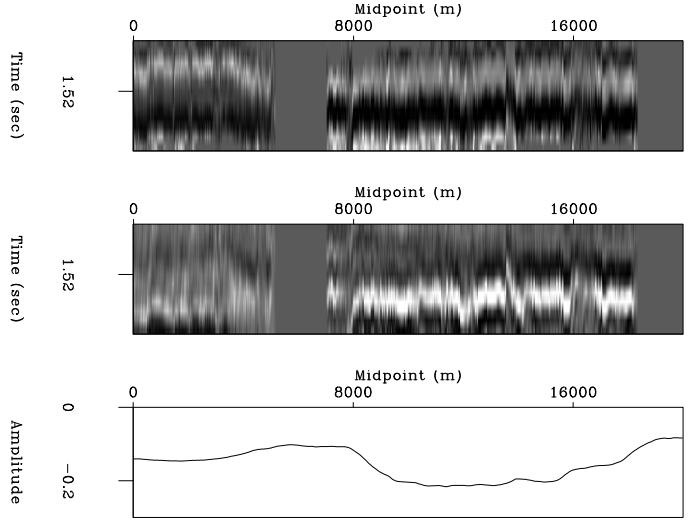

Figure 3.3: Top: Stack of window around R1 reflection. Center: Stack of window around R1 pure multiple (R1M). Bottom: estimated R1 reflection coefficient. results2d-rc.2.gulf [CR]

WesternGeco supplied a depth interval velocity model, so computation of stacking velocities was trivial. I ran LSJIMP with 20 conjugate gradient iterations on 28 CPUs (1.3 Ghz

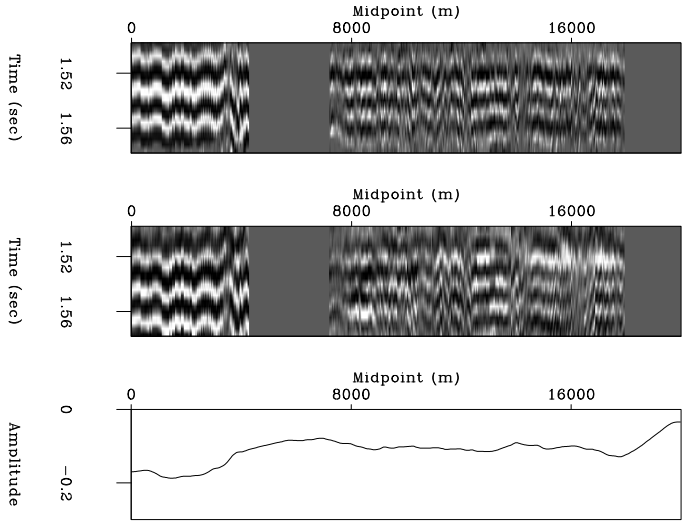

Figure 3.4: Top: Stack of window around R2 reflection. Center: Stack of window around R2 pure multiple (R2M). Bottom: estimated R2 reflection coefficient. results2d-rc.3.gulf [CR]

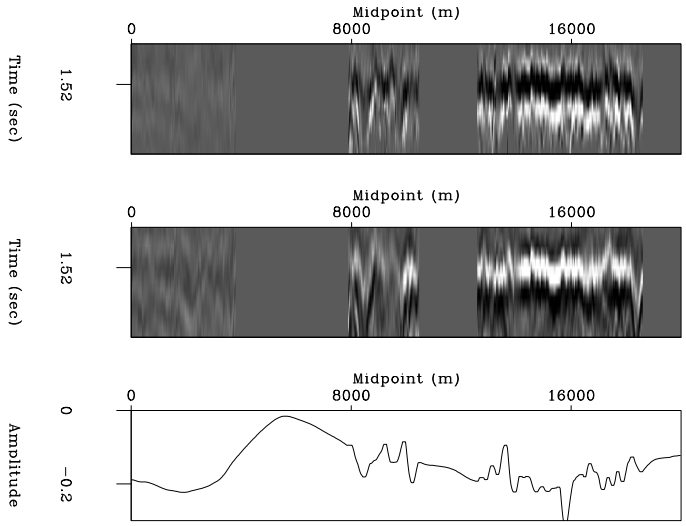

Figure 3.5: Top: Stack of window around top-of-salt reflection (TS). Center: Stack of window around top-of-salt pure multiple (TSM). Bottom: estimated TS reflection coefficient. results2d-rc.4.gulf [CR]

Pentium 3) of a Linux cluster, for a total run time of around 3 hours, including all I/O. Coincidentally, the run time is very similar to the prestack wave-equation depth migration run to generate the results in section 3.0.1.

Figure 3.6 illustrates the stack of the LSJIMP primary image, $\mathbf{m}_0$, which should contain only primaries. From the difference panel (c), note that important above-salt peglegs are almost entirely removed. Primaries are not visibly damaged. Salt rugosity contributes negatively to the separation, by forming diffractions that are not modeled by HEMNO, and by violating HEMNO's small reflector dip assumption. Still, LSJIMP does a fairly good job of removing the specular components of strong salt-related multiples. Some deep multiple energy remains. While unmodeled multiple events, such as internal salt multiples, may explain the residual, another likely contributor is the complex subsalt wave propagation. Time imaging operators like HEMNO generally perform more poorly than depth migration below large velocity contrasts.

Figures 3.7 and 3.8 make the same comparison as Figure 3.6, but in small windows to emphasize local features. The geological context of Figure 3.7 is a generally well-behaved sedimentary basin, with shallow dips and low velocity contrast. Notice that a variety of strong peglegs are largely removed without badly damaging the many updipping primary events in the section. Figure 3.8 is taken from over the tabular salt body. The multiples visible in this window are effectively separated from the data, even those from the top and bottom of the salt. Weak subsalt primaries, like the anticlinal structure which peaks around CMP 16000 m are not visibly harmed by the separation.

Figures 3.9-3.11 show the LSJIMP results at three midpoint locations. In each Figure, panels (c), (d), (g), and (h) illustrate the estimated total first order multiple from each of the four multiple generators. For instance, to generate the estimated seabed pegleg panel (c), we construct a model vector,

$$\mathbf{m}_{\text{wb}} = \begin{bmatrix} \mathbf{0} & \mathbf{m}_{1,0,1} & \mathbf{m}_{1,1,1} & \mathbf{0} & \mathbf{0} & \mathbf{0} & \mathbf{0} & \mathbf{0} & \mathbf{0} \end{bmatrix}^T, \tag{3.1}$$

where vector $\mathbf{0}$ has the same dimension as a CMP gather and vectors $\mathbf{m}_{1,0,1}$ and $\mathbf{m}_{1,1,1}$ are the images of the source and receiver peglegs from the seabed. To compute the estimated total

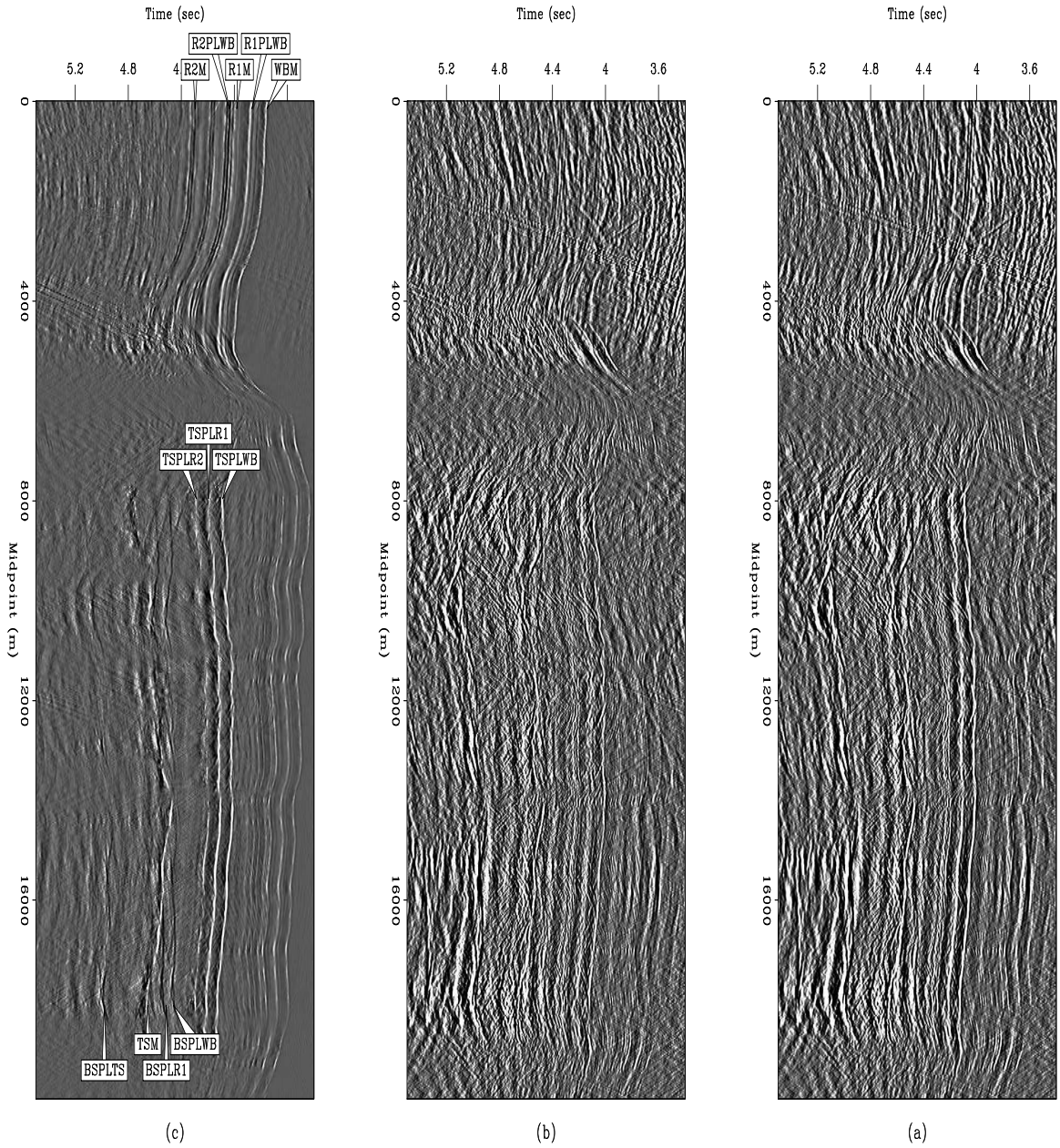

Figure 3.6: Mississippi Canyon stacked section before and after LSJIMP. All panels windowed in time from 3.5 to 5.5 seconds and gained with t^2. (a) Raw data stack. (b) Stack of estimated primary image, $\mathbf{m}_0$. (c) Stack of the subtracted multiples. Prominent multiples labeled as in Figure 3.1. results2d-stackcomp.gulf [CR,M]

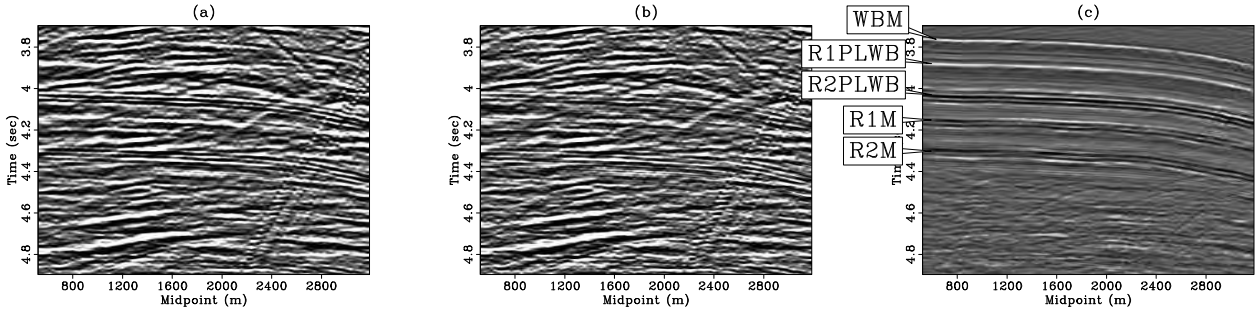

Figure 3.7: Zoom of Mississippi Canyon stacked section before and after LSJIMP. All panels windowed in time from 3.7 to 4.9 seconds and in midpoint from 500 to 3200 meters and gained with t^2. (a) Raw data; (b) Estimated primaries ($\mathbf{m}_0$); (c) Stack of the subtracted multiples. Multiples labeled as in Figure 3.1. results2d-stackcomp.zoom.1.gulf [CR,M]

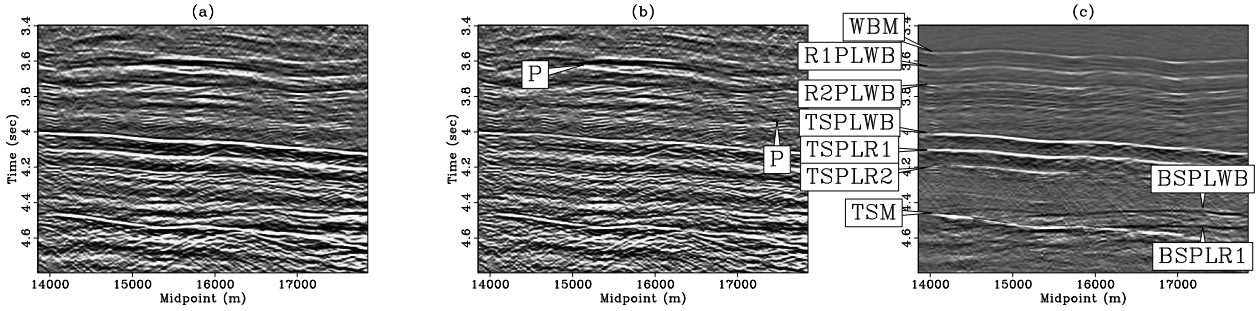

Figure 3.8: Zoom of Mississippi Canyon stacked section before and after LSJIMP. All panels windowed in time from 3.4 to 4.8 seconds and in midpoint from 13850 to 17850 meters and gained with t^2. (a) Raw data; (b) Estimated primaries ($\mathbf{m}_0$); (c) Stack of the subtracted multiples. Multiples labeled as in Figure 3.1. Subsalt primary events labeled "P". results2d-stackcomp.zoom.3.gulf [CR,M]

first-order seabed pegleg, we simply apply the LSJIMP forward model:

$$\mathbf{d}_{\text{wb}} = \mathbf{L}\mathbf{m}_{\text{wb}}. \tag{3.2}$$

An analogous process can be repeated for the first-order peglegs from the other three multiple generators modeled here. The modeled data (panel (e)) is simply the sum of the estimated primaries (panel (b)) and the first-order peglegs from the four modeled multiple generators. The residual error (panel (f)) is the difference between the input data and modeled data, with the residual weight applied to account for missing traces in the input.

Figure 3.9 comes from the sedimentary basin portion of the data. The multiples on this gather have fairly simple moveout behavior. From the relatively small amount of correlated energy on the residual error panel (f), we see that most multiples present in the data are modeled well by LSJIMP. However, notice the introduction of a "new" event to the modeled data around $\tau = 4.15s$. The R1M event overlaps with R2PLWB, which leads to crosstalk leakage and a poor estimate of R1's reflection coefficient. As we will see later, in section 3.3, the nonlinear updating scheme of section 2.1.8 helps solve this problem.

Figure 3.10 is drawn from the left-hand side of the salt body. The separation results are quite good, both for the relatively simple shallow multiples and for the complex salt-related multiples, which visibly split. A flat event around 4.5 seconds, which appears to be a primary, is actually most likely a pegleg multiple from the base of salt, flattened because the stacking velocity decreases below the salt.

Figure 3.11 is drawn from the right-hand side of the salt body. As with Figure 3.10, some of the complex splitting behavior in the salt-related peglegs is effectively modeled by HEMNO. In this case, the reflector dips are such that the events split at medium offsets, but happen to coincide at far offsets. Signal events are quite difficult to spot under the multiples, but some shallow events are uncovered.

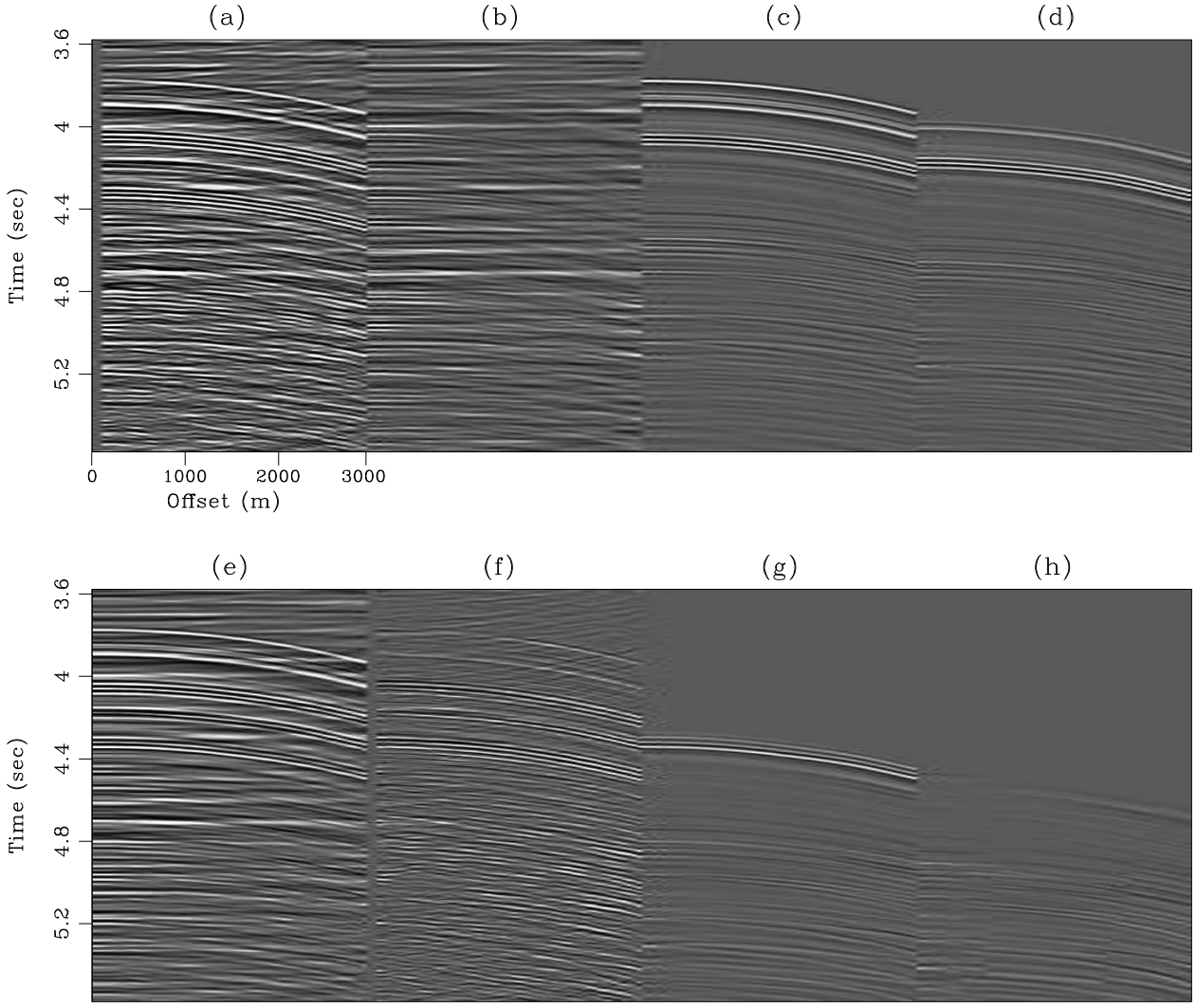

Figure 3.9: Mississippi Canyon CMP 55 (1440 m). Events labeled as in Figure 3.1. All panels NMO'ed with stacking velocity and windowed in time from 3.5 to 5.5 seconds and gained with t^2. (a) Raw data; (b) Estimated primaries ($\mathbf{m}_0$); (c) Estimated WB peglegs; (d) Estimated R1 peglegs; (e) Estimated data (sum of (b), (c), (d), (g), and (h)); (f) Data residual (difference of (a) and (e)); (g) Estimated R2 peglegs; (h) Estimated TS peglegs. results2d-comp1.4.lsrow.gulf.55 [CR]

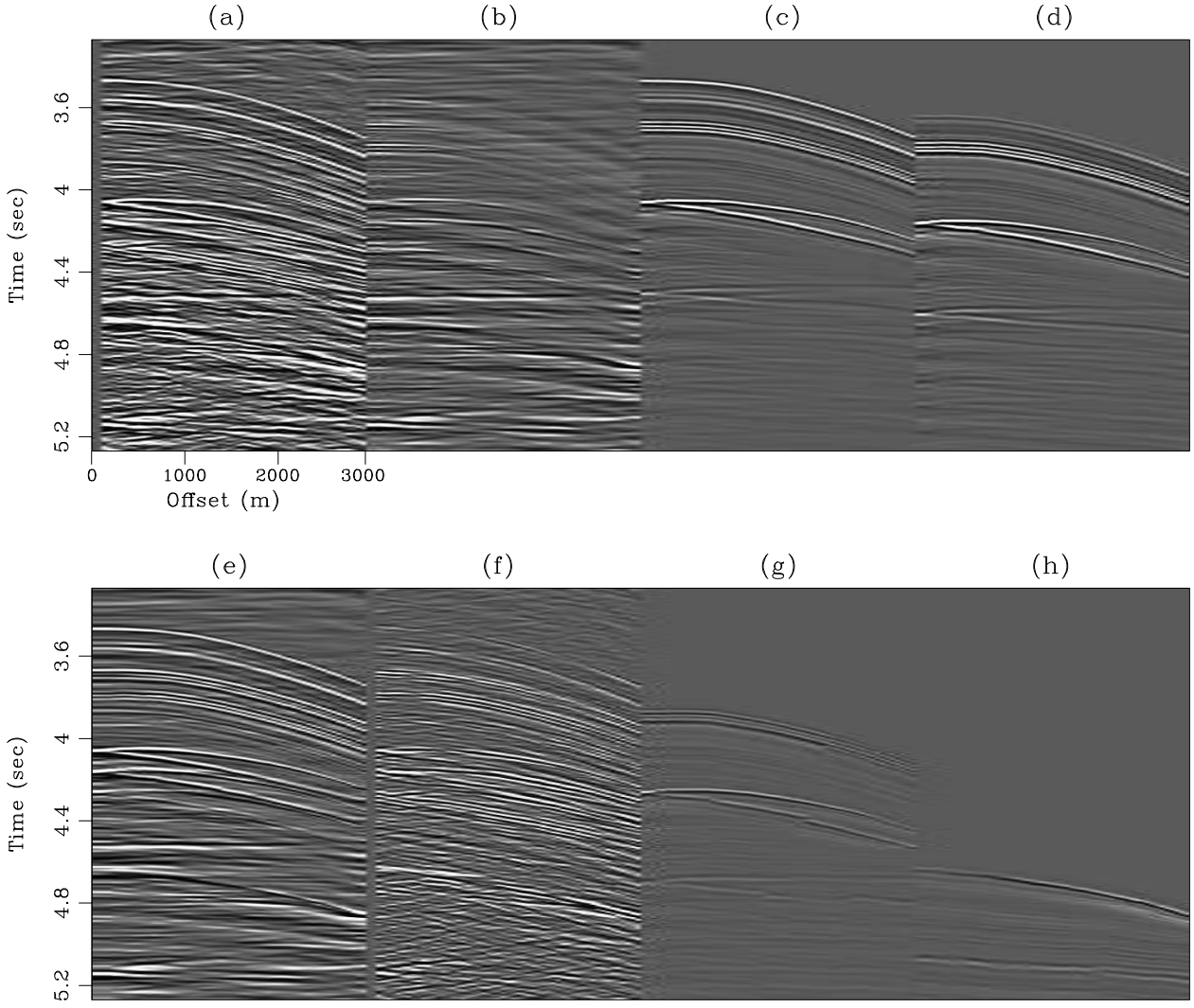

Figure 3.10: Mississippi Canyon CMP 344 (9150 m). Events labeled as in Figure 3.1. All panels NMO'ed with stacking velocity and windowed in time from 3.5 to 5.5 seconds and gained with t^2. (a) Raw data; (b) Estimated primaries ($\mathbf{m}_0$); (c) Estimated WB peglegs; (d) Estimated R1 peglegs; (e) Estimated data (sum of (b), (c), (d), (g), and (h)); (f) Data residual (difference of (a) and (e)); (g) Estimated R2 peglegs; (h) Estimated TS peglegs. results2d-comp1.4.lsrow.gulf.344 [CR]

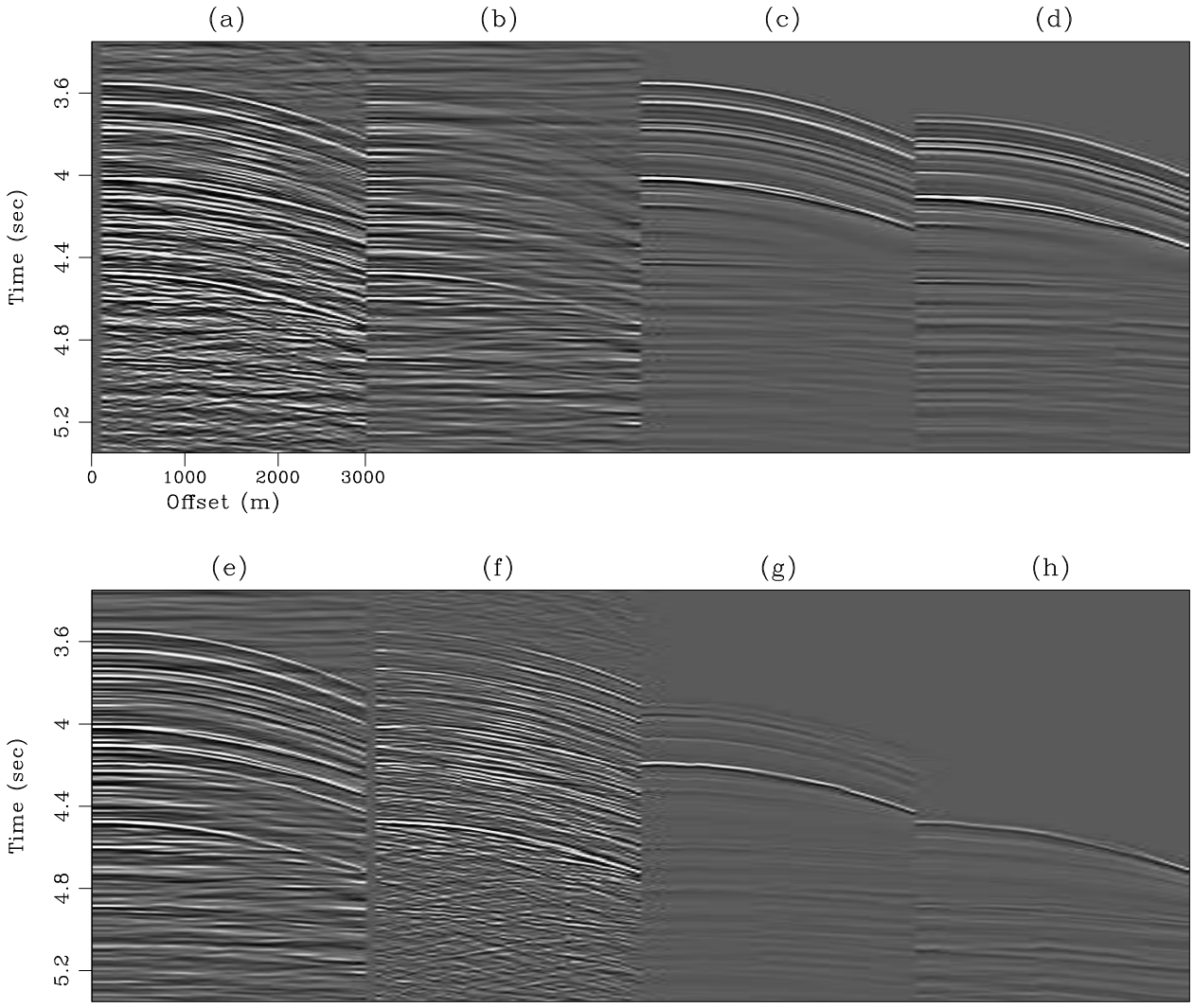

Figure 3.11: Mississippi Canyon CMP 540 (14400.0 m). Events labeled as in Figure 3.1. All panels NMO'ed with stacking velocity and windowed in time from 3.5 to 5.5 seconds and gained with t^2. (a) Raw data; (b) Estimated primaries ($\mathbf{m}_0$); (c) Estimated WB peglegs; (d) Estimated R1 peglegs; (e) Estimated data (sum of (b), (c), (d), (g), and (h)); (f) Data residual (difference of (a) and (e)); (g) Estimated R2 peglegs; (h) Estimated TS peglegs. results2d-comp1.4.lsrow.gulf.540 [CR]

3.0.1 Depth Migration Before and After LSJIMP

My particular LSJIMP implementation would likely come early in a modern seismic processing flow; after stacking velocity analysis, but before depth migration and interval velocity model building. Therefore a scenario of considerable practical interest is to view LSJIMP as a multiple suppression algorithm, and to treat the estimated LSJIMP primaries (after inverse NMO) as demultipled data, which would then be depth migrated.

WesternGeco supplied a depth interval velocity model with the data. I migrated the raw data and the LSJIMP primary data using a 2-D Extended Split-Step prestack depth migration algorithm (Stoffa et al., 1990) with three so-called "reference velocities" to handle lateral velocity variation. Image sampling in depth is 6.67 meters. The migration algorithm outputs gathers as a function of depth, midpoint, and subsurface offset. Using the method of Sava and Fomel (2000), the offset gathers are converted to Angle-domain Common-image gathers (ADCIGs) as a function of opening angle at the reflector.

Figure 3.12 shows angle stacks, after a $z^{1.5}$ gain, of the Mississippi Canyon raw data, the data after LSJIMP, and the difference of the two. The Figure is similar in style to Figure 3.6. The removed multiples are simplest to view on the left-hand side of the section, where the geology is less complicated than under the salt body. In the sedimentary region, we notice, as before, that LSJIMP can cleanly separate primaries from many different multiple reflections. In the salt region, the results are somewhat muddied, since migration strongly defocuses multiples. We see that much multiple energy has been removed, though much remains. Subsalt primaries, already difficult to spot without any multiple energy, are uncovered better, especially around 3500 meters depth. The dominant dip is negative (toward the surface with increasing midpoint).

For reasons explained in more detail in section 3.0.2, some primary energy is seen on the difference panel, where we hope to see only multiple energy. The loss of primary energy, while well below the clip value anywhere, is strongest for the top of salt reflection. Much of the lost energy has a high spatial wavenumber, and likely arises from diffractions which my implementation of LSJIMP cannot model. Also, the large velocity contrast at the top of salt gives rise to strong head waves, which have a high apparent velocity. These events, which are

not flat after NMO for primaries, are filtered out as noise by the LSJIMP regularization which differences across offset.

Figures 3.13 and 3.14 illustrate, after $z^{1.5}$ gain, ADCIGs at midpoints 55 and 344 (of 750), respectively. Compare these Figures to Figures 3.9 and 3.10. Figure 3.13 is extracted from the sedimentary region of the data. Notice that LSJIMP has quite cleanly separated multiples from the primaries, and certainly improved our ability to interpret the angle gather for amplitude-versus-angle phenomena.

Figure 3.14, on the other hand, is extracted from the salt-bearing region of the data. Visually, it is far more difficult on the angle gather to distinguish primaries from multiples, although peglegs from shallow reflectors, between 3500 and 4300 meters depth, are recognizable and cleanly removed from the data, uncovering some hidden primaries. Notice that some downcurving reflections within the salt (1900 to 2800 meters depth), which may be internal multiples, are attenuated by LSJIMP, since they are not flat like true signal events. Furthermore, the events with negative dip below 4000 meters, which may be out-of-plane reflections or diffractions, are also attenuated somewhat.

3.0.2 A closer look at the residuals

The theoretical development of the LSJIMP algorithm given in Chapter 2 defines the data and model residuals in mathematical and algorithmic terms, but in this section, I more practically illustrate the structure of and relationship between the residual vectors with a real data example. Figures 3.15-3.20 were computed at CMP 55 or 750 of the Mississippi Canyon 2-D dataset, in the sedimentary region of the data. Figures which display seismic data are divided in half along the time axis and clipped independently for viewing purposes.

Figure 3.15 illustrates, as a function of conjugate gradient iteration, the norm of the data and model residuals from the LSJIMP inversion at CMP 55. Although the norm of the combined model and data residual [equation (2.12)] is guaranteed to decrease with iteration, we see that the individual residuals may decrease at different rates, or even increase with iteration. Of particular interest in the Figure is the model residual corresponding to differentiation across

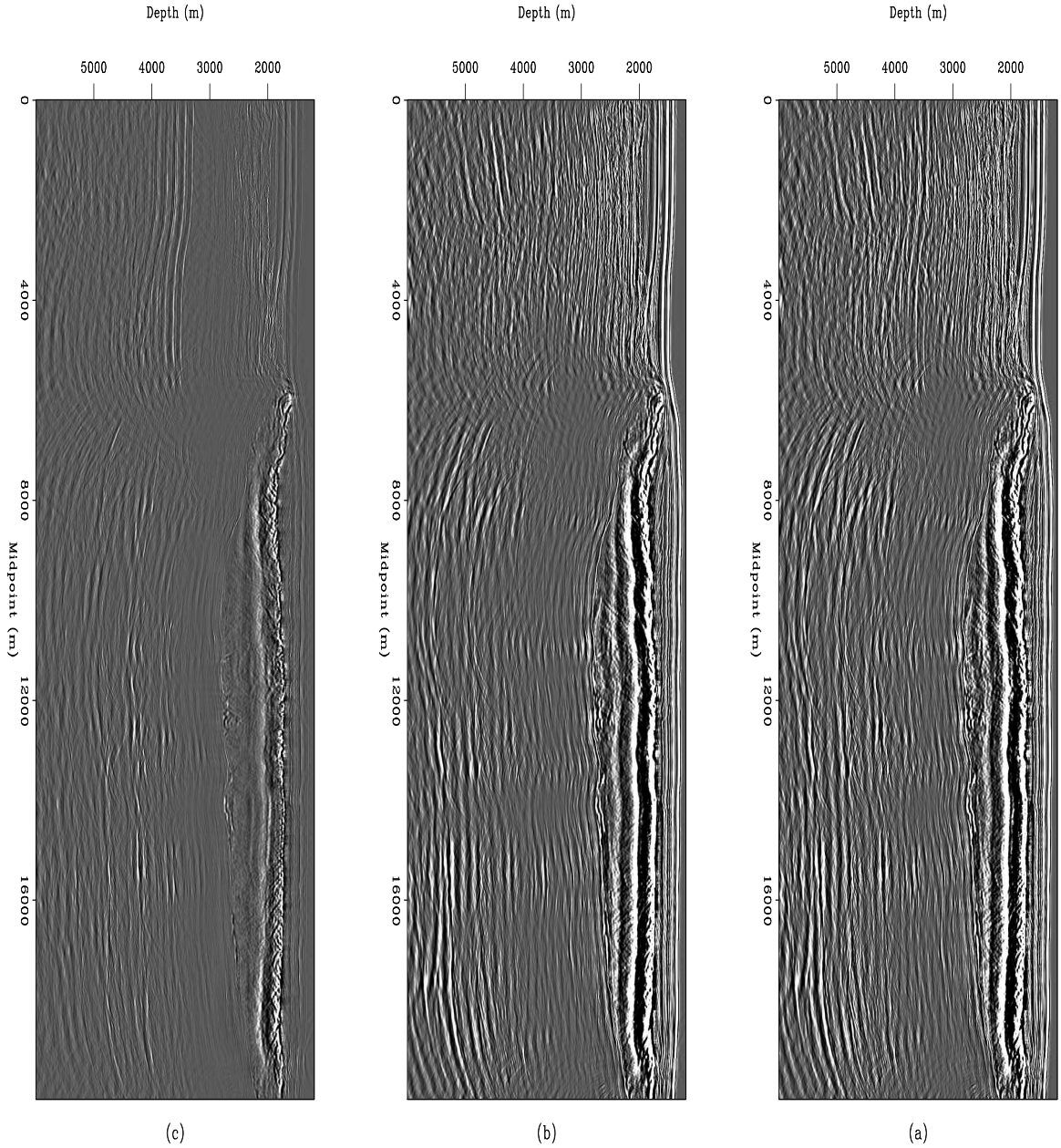

Figure 3.12: Angle stacks after prestack depth migration. Panel (a): Raw data. Panel (b): LSJIMP estimated primaries after inverse NMO. Panel (c): Difference. results2d-stackcomp-weimig.gulf [CR,M]

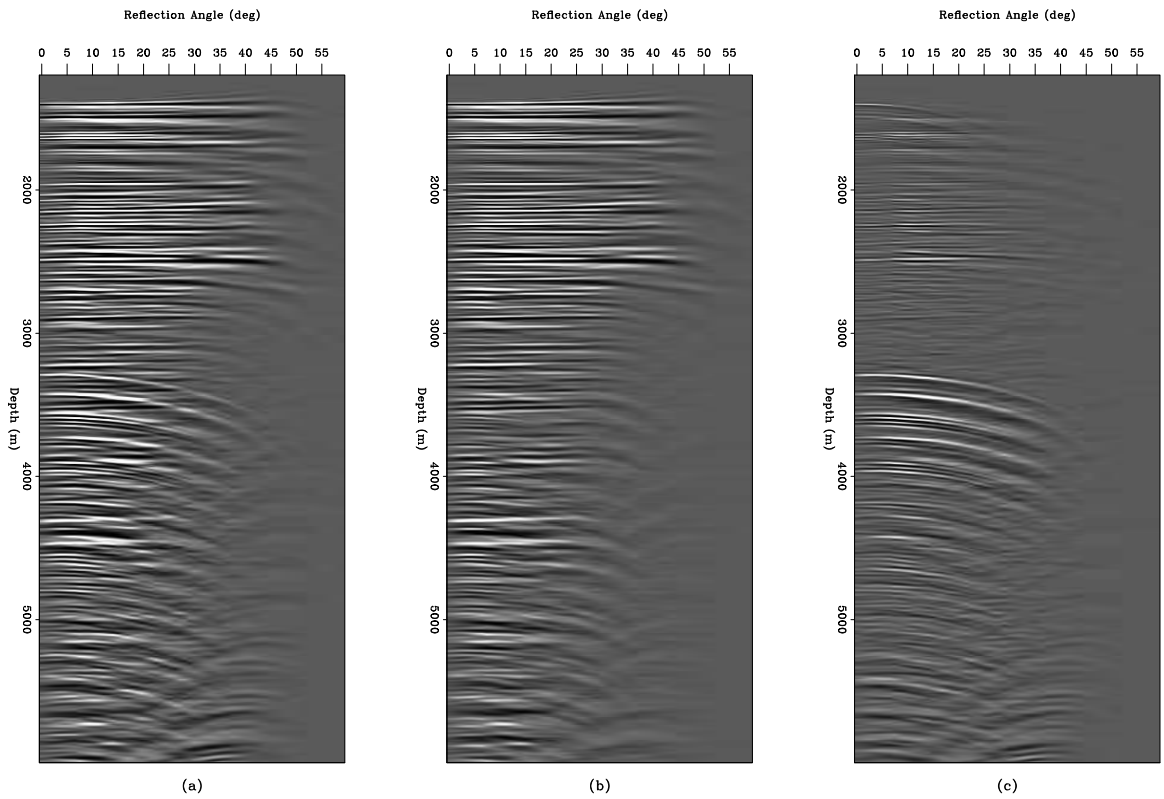

Figure 3.13: Angle gather comparison at CMP 55 of 750. Panel (a): Raw data. Panel (b): LSJIMP estimated primaries after inverse NMO. Panel (c): Difference. results2d-angcomp.weimig.gulf.55 [CR]

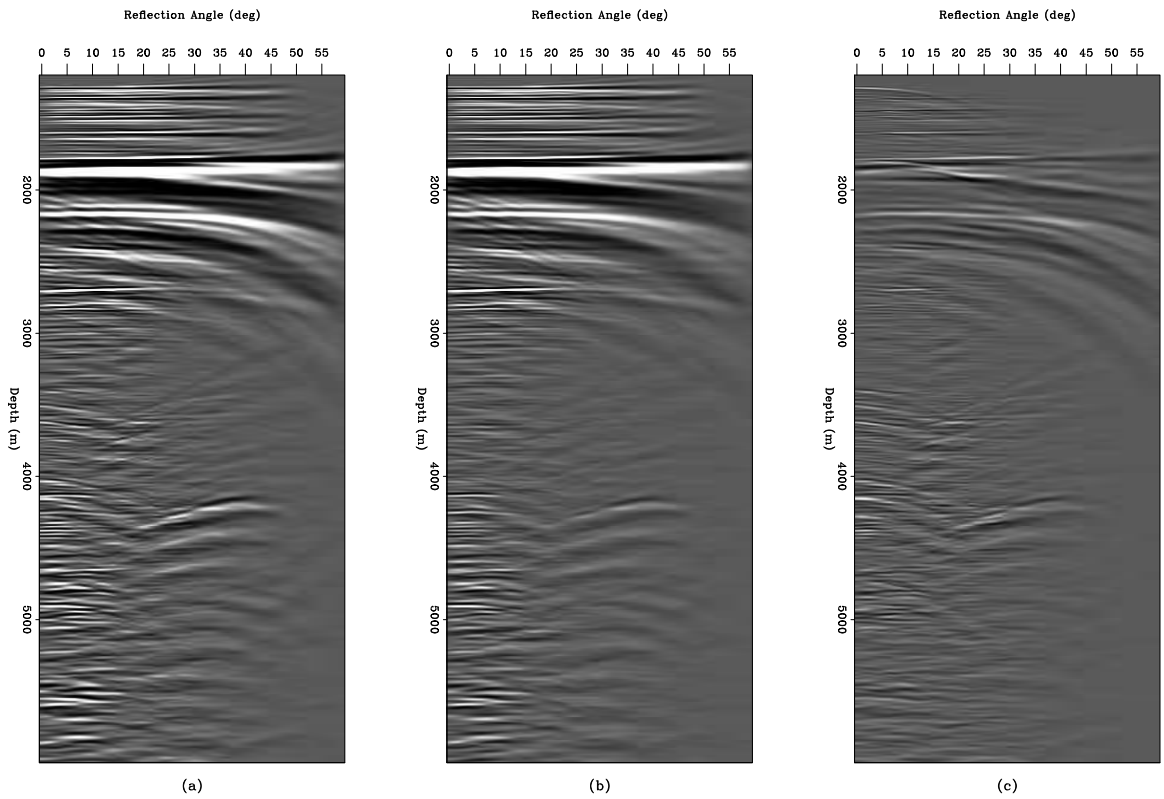

Figure 3.14: Angle gather comparison at CMP 344 of 750. Panel (a): Raw data. Panel (b): LSJIMP estimated primaries after inverse NMO. Panel (c): Difference. results2d-angcomp.weimig.gulf.344 [CR]

individual images ($\mathbf{r}_m^{[1]}$ in equation (2.12)). As a starting guess, I simply "spread" a stacked trace of the primaries across all offsets, for all images. $\mathbf{r}_m^{[1]}$ is roughly a measure of image dissimilarity. As the images are adjusted to fit variations in the data, the images become more dissimilar, and the model residual initially increases, before decreasing slowly with iteration.

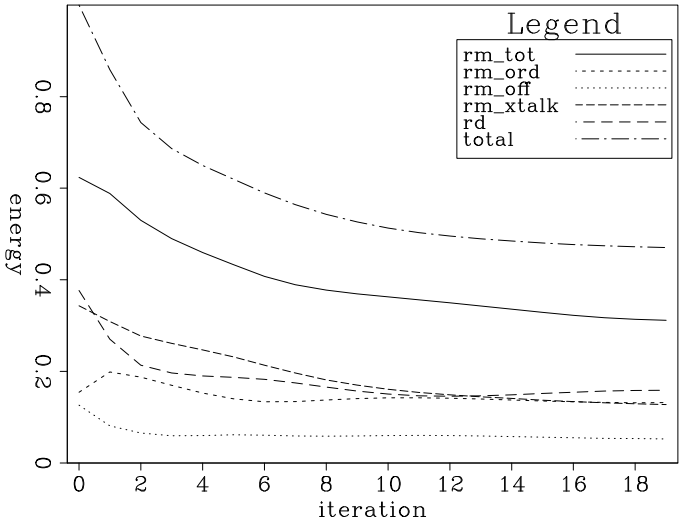

Figure 3.15: Individual data and model residuals as a function of iteration for LSJIMP inversion, CMP 55 of 750. "rm_ord", "rm_off", and "rm_xtalk" derive from $\mathbf{r}_m^{[1]}$, $\mathbf{r}_m^{[2]}$, and $\mathbf{r}_m^{[3]}$ in equation (2.12), respectively, while "rm_tot" is the sum of these residuals. "rd" is the data residual, while "total" denotes the combined LSJIMP residual of equation (2.12). results2d-respow.gulf [CR]

Figure 3.16 compares the data residual and raw data at CMP 55. A somewhat similar comparison was made earlier, in Figures 3.9-3.11, to examine the quality of fit to the multiples, but the earlier portions of the time axis were not shown. At earlier times, notice that the data residual contains some primary energy. The model regularization terms in the LSJIMP inversion cause the misfit. LSJIMP's working definition of "signal" includes events that are perfectly flat with offset on all images (with "smooth" AVO variation) and perfectly self-consistent multiple and primary images. If, for instance, the stacking velocity does not perfectly flatten a primary, or if primary and multiple events are misaligned or mis-modeled in terms of amplitude, we will see some primary energy in the data residual. Furthermore, notice increased misfit at near offsets versus far offsets. As noted in Section 2.2, the model regularization operators are not applied where the multiples provide no information – specifically, as far offsets, as dictated by Snell Resmpling. The fact that we see little to no residual primary energy at far offsets confirms the notion that model regularization terms cause the observed misfit at near offsets.

Figure 3.17 simply shows all nine (four multiple generators, first-order multiples only) panels of the model space at CMP 55. Comparing the primary image ("m0") directly with the

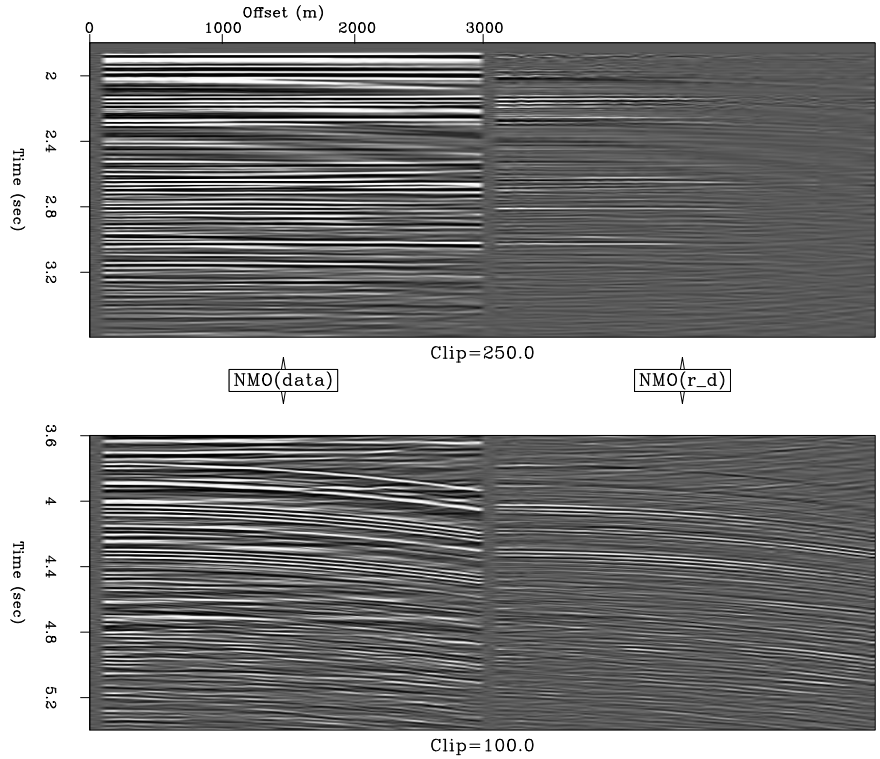

Figure 3.16: Raw data (left) and data residual (right) compared for CMP 55 of 750. NMO with primary stacking velocity applied to facilitate discrimination between multiples and primaries. results2d-resd.gulf [CR]

raw data shown in Figure 3.16, notice that obvious multiples have been strongly, but not totally, suppressed and that two prominent primary reflections between 4.4 and 4.8 seconds uncovered. This Figure and Figures 3.18-3.20, which display the various model residual vectors, have the same graphical layout.

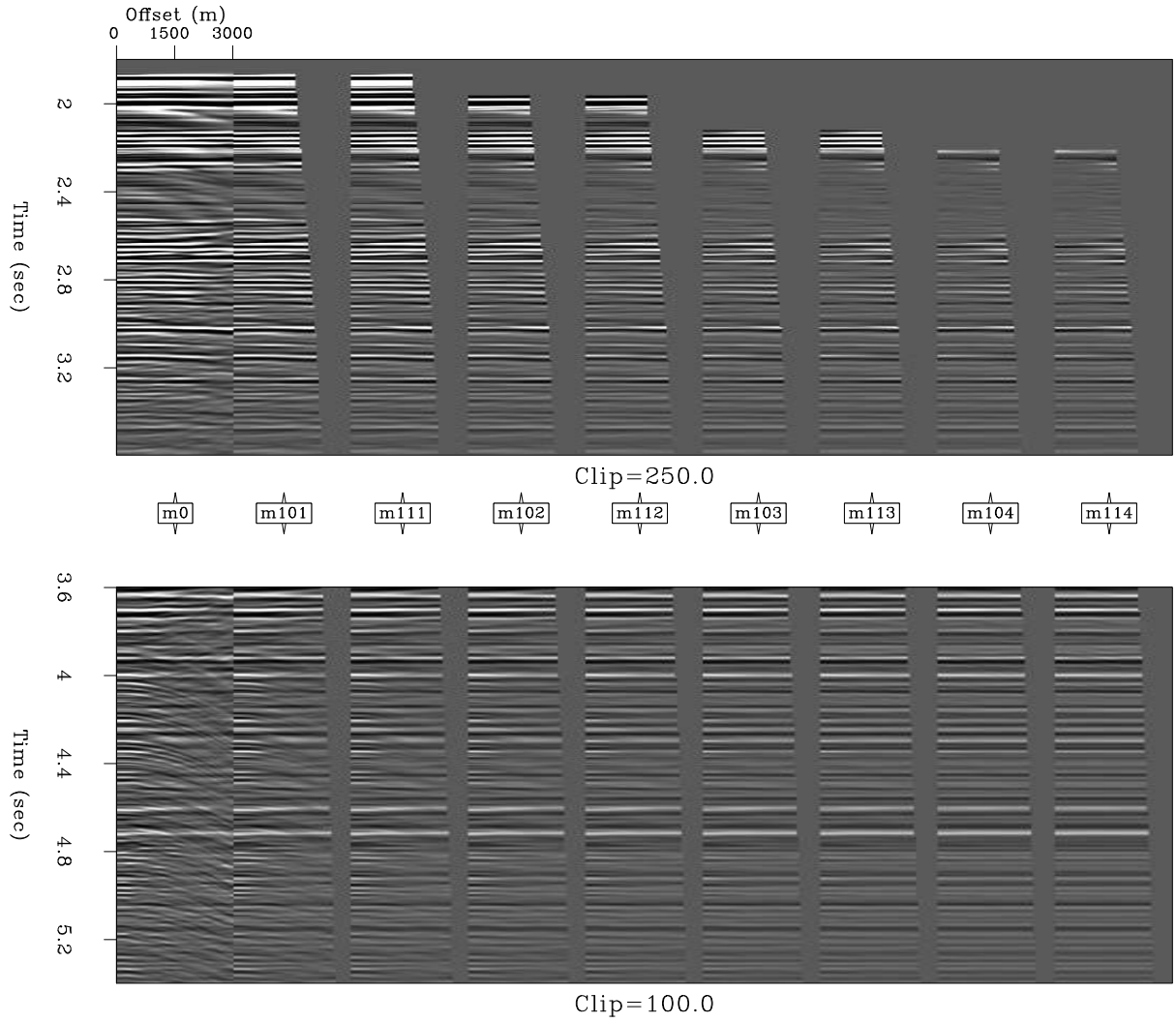

Figure 3.17: LSJIMP model space at CMP 55 of 750. "m0" is the primary image, $\mathbf{m}_0$, while "mikm" corresponds to $\mathbf{m}_{i,k,m}$, the image of the k^{th} split of the i^{th}-order pegleg multiple from the m^{th} multiple generator. results2d-model.gulf [CR]

Figure 3.18 illustrates the model residual corresponding to the differencing across images

regularization operator derived in Section 2.1.4, and to $\mathbf{r}_m^{[1]}$ in equation (2.12). First notice that the last panel, "m114" is blank. The differencing operator subtracts one image panel from the previous, in exactly the left-to-right order shown on the Figure. The difference is not defined for the last image, here "m114". The difference is zero-valued at far offsets, because the multiples provide no information here, as mentioned in the discussion of Figure 3.16. Above the onset of the seabed pure multiple, notice on the residual panels some primary energy, the presence of which can be explained by misalignment of primaries and multiples after imaging or by inaccuracies in the amplitude modeling of the multiples. In theory, after proper imaging, the multiples should be "copies of the primary"; any deviations from this state will appear on the model residual shown in Figure 3.18. At later times, we notice considerable residual multiple energy. As discussed in Section 2.1.4 (Figure 2.1), crosstalk events from one image panel to another do not generally coincide at far offsets.

Figure 3.18 illustrates the model residual corresponding to the differencing across offset regularization operator derived in Section 2.1.5, and to $\mathbf{r}_m^{[2]}$ in equation (2.12). The panels are fairly simple to understand; the differencing filter amplifies high spatial wavenumber events, such as multiples at far offsets, random noise, or non-flat primaries. Notice that the difference is not taken at the far offsets of the multiple panels, where no multiple energy is recorded.

Figure 3.20 illustrates the model residual corresponding to the crosstalk penalty weighting regularization operator derived in Section 2.1.6, and to $\mathbf{r}_m^{[3]}$ in equation (2.12). Conceptually, the panels are easily understood; each is simply the result of applying the crosstalk weight to the corresponding panel of the LSJIMP estimated model (Figure 3.17). In the case of the primary panel, "m0", the weight attempts to penalize all the modeled multiples. In the case of the multiple panels, the weight attempts to penalize multiples from all the other multiple generators.

3.1 SRME versus HEMNO

Verschuur et al. (1992) of Delft University presented a very effective autoconvolutional modeling technique for surface-related multiples, known as the "SRME" (Surface-related Multiple Elimination) method. Assuming sufficiently dense source coverage, as is typical with 2-D

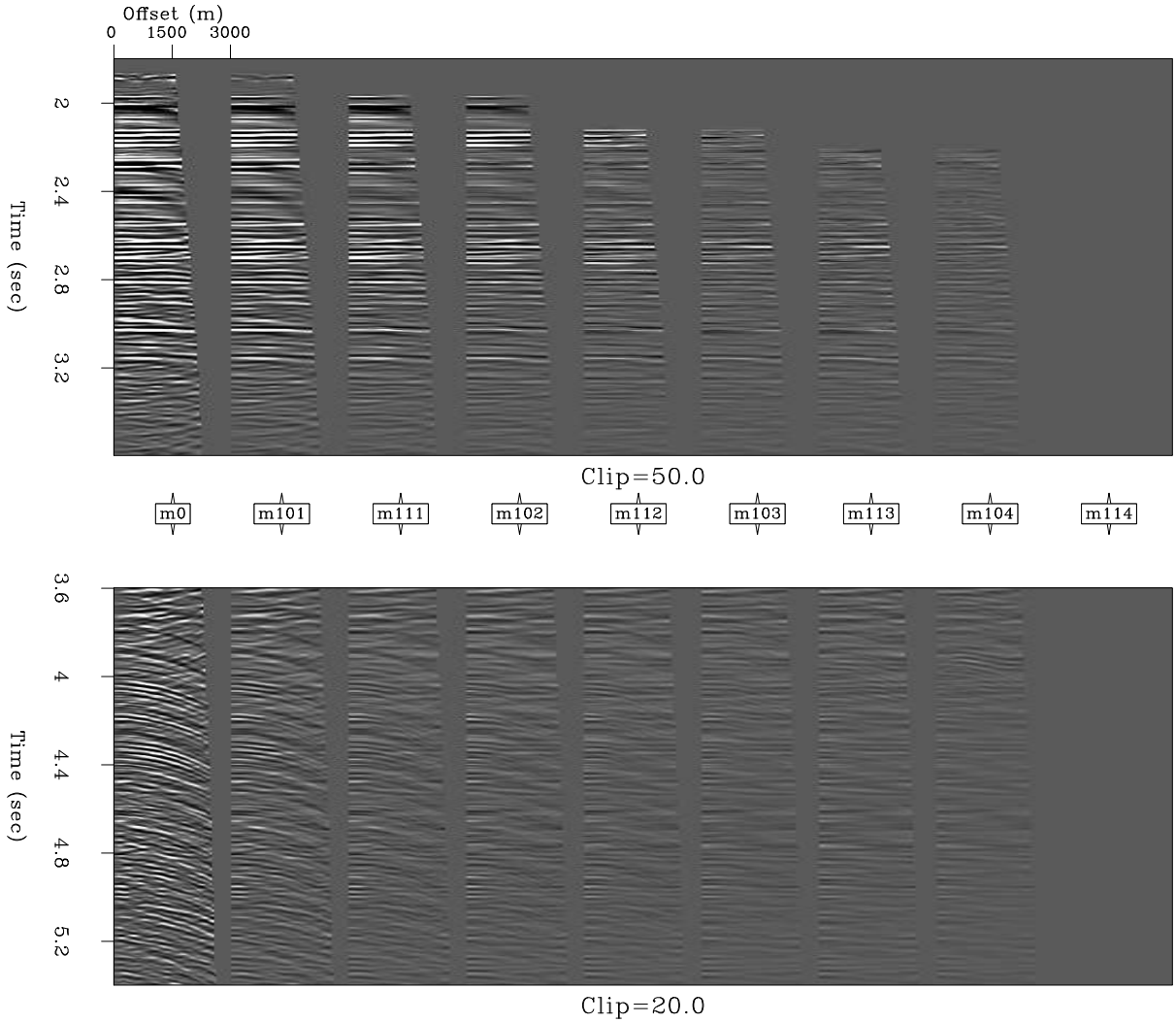

Figure 3.18: LSJIMP model residual $\mathbf{r}_m^{[1]}$ at CMP 55 of 750. Each panel is the difference of one panel of the estimated model and the next panel to the right (see Figure 3.17). results2d-resm.order.gulf [CR]

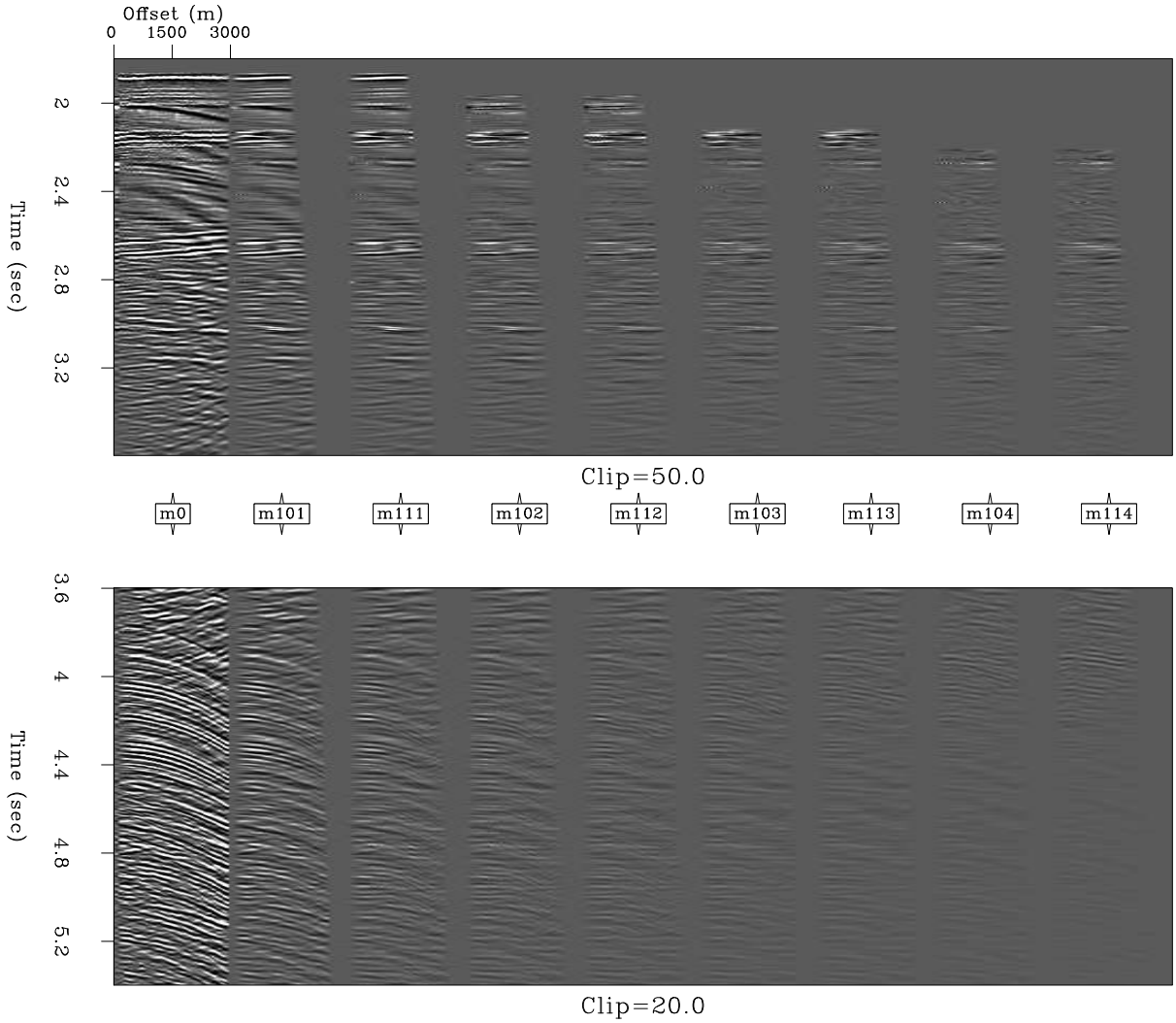

Figure 3.19: LSJIMP model residual $\mathbf{r}_m^{[2]}$ at CMP 55 of 750. Each sample of each panel is the difference of that sample and the adjacent sample in offset, on the corresponding estimated model panel (see Figure 3.17). results2d-resm.offsetx.gulf [CR]

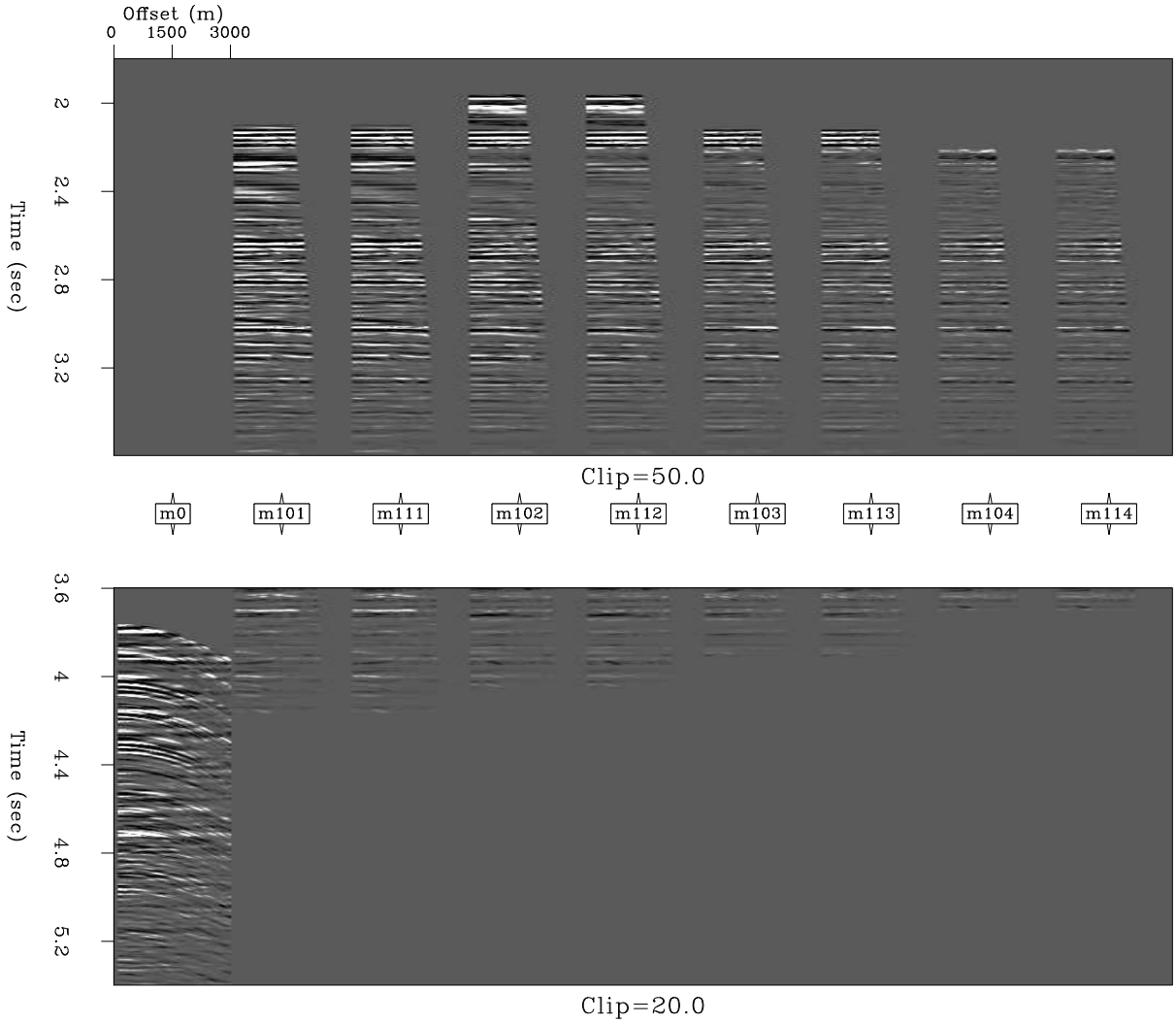

Figure 3.20: LSJIMP model residual $\mathbf{r}_m^{[3]}$ at CMP 55 of 750. Each panel is the result of applying crosstalk weights to the corresponding estimated model panel (see Figure 3.17). results2d-resm.xtalk.gulf [CR]

towed-streamer marine data, the method accurately models all multiples which bounce downward at the acquisition datum, but nowhere else. SRME can model diffracted multiples and other complex events, and most compellingly, requires no prior knowledge of the subsurface geology. Once estimated, the SRME multiple model is usually subtracted from the recorded data by any number of adaptive subtraction techniques.

Postponing a discussion of SRME's limitations with 3-D narrow azimuth marine data until Chapter 4, the method has a number of limitations in 2-D. The method obtains a multiple model by iteratively adding terms of an infinite series, although in practice only one iteration is done. After one iteration, the wavelet of the multiple model will generally be stretched somewhat because it is generated via autoconvolution. Additionally, the near-offset gap of the multiple model is twice that in the data. Since near-offset multiple energy contributes most to the stack, accurate extrapolation of the near-offset traces is crucial. Another limitation of SRME is its tendency to "over-predict" higher-order multiples; this may hamper some subtraction algorithms.

In this section, I compare an SRME multiple model (one iteration), computed by Antoine Guitton, with a multiple model generated by the method outlined previously for the computation of crosstalk (section 2.1.6), using HEMNO as the imaging engine. Figures 3.21 and 3.22 compare the SRME and HEMNO results at CMP locations 55 (1440 m) and 344 (9150 m), respectively. The results of LSJIMP at same CMP locations are shown in Figures 3.9 and 3.10.

Figure 3.21 is taken from the sedimentary basin portion of the Mississippi Canyon data. We first notice the improved near-offset coverage of the HEMNO model. Kinematically, both HEMNO and SRME match the shallow multiple events quite accurately. Deeper in the gather, we see little order to the multiples in the data. Many of the primaries in the 2.5-3.5 second range may come from out-of-plane reflectors or diffractors, hence the multiples of these events will not have the expected kinematics. In 2-D, both HEMNO and SRME assume that all energy propagates in the plane of acquisition. Figure 3.22 is taken from over the salt body. Notice that both the HEMNO and SRME models fairly accurately represent the strong split peglegs from the top of salt reflection.

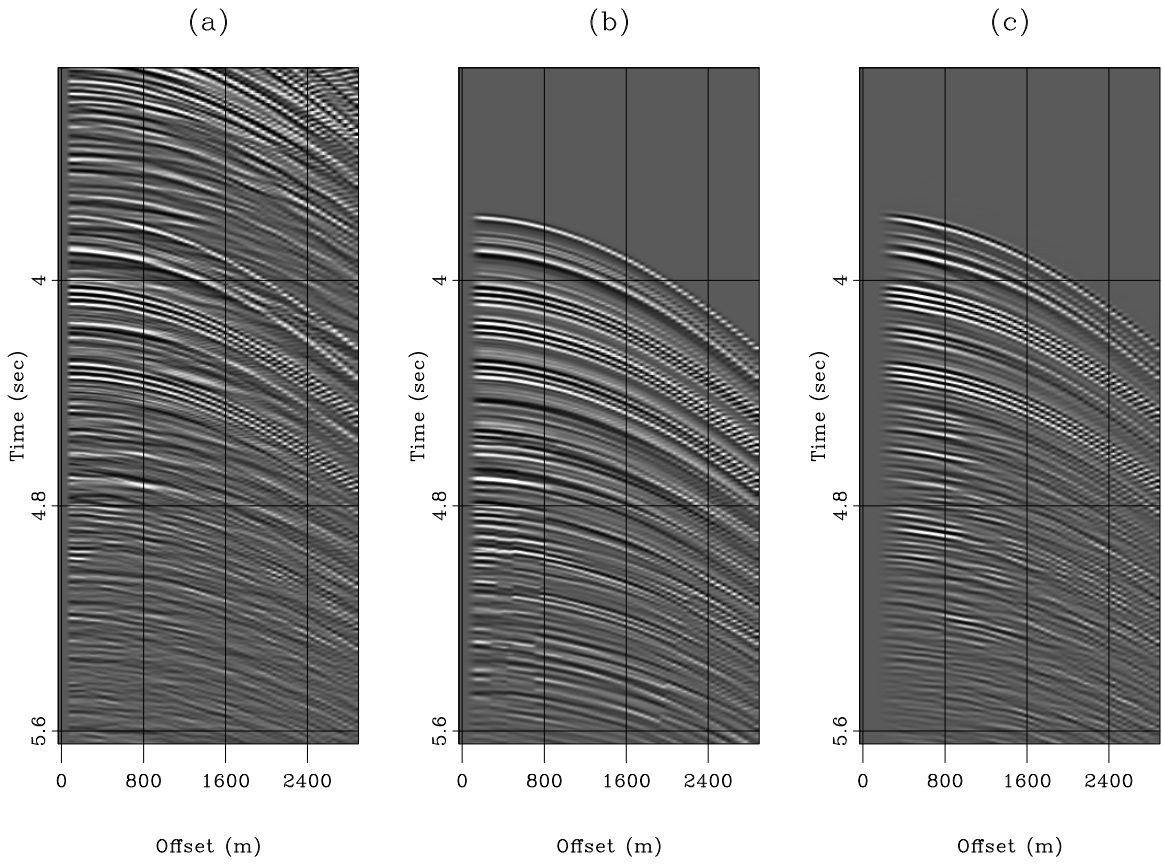

Figure 3.21: HEMNO versus SRME comparison, CMP 55 (1440m). Left: raw data. Center: HEMNO multiple model. Right: SRME multiple model. results2d-delft.comp.55 [CR]

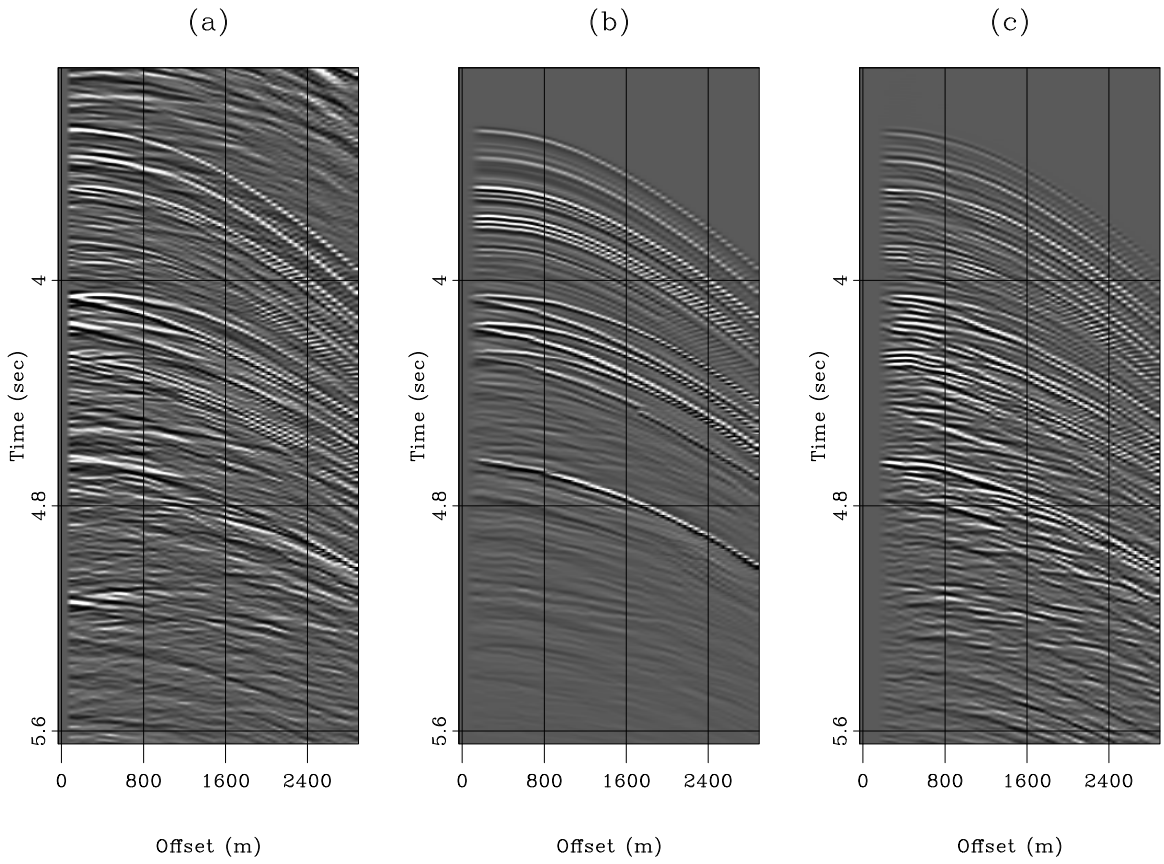

Figure 3.22: HEMNO versus SRME comparison, CMP 344 (9150). Left: raw data. Center: HEMNO multiple model. Right: SRME multiple model. results2d-delft.comp.344 [CR]

Figures 3.23 and 3.24 compare the HEMNO and SRME multiple models on constant-offset sections. Here, we can check each model for correct event positioning–especially important when complex peglegs split. On a near-offset section (Figure 3.23), we see that both methods accurately match the kinematics of the important multiple reflections. The region highlighted by the circle illustrates the stretched wavelet of the SRME model. The region highlighted by the oval shows how the poorly-estimated R1 reflection coefficient has caused an overly strong event to appear in the HEMNO model. On a medium-offset section (Figure 3.24) we again see that both models roughly mimic the multiples in the data. Of special interest is the positioning of split multiple events. In the region highlighted by the circle, all three methods correctly model the split pegleg. The amplitudes on the HEMNO model appear truer to the data. In the region highlighted by the tall oval, we see that the HEMNO model does not accurately represent the data, but the SRME model does. In the region highlighted by the wide oval, we see that SRME better models the diffractions and other features of the complex top of salt pure multiple.

3.2 Playing Devil's Advocate: What do the multiples add?

LSJIMP seeks to exploit another type of multiplicity in the data, that between multiples and primaries. I claimed in Chapter 2 that by adding the model regularization which differences between images (section 2.1.5), we expect that information from the multiples can fill illumination holes or missing trace and also lead to better discrimination between signal and noise. The veracity of this claim is central to the labeling of LSJIMP as a "joint imaging" algorithm. If false, then we conclude that the multiples add nothing to the inversion. I ran a simple test to determine what, if anything, the multiples add to the LSJIMP inversion, I "turn off" the regularization which differences across images by setting $\epsilon_2 = 0$ in equation (2.12). Figures 3.25-3.28 show the results of this test.

Figure 3.25 shows the stack of the estimated primaries, $\mathbf{m}_0$, with $\epsilon_2 = 0$, and can be compared directly with Figure 3.6. Differences are apparent, although subtle. Generally, we notice a loss of coherency in the estimated multiples (difference panel).

More revealing are Figures 3.26 and 3.27, which show a zoomed view of two regions

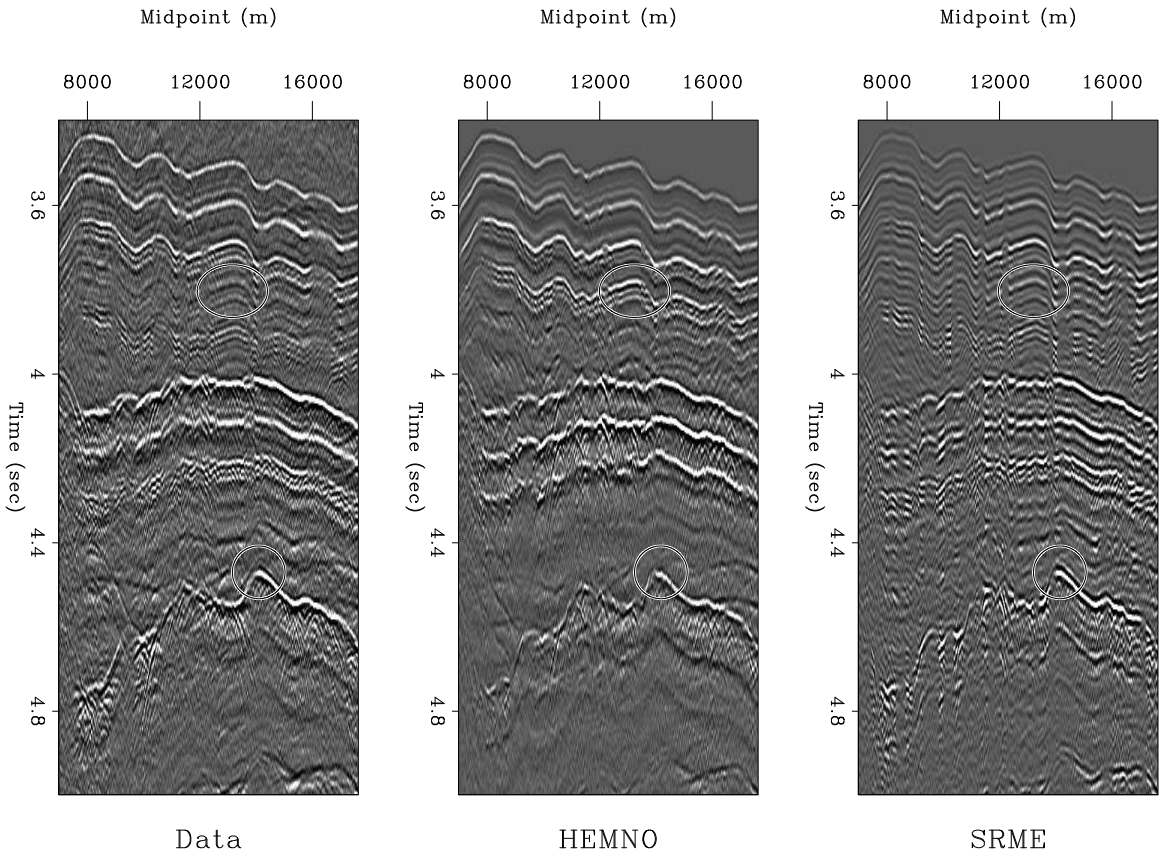

Figure 3.23: HEMNO versus SRME near-offset comparison. Left: raw data. Center: HEMNO multiple model. Right: SRME multiple model. Regions of interest are highlighted. results2d-delft.noffcomp [CR]

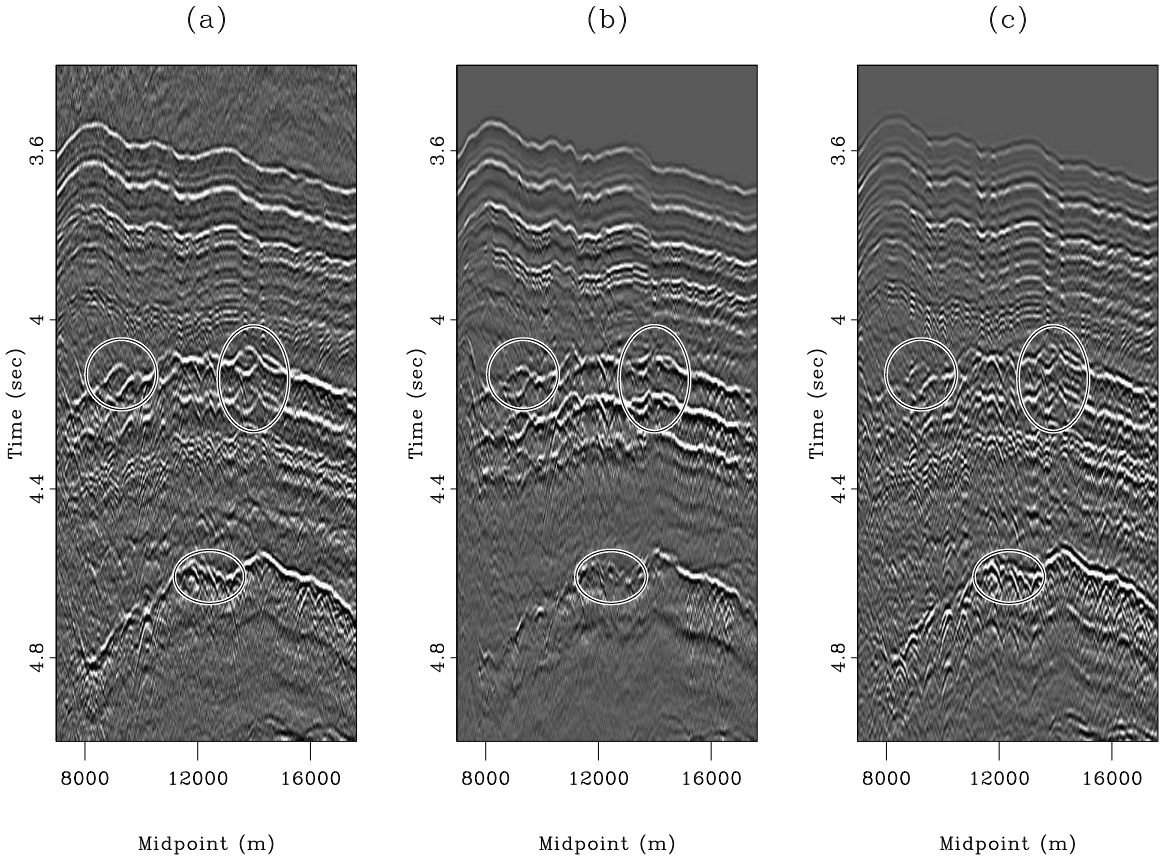

Figure 3.24: HEMNO versus SRME medium-offset comparison. Left: raw data. Center: HEMNO multiple model. Right: SRME multiple model. Regions of interest are highlighted. results2d-delft.moffcomp [CR]

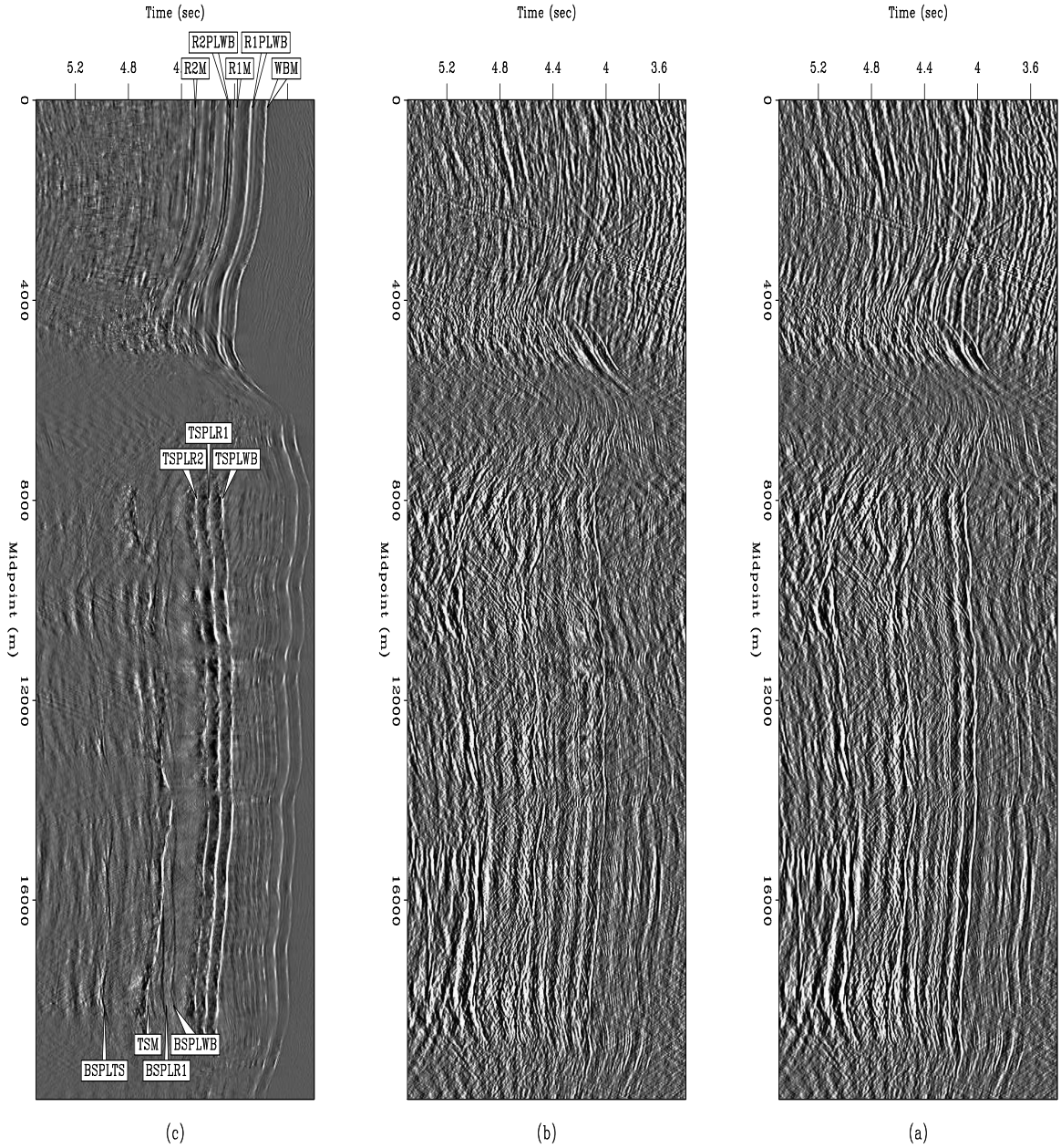

Figure 3.25: Top: raw data stack. Center: estimated LSJIMP primaries stack, with $\epsilon_2 = 0$. Bottom: difference panel (estimated multiples) stack. Compare with Figure 3.6. results2d-stackcomp-devils.gulf [CR,M]

of Figure 3.25, and are directly comparable to Figures 3.7 and 3.8, respectively. Comparing Figure 3.26 to Figure 3.7, we again note a general decrease in estimated multiple coherency when $\epsilon_2 = 0$. We also can see that in regions where multiples overlap primaries, like at 3.7 seconds/1200 meters, setting $\epsilon_2 = 0$ leads to some losses in primary energy. Comparing Figure 3.27 to Figure 3.8, we see that setting $\epsilon_2 = 0$ leads to a generally worse result. Less multiple energy is removed, particularly from some of the salt-related multiples, like TSPLWB and BSPLWB, and again, the subtracted energy is less coherent.

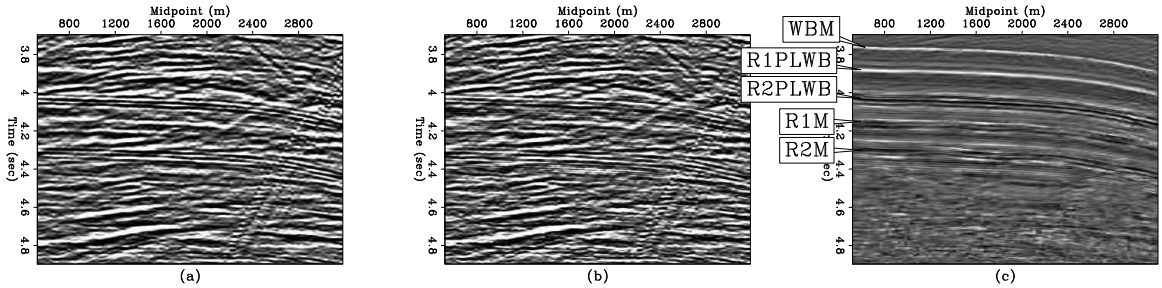

Figure 3.26: Zoom on Figure 3.25, from the sedimentary basin section of the data. Top: raw data stack. Center: estimated LSJIMP primaries stack, with $\epsilon_2 = 0$. Bottom: difference panel (estimated multiples) stack. Compare with Figure 3.7. results2d-stackcomp-devils.zoom.1.gulf [CR,M]

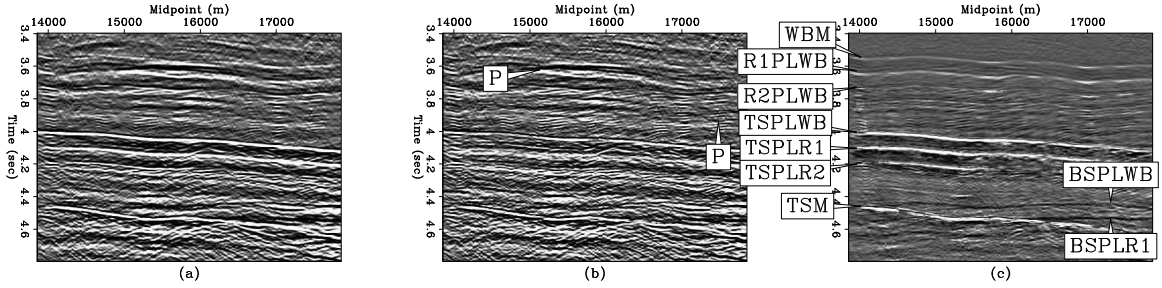

Figure 3.27: Zoom on Figure 3.25, from the subsalt section of the data. Top: raw data stack. Center: estimated LSJIMP primaries stack, with $\epsilon_2 = 0$. Bottom: difference panel (estimated multiples) stack. Compare with Figure 3.8. results2d-stackcomp-devils.zoom.3.gulf [CR,M]

Finally, Figure 3.28 compares the result of setting $\epsilon_2 = 0$ in the prestack sense, at CMP 55 of 750. The left-hand panels compare the estimated primaries with $\epsilon_2 = 1.0$ and $\epsilon_2 = 0$,

while the right-hand panels compare (after NMO) the data residuals for $\epsilon_2 = 1.0$ and $\epsilon_2 = 0$. The panels are split in half vertically and clipped at a different value, labeled on the plot, for display purposes. Comparing the estimated primaries, we see from the small oval that where multiples and primaries overlap, setting $\epsilon_2 = 0$ reduces the quality of the separation. Primaries are less coherent with offset, and the primary panel contains some energy corresponding to the seabed pure multiple. From the larger oval, notice that for the strongest multiples, setting $\epsilon_2 = 0$ leads to poorer separation. Comparing the data residuals, we see from the top pair of ovals that if $\epsilon_2 > 0$, we generally somewhat damage the primaries, which we expect if we have velocity errors, mis-alignment between imaged primaries and multiples, or incorrect reflection coefficient. This issue was discussed earlier, in section 3.0.2. However, we also note from the lower pair of ovals, that setting $\epsilon_2 = 0$ seems to have reduced our ability to accurately model the important multiples.

3.3 Nonlinear Iteration Test

In this section I test the nonlinear iteration outlined in section 2.1.8 on the Mississippi Canyon data. I ran only one nonlinear iteration. Since the velocity model is already quite nicely determined, I did not do residual velocity analysis after the first run of LSJIMP. However, I did recompute the crosstalk weights and the reflection coefficients for each of the four multiple generators.

The updated crosstalk weights are shown in Figure 3.29, at CMP 55 of 750. The most notable difference after the nonlinear update is the infill of the near offsets. Although invisible in this case, the nonlinear update also allows us to model crosstalk energy below twice the onset of the first seabed multiple, which would be 7.5 seconds. This ability is very important for data recorded in shallower water.

Figure 3.30 compares the weighted data residual at CMP 55 of 750 before and after the nonlinear update. The Figure is split in half along the time axis as explained earlier in section 3.0.2. The most striking differences are highlighted with ovals. As mentioned earlier, the R1 pure multiple and R2 seabed pegleg overlap over most of the 2-D line, which inhibits estimation of R1's reflection coefficient. Although I do not show the updated R1 reflection

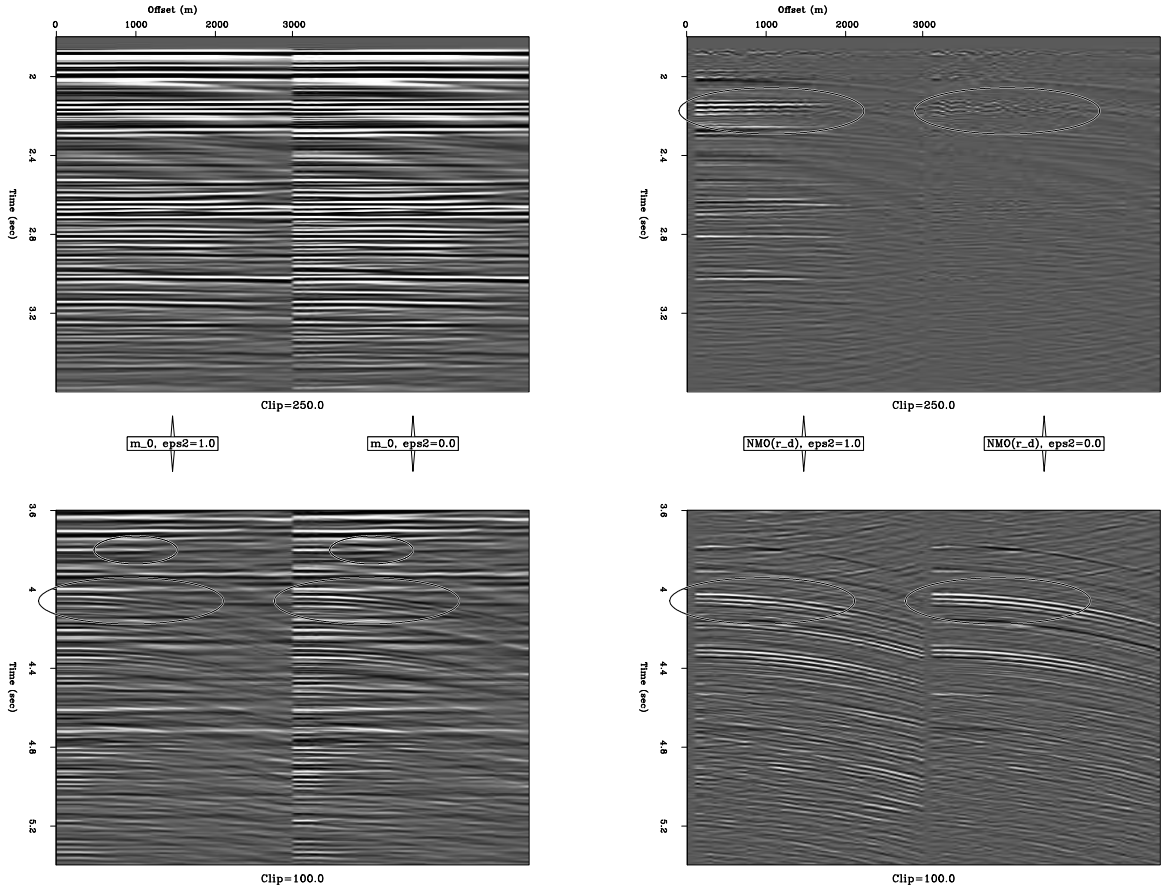

Figure 3.28: Left-hand panels: Estimated LSJIMP primaries at CMP 55 of 750, with $\epsilon_2 = 1.0$ and $\epsilon_2 = 0.0$. Right-hand panels: Weighted data residuals at CMP 55 (after NMO) with $\epsilon_2 = 1.0$ and $\epsilon_2 = 0.0$. Left-hand and right-hand panels split in half along time axis and clipped independently for display clarity. results2d-devils.gulf [CR,M]

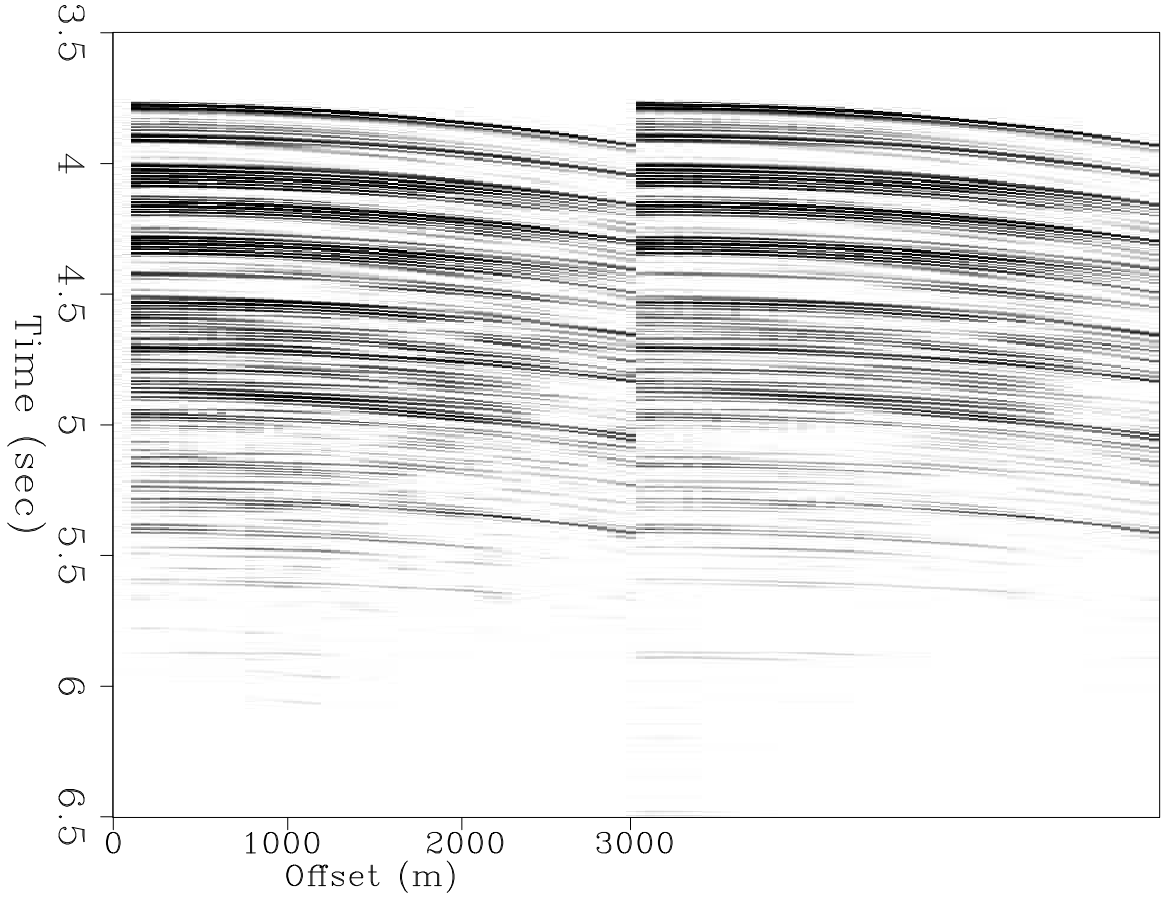

Figure 3.29: Crosstalk weights at CMP 55 of 750, before and after one nonlinear update. Left: Crosstalk weights before update. Right: Crosstalk weights after update. results2d-crosstalk.gulf.iter [CR,M]

coefficient, Figure 3.30 implicitly illustrates the beneficial change. The event highlighted in ovals on the residual panels, which has three visible peaks, does not have that wavelet shape in the raw data. Crosstalk between the overlapping events and an improperly high R1 reflection coefficient cause the event to be "manufactured" in the LSJIMP result. By better estimating the R1 reflection coefficient, the event is not present in the residual, and thus, not manufactured by LSJIMP. Other that this event, however, the differences between the two panels are minimal.

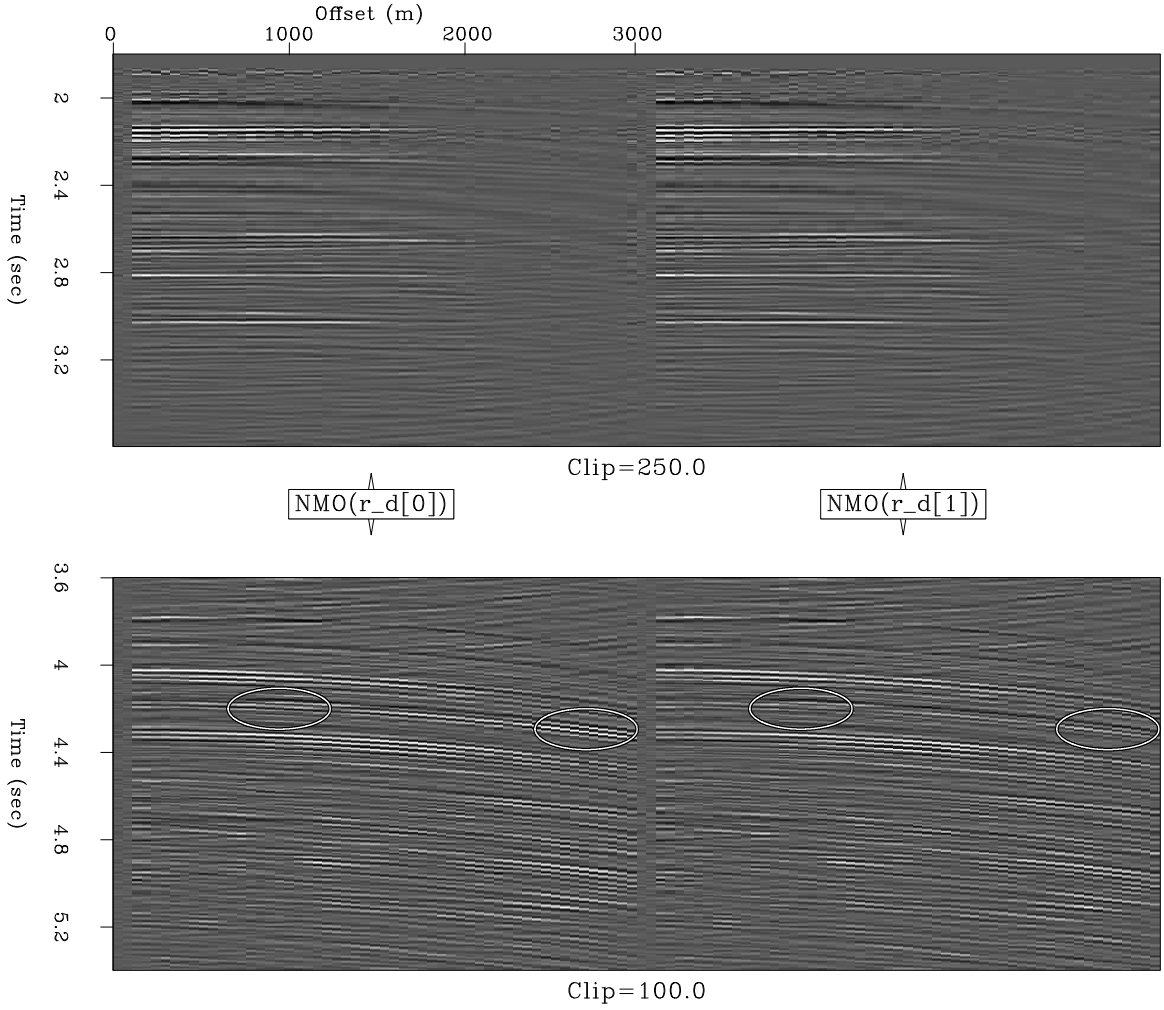

Figure 3.30: LSJIMP data residual before and after nonlinear update of crosstalk weights and reflection coefficients. Left: residual before updating. Right: residual after updating. Panels split in half along time axis for display purposes and clipped as labeled. results2d-resd-iter1.gulf [CR,M]

Figure 3.30 compares the LSJIMP estimated primaries at CMP 55 of 750 before and after the nonlinear update. The Figure is split in half along the time axis as explained earlier in section 3.0.2. Ovals highlight the same regions as were highlighted in Figure 3.30. The differences between the two estimated primary panels are quite subtle; the difference panel on the right is more englightening. Notice how the manufactured event discussed earlier is better suppressed after the nonlinear update.

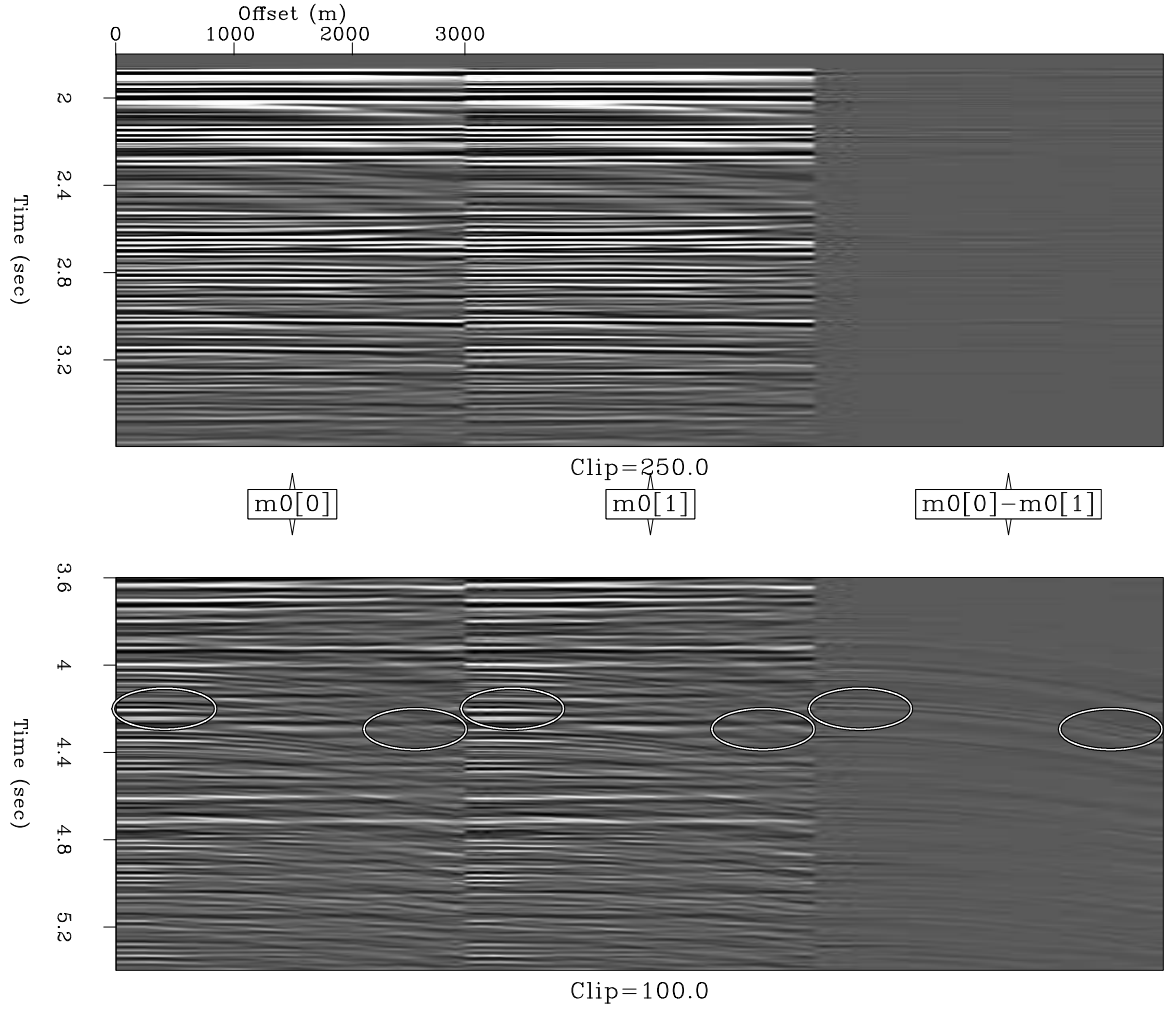

Figure 3.31: LSJIMP estimated primaries before and after nonlinear update of crosstalk weights and reflection coefficients. Left: $\mathbf{m}_0$ before updating. Center: $\mathbf{m}_0$ after updating. Right: Difference. Panels split in half along time axis for display purposes and clipped as labeled. results2d-model-iter1.gulf [CR,M]

Finally, Figure 3.32 shows the stack of the LSJIMP estimated primaries after the nonlinear update. The Figure is directly comparable with Figure 3.6. Again, the differences are quite subtle. Notice an improvement in the removal of deep, salt-related multiple events, like BSPLTS.

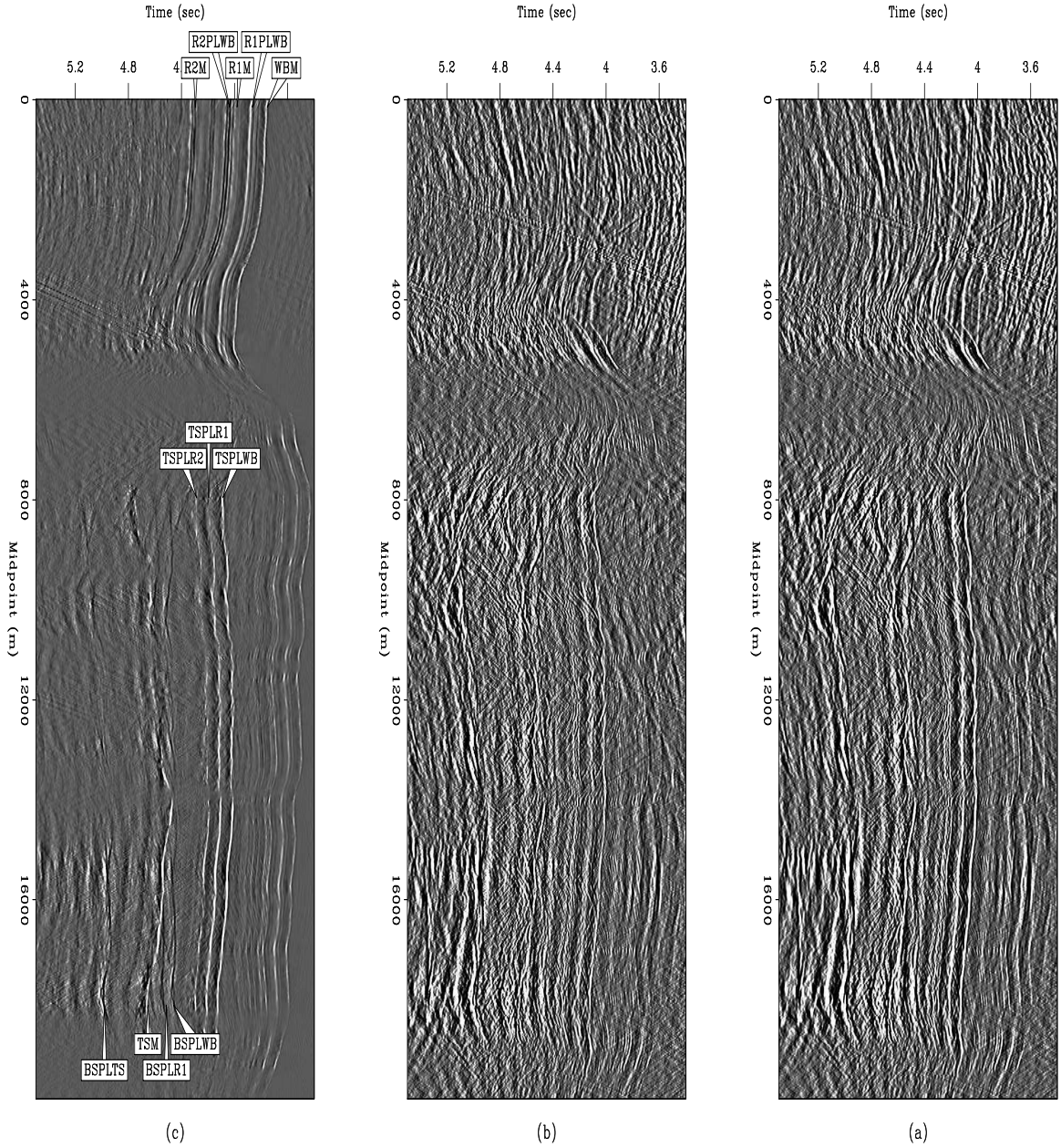

Figure 3.32: Top: raw data stack. Center: estimated LSJIMP primaries stack after nonlinear updating of crosstalk weights and reflection coefficients. Bottom: difference panel (estimated multiples) stack. Figure annotated and displayed with same gain and clip as Figure 3.6. results2d-stackcomp-iter1.gulf [CR,M]

Chapter 4

3-D Theory

In marine environments, three-dimensional reflection seismic data is normally acquired in a so-called "wide tow" streamer configuration, illustrated in Figure 4.1. Ironically, the crossline offset range of this data is less than with most land acquisition geometries, so geophysicists often call towed streamer data "narrow azimuth" data. Note that the crossline shot interval, Δs_y, is chosen such that the outermost receiver line on one swath overlaps the innermost receiver line on the previous swath. Figure 4.2 illustrates that such an acquisition geometry produces a regularly sampled crossline CMP axis, if cable feathering is absent. In one sense, this geometry boasts some degree of optimality, as it produces a well-sampled 3-D image at a minimum cost.

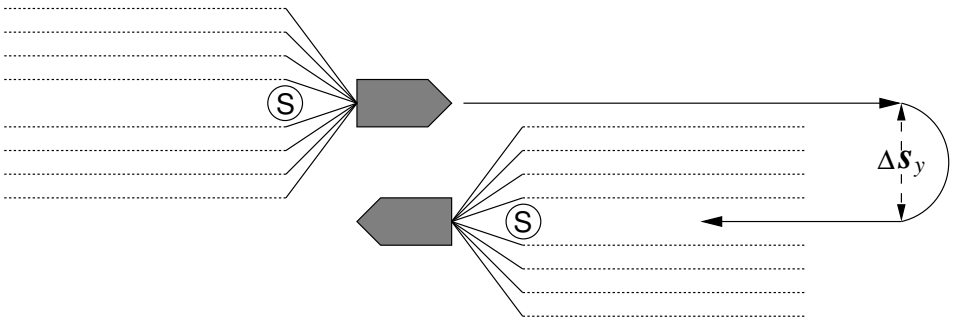

Figure 4.1: Wide tow marine geometry. The acquisition boat tows many (usually 4-12) receiver lines and steams in parallel sail lines. theory3d-narrow-az [NR]

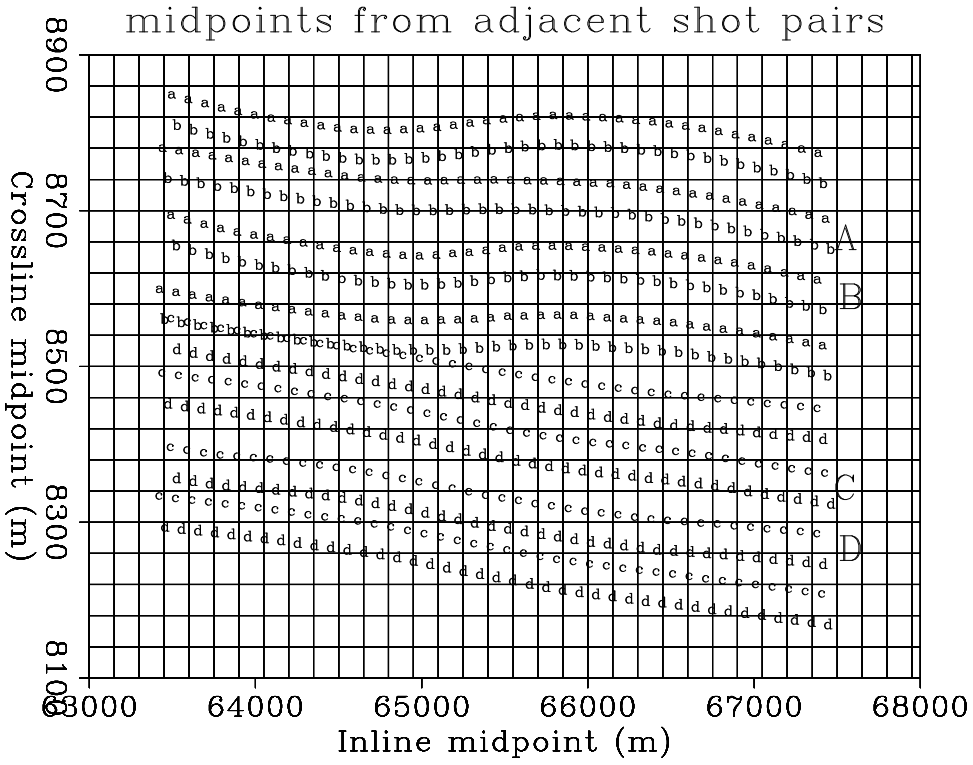

Figure 4.2: Midpoint locations from two adjacent sail lines of the CGG Green Canyon 3-D dataset. The boat tows four streamers and fires two sources alternatively in a "flip-flop" configuration. Midpoints from shot "A" are labeled "a", and so on. Two shot pairs from each sail line are shown. For a fixed ship speed, this geometry doubles crossline midpoint density, at the cost of reduced inline resolution, compared to a single-source configuration. Flip-flop shooting allows one airgun to be recharged while the other shoots, thereby allowing the ship to sail faster than would be possible with one gun. Cable feathering is evident, though not severe. theory3d-cgg-midpoints [NR]

Unfortunately, geometry shown in Figure 4.2 causes the 3-D extension of the SRME method of multiple prediction to fail spectacularly. SRME requires Δs_y to be relatively small–in practice, roughly the same as commonly chosen crossline receiver line spacing parameters (van Borstelen, 2003). 3-D field datasets commonly have a crossline shot interval of up to ten times the crossline receiver line spacing. Workarounds for the 3-D sampling problem include: ignoring crossline structure and using a 2-D prediction, massive (270,000 CPU hours) shot interpolation (Kleemeyer et al., 2003), sparse inversion of the crossline multiple contribution gathers (van Dedem and Verschuur, 2002; Hokstad and Sollie, 2003), and novel acquisition geometries (Paffenholz, 2003). Currently, none of these methods combines proven accuracy with computational/cost efficiency.

The LSJIMP method has good potential to separate 3-D peglegs from wide tow marine data. In Section 3.1, I demonstrated how, in a fairly complex 2-D setting, the HEMNO equation can model some complex multiples as accurately as SRME. In this chapter, I outline a practical extension of my implementation of LSJIMP to work on 3-D wide tow marine data.

4.1 LSJIMP and wide tow marine data

For the particular geometry shown in Figures 4.1 and 4.2, notice that each crossline midpoint gather is occupied by one, and only one receiver line. Therefore, we can conceptualize a 3-D CMP gather as a 2-D CMP gather with nonzero crossline offset, and thus remove the crossline offset axis from five-dimensional CMP-sorted data, saving considerable memory and computational waste. This approach is similar to Biondi's (1997) combination of azimuth moveout (AMO) (Biondi et al., 1998) and common-azimuth wave equation depth migration (Biondi and Palacharla, 1996) for the prestack imaging of primaries in data with narrow-azimuth geometries. Unfortunately, the AMO transformation is not generally valid for multiples.

HEMNO is well-suited to image multiples with the data geometry described above, primarily because HEMNO images pegleg multiples with a vertical time shift. Rather than correlating wavefields across possibly-undersampled axes like migration, HEMNO uses a measurement of the data's zero-offset time dip to account for structure-induced moveout variations. Because the crossline offset axis is removed, the computational cost increase of applying

HEMNO to 3-D data versus 2-D data is only proportional to the number of crossline midpoints.

My particular LSJIMP implementation, presented in Section 2.2.9, uses HEMNO, in conjunction with three amplitude normalization operators to produce a "true amplitude" image of pegleg multiples. From Figure 2.5, recall that Snell Resampling moves multiple energy across offset to make the multiple's AVO response comparible with its primary. For this reason, the use of Snell Resampling in the crossline direction runs contrary to the stated assumption that we store only one crossline offset bin per 3-D CMP gather. Therefore, in this thesis, I do not apply crossline Snell Resampling for narrow-azimuth data. In practice, little useful angular information is anyway obtained in the crossline direction, since in most cases the data will have a maximum crossline offset of merely a few hundred meters.

4.2 Modifications to the 2-D Theory

In this section I enumerate the necessary modifications to my particular LSJIMP implementation, presented earlier in section 2.2, to move from 2-D data to 3-D data. The narrow azimuth geometry illustrated in this chapter considerably simplifies this move, but for completeness, I nontheless discuss both the narrow azimuth and general 3-D implementations.

- **Regularization operators:** In section 2.1.3 I introduced the three LSJIMP regularization operators. The first (differencing between images, section 2.1.4) and third (crosstalk penalty weights, section 2.1.6) extend to 3-D with no modification. However, in the full 3-D case, the second operator, which differences across offset (section 2.1.5), must operate along both inline and crossline offset axes. Thus the corresponding model residual [equation (2.8)] becomes a vector quantity, as it is nothing more than a finite difference spatial gradient. As mentioned earlier, in the narrow azimuth case, the crossline offset axis is ignored, in which case the operator is the same as in the 2-D case.

- **1-D Imaging of multiples:** The 1-D imaging operator for multiples, derived in section 2.2.1 changes in 3-D. For the full 3-D case, the NMO equation for both primaries and multiples changes. In equations (2.16) and (2.18), the squared inline offset (x^2) changes

to the sum of the squared inline (x_1^2) and crossline offsets (x_2^2):

$$x^2 \Rightarrow x_1^2 + x_2^2, \tag{4.1}$$

where $x_1^2 + x_2^2$ is the squared norm of the offset vector $[x_1\ x_2]^T$. Equation (4.1) applies to the full 3-D and narrow azimuth cases alike. The difference is in the implementation: in the full 3-D case, a computer program loops over the x_2 axis, but not in the narrow azimuth case, where the crossline offset at a given CMP location must be pre-defined and passed as an input parameter.

- **Amplitude correction operators:** An important quantity for my implementation of LSJIMP was x_p, the width of the primary leg of a pegleg multiple [equation (2.21)]. Like the offset vector in 3-D, x_p also becomes a vector quantity:

$$x_p \Rightarrow \begin{bmatrix} x_{p,1} \\ x_{p,2} \end{bmatrix} = \begin{bmatrix} \frac{x_1 \tau V_{\text{rms}}^2}{\sqrt{(\tau + j\tau^*)^2\ V_{\text{eff}}^4 + (x_1^2 + x_2^2)(V_{\text{eff}}^2 - V_{\text{rms}}^2)}} \\ \frac{x_2 \tau V_{\text{rms}}^2}{\sqrt{(\tau + j\tau^*)^2\ V_{\text{eff}}^4 + (x_1^2 + x_2^2)(V_{\text{eff}}^2 - V_{\text{rms}}^2)}} \end{bmatrix}. \tag{4.2}$$

  As noted earlier in this chapter, with narrow azimuth data it makes the most sense not to do Snell Resampling in the crossline direction. Still, the crossline offset of the "reduced" CMP gather may still be nonzero, and will affect the value of $x_{p,1}$.

  The differential geometric spreading correction derived in section 2.2.4 remains unchanged, with the exception of substituting equation (4.1) for squared offset in equations (2.23) and (2.24).

  The estimation of a multiple generator's reflection coefficient in 3-D remains similar to the 2-D case, although the model is a function of two varibles, CMPx and CMPy, and the data may (full 3-D) or may not (narrow azimuth) be a function of crossline offset.

- **HEMNO:** HEMNO is strongly dependent on the quantity x_p derived in section 2.2.3 [equation (2.21)]. The zero-offset traveltimes to multiple generator and reflector and the effective velocity are measured at midpoints y_m and y_p, defined specifically for the

first-order S102G pegleg in equation (2.26), can be rewritten:

$$y_m \Rightarrow \begin{bmatrix} y_0 - x_{p,1}/2 \\ y_0 - x_{p,2}/2 \end{bmatrix} \quad \text{and} \quad y_p \Rightarrow \begin{bmatrix} y_0 + (x_1 - x_{p,1})/2 \\ y_0 + (x_2 - x_{p,2})/2 \end{bmatrix}. \tag{4.3}$$

An accurate 3-D dip estimate is also required. Event tracking in 3-D is just as straightforward as in 2-D The only other change required to HEMNO is to change squared inline offset in equation (2.27) to the squared norm of the offset vector, equation (4.1).

Chapter 5

3-D Results

5.1 CGG Green Canyon IV 3-D Data

In 2003, CGG donated a large portion of a 161-block speculative seismic survey it acquired in the Green Canyon region of the Gulf of Mexico. The data were acquired in the transition zone between the edge of the Continental Shelf and the Sigsbee escarpment which signals the edge of the abyssal plain. Geologically, the Green Canyon region is characterized by sedimentary "minibasins" interrupted by complex salt bodies (AAPG, 1998).

CGG's 3-D data were acquired by a ship sailing east-to-west, in the strike direction relative to the dominant geologic dip. The subset of the data that I process in this thesis contain fairly significant crossline dip ($> 3°$) in most places. Figure 5.1 shows a stacked section of the subset, which contains 192 midpoints inline and 14 midpoints crossline. The stacked section includes contributions from two adjacent sail lines, the geometry of which is illustrated in Figure 5.2.

The subset shown in Figure 5.1 is situated in a sedimentary minibasin, with strong reflections visible at a two-way traveltime of well over 5 seconds. Thanks to a strong velocity gradient and the sparse offset sampling, surface-related multiples are largely absent from the stacked section. Still, as we shall see, the multiples are fairly strong in the prestack data, and would likely inhibit prestack amplitude analysis. The section exhibits moderate reflector dip,

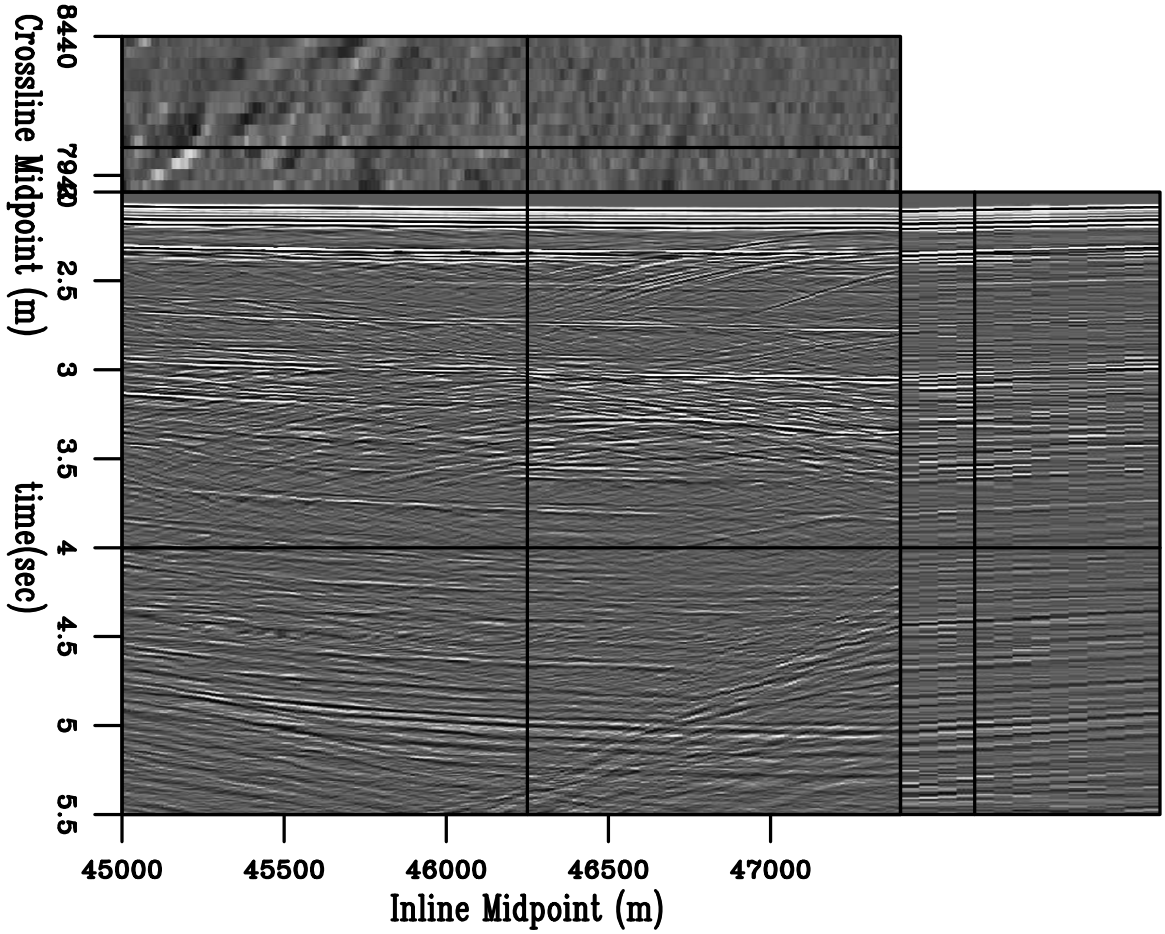

Figure 5.1: Stacked section of subset of Green Canyon IV 3-D dataset processed in this chapter. results3d-stackraw3d.gc3d [CR]

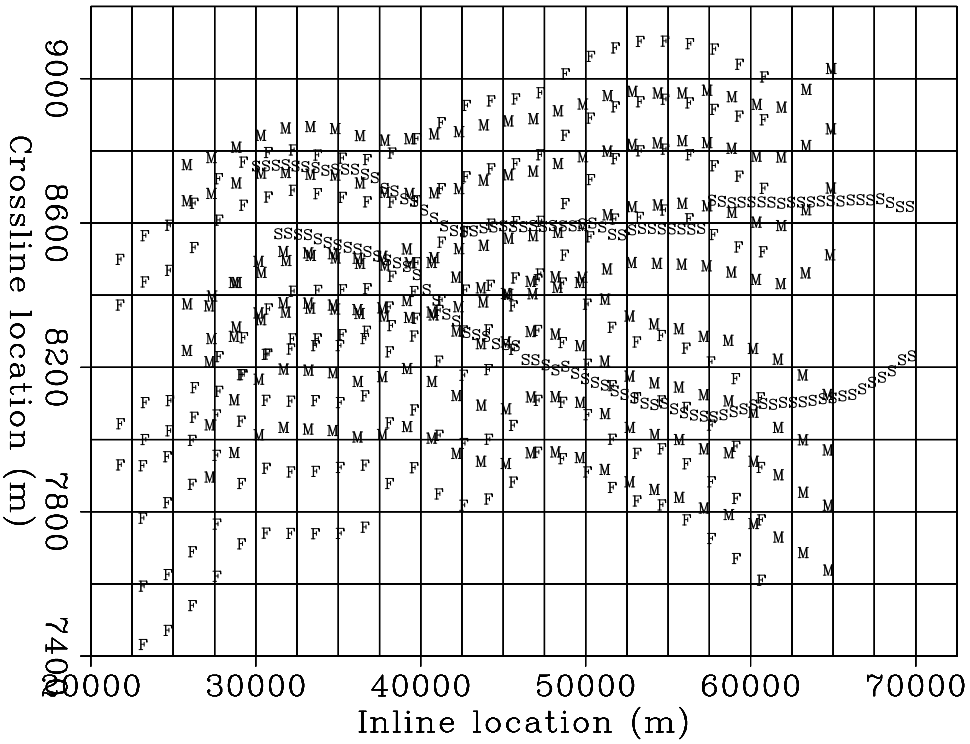

Figure 5.2: Acquisition geometry for two sail lines contributing to subset shown in Figure 5.1. "S" symbols illustrate source positions. "M" and "F" symbols illustrate the medium- and far-offset receivers, respectively, on each of the boat's four streamers. The nominal sail line spacing is 300 meters, although it varies considerably in this case from about 200 to 500 meters. The subset processed in this section contains shot records from about 40,000 to 50,000 meters inline location. Cable feathering in this zone is present, though not severe. Although they are not supposed to, the two sail lines overlap to some extent, which reduces the number of crossline midpoint locations from these two sail lines to 14 from 16 over the subset. results3d-feather [NR]

from an anticlinal structure in the inline direction and an effectively constant crossline dip of several degrees.

The acquisition ship sailed quite fast, with a flip-flop source interval of 37.5 meters, and an interval of 75 meters between like sources. The fast ship speed leads to reduced resolution along the inline offset axis: for an 8100-meter cable with receiver group spacing of 25 meters, the nominal fold is only 54, implying a nominal inline offset spacing of 150 meters. Figure 5.3 illustrates the sparse sampling of the inline offset axis. While the nominal inline offset bin size of 150 meters ensures that all bins will contain a live trace, such sparsity will greatly inhibit the estimation of reasonable stacking velocities and create "checkerboard" artifacts in the shallow portions of a stacked image.

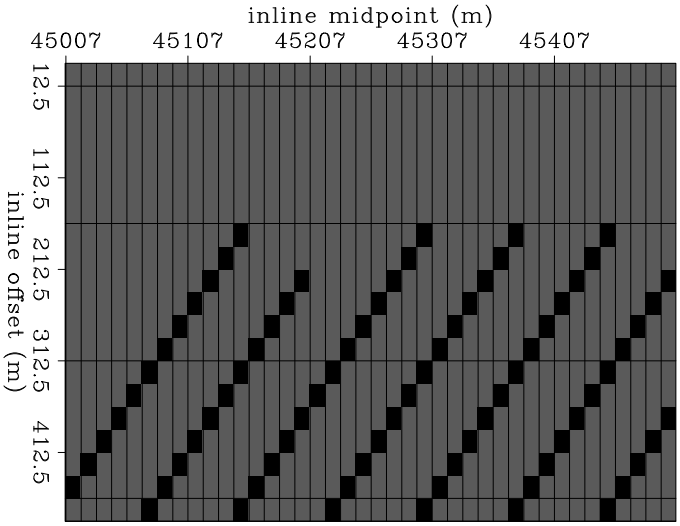

Figure 5.3: Illustration of sparsity of inline offset axis of CGG Green Canyon IV data. Grid represents nominal bin size of 150x12.5 meters. Black dots correspond to trace locations. results3d-sparse.gc3d [ER]

Therefore, in my processing of this dataset, I use an offset bin spacing of 25 meters. While this fine sampling better honors the physics of the experiment, it leads to a fivefold increase in empty bins. Moreover, although I have cast LSJIMP primarily as a wavefield separation algorithm, recall that one major motivation of integrating multiples and primaries is to use the multiples as a constraint on the primaries in zones where we do not record data. Multiples sample reflectors more finely in reflection angle/offset than do primaries. Moreover, the regularization strategies presented in Section 2.1.3 provide the infrastructure to exploit the inherent multiplicity of signal within an image and between multiple and primary images. Although designed to separate signal and noise, these same strategies also prove adept at interpolating

signal in missing traces.

Stacking velocities were computed by a conventional velocity scan, coupled with maximum amplitude autopicking and local weighted (stack power) mean smoothing. The residual weight, simply zero for missing traces, but one elsewhere, is particularly important to achieve a successful LSJIMP result.

5.2 Results

Figure 5.4 shows stacked sections from the multiple-infested zone of the CGG subset before and after application of LSJIMP. Figure 5.5 is in the same format, but shows a zoom of the multiple-infested region. CMP stacking strongly suppresses the multiples, but from the difference panel, notice that LSJIMP has nonetheless subtracted most of the remaining surface-related multiple energy, and has preserved the stronger primaries to a great extent. The timeslice on the 3-D cube transects the seabed pegleg from reflector R1; it shows up prominently on the raw data stack, as well as on the difference panel, but has been largely suppressed from the LSJIMP estimated primaries stack.

Figures 5.6 and 5.7 illustrate LSJIMP's performance on two individual CMP gathers extracted from different portions of the CGG 3-D data. It is in this domain where the strength of the LSJIMP method shines most. The raw data panels show strong surface-related multiples with an onset of around 4.3 seconds, and also fairly strong primary events under the curtain of multiples. The LSJIMP estimated primaries in panel (b) are effectively free of multiples, and moreover, since the data residual panel (f) barely contains any noticeable flat primary energy, we have preserved the primary events. Also notice that the data residual contains little structured energy. This implies that the LSJIMP forward model accurately models the primaries and important multiples in the data. Unfortunately, much of this "unstructured" energy likely belongs to fairly weak pegleg multiples that simply appear incoherent with the data's poor inline resolution. On Figure 5.7, notice that cable feathering has caused missing traces at far offsets. LSJIMP has used the data's multiplicity and model constraints to reasonably extrapolate the missing traces.

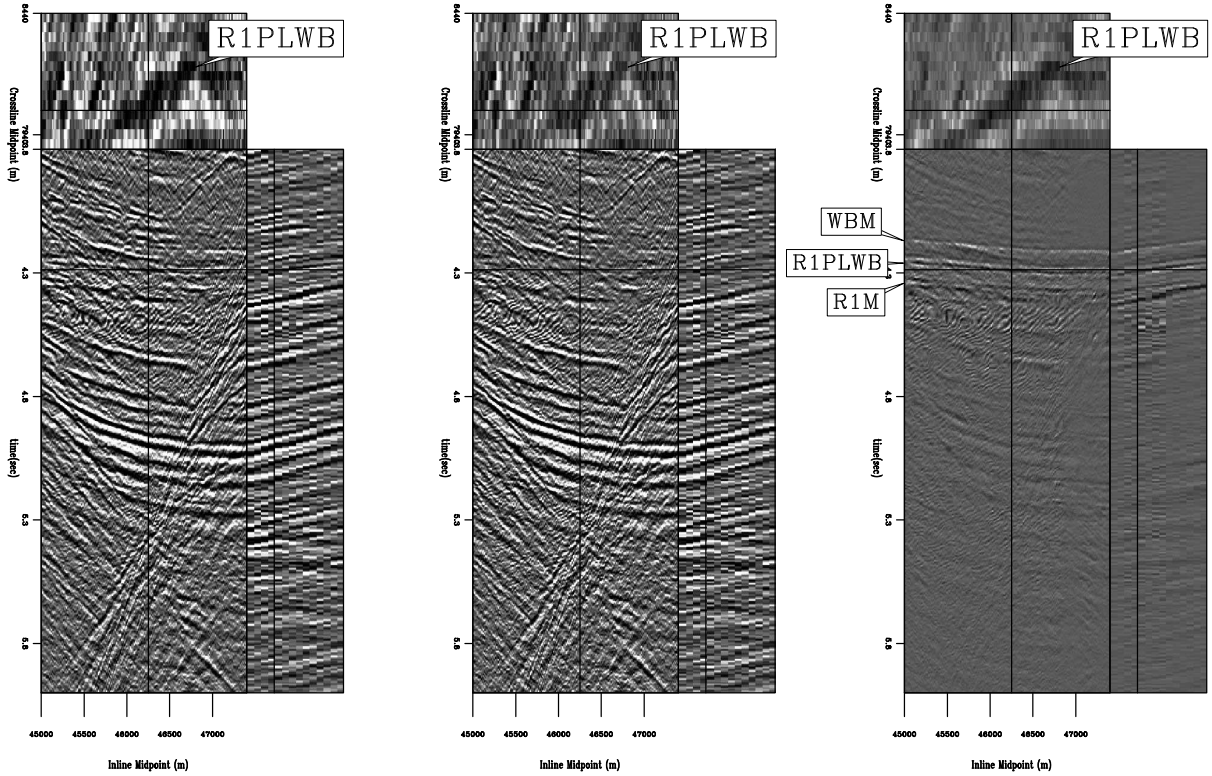

Figure 5.4: Stacked subset (192 midpoints inline, 14 midpoints crossline) of CGG 3-D data before and after LSJIMP. All panels windowed in time from 3.8 to 6.0 seconds and gained with t^2. Left: Raw data stack. Center: Stack of estimated primary image, $\mathbf{m}_0$. Right: Stack of the subtracted multiples. Naming convention for pure first-order multiples: (*reflector*)M, e.g., R1M. Naming convention for first-order pegleg multiples: (*target*)PL(*multiple generator*), e.g., R1PLWB. results3d-stackcomp3d.gc3d [CR,M]

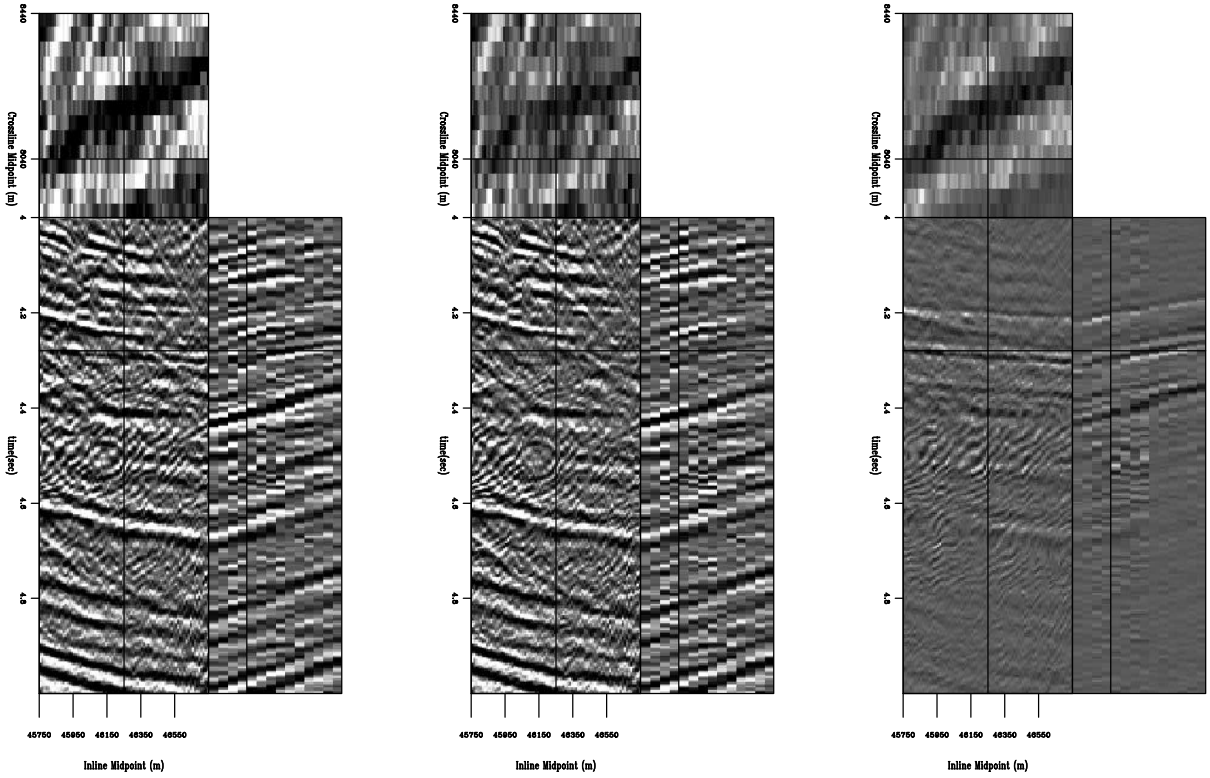

Figure 5.5: Zoom of stacked subset of CGG 3-D data before and after LSJIMP. All panels windowed in time from 4.0 to 5.0 seconds. Left: Raw data stack. Center: Stack of estimated primary image, $\mathbf{m}_0$. Right: Stack of the subtracted multiples. results3d-stackcomp3d.zoom.gc3d [CR,M]

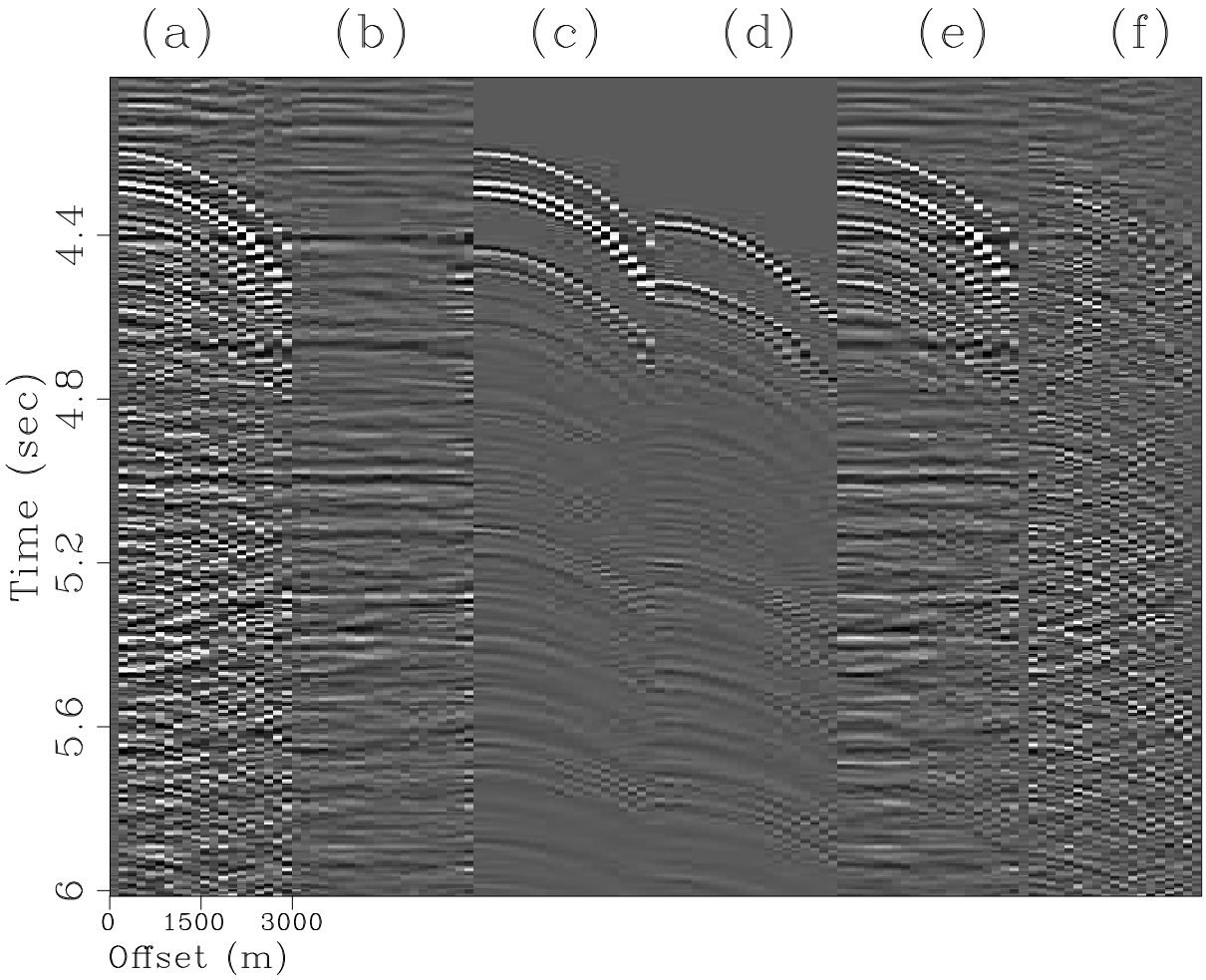

Figure 5.6: LSJIMP results on individual midpoint location (CMPx=100,CMPy=4). All panels decimated in offset by a factor of 6 and NMO'ed with stacking velocity, for display purposes. Panel (a): Raw data. Panel (b): LSJIMP estimated primaries. Panels (c) and (d): Estimated seabed and R1 pegleg multiples. Panel (e): Modeled data (sum of panels (b), (c), and (d)). Panel (f): Data residual (difference of panels (a) and (e)), with residual weight applied. results3d-compwind.lsrow.gc3d.100.4 [CR]

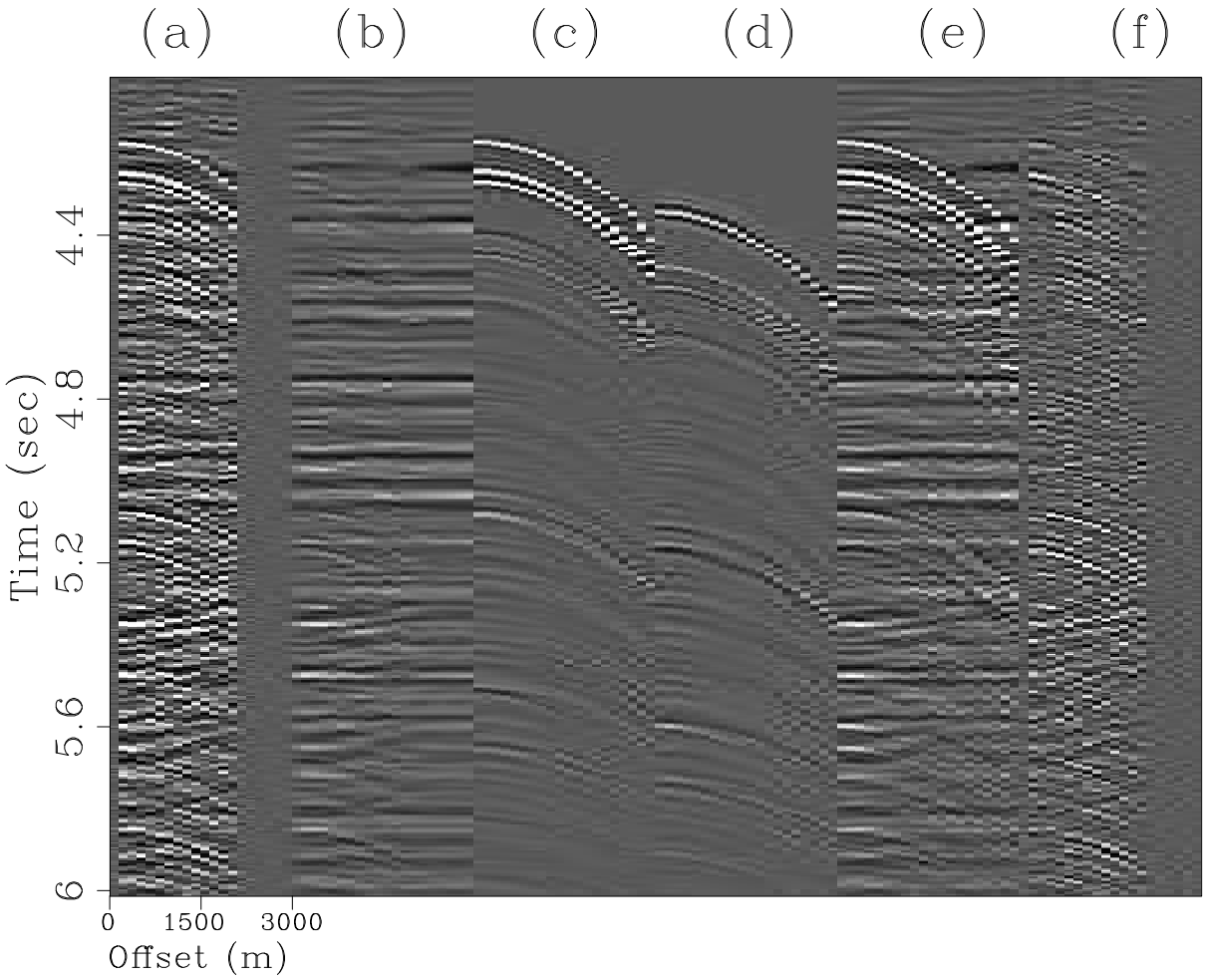

Figure 5.7: LSJIMP results on individual midpoint location (CMPx=100,CMPy=12). All panels decimated in offset by a factor of 6 and NMO'ed with stacking velocity, for display purposes. Panel (a): Raw data. Panel (b): LSJIMP estimated primaries. Panels (c) and (d): Estimated seabed and R1 pegleg multiples. Panel (e): Modeled data (sum of panels (b), (c), and (d)). Panel (f): Data residual (difference of panels (a) and (e)), with residual weight applied. results3d-compwind.lsrow.gc3d.100.12 [CR]

5.2.1 LSJIMP versus Radon Demultiple

Radon demultiple remains the default multiple suppression technique in many situations, particularly in 3-D, where acquisition sparsity may inhibit other techniques. On CMP gathers, primaries and multiples normally have different apparent velocities, and a Radon transform which sums across offset using various curvature parameters will focus the two types of events in different parts of the transform panel. The most natural curvature parameter for CMP data is the velocity of the hyperbola defined by the NMO equation (2.16) (Foster and Mosher, 1992). While the Hyperbolic Radon transform is a linear mapping, it is not time-invariant, and thus cannot be implemented efficiently as a Fourier domain operator. However, a multiple's residual moveout after NMO is approximately parabolic (quadratic) with offset, so a time-invariant Parabolic Radon transform is much faster, though not as accurate (Hampson, 1986; Kabir and Marfurt, 1999).

To remove multiples, the primary energy in the transform panel is muted, and the inverse radon transform applied to produce an estimate of the multiples, which is subtracted from the data to produce a primary estimate. If we define $\mathbf{d}$ as a raw CMP gather, $\mathbf{H}$ as the linear mapping between radon transform space and data space, $\mathbf{M}$ as a mute operator that zeroes primary energy in radon transform space, and $\mathbf{d}_r$ as the estimated primaries, then we can express the radon demultiple process in equation form:

$$\mathbf{d}_r = \mathbf{H}\mathbf{M}^T\mathbf{H}^T\mathbf{d}. \tag{5.1}$$

Operator $\mathbf{H}$ is non-unitary ($\mathbf{H}^T\mathbf{H} \neq \mathbf{I}$), so the amplitude of the estimated primaries will not match the recorded primaries. By casting Radon demultiple as a least-squares optimization problem, the Radon transform panel can be scaled such that $\mathbf{d}_r$ and $\mathbf{d}$ are directly comparable. We first optimize a Radon transform panel, $\mathbf{p}$, to minimize the data misfit:

$$\min_{\mathbf{p}} Q(\mathbf{p}) = \|\mathbf{H}\mathbf{p} - \mathbf{d}\|^2, \tag{5.2}$$

and then apply the mute operator and adjoint of $\mathbf{H}$ to produce the estimated primaries:

$$\mathbf{d}_r = \mathbf{d} - \mathbf{H}\mathbf{M}^T\mathbf{p}. \tag{5.3}$$

The finite frequency content of the data, limited extent of the array, and the intrinsic unresolvability of velocity information at zero offset all contribute to the non-uniqueness of the least-squares Radon demultiple problem. At far offsets, events with many zero-offset traveltimes and different velocities are fit equally well by a single curvature parameter. Low-frequency data makes moveout discrimination between multiples and primaries more difficult. At near offsets, all the events are fit equally well by all curvature parameters. All these pitfalls lead to reduced resolution of events in the Radon domain. So-called "high resolution" least-squares Radon transform implementations partially overcome these problems by imposing sparsity constraints in either the hyperbolic or parabolic Radon domain (Thorson and Claerbout, 1985; Sacchi and Ulrych, 1995).

I implemented and tested least-squares Hyperbolic Radon demultiple (LSHRTD) on the CGG 3-D data subset. I performed 10 conjugate gradient iterations to produce an optimal $\mathbf{p}$, then applied a mute function which is zero for velocities greater than 90% known stacking velocity. The mute tapers linearly from 1.0 to 0.0 between 85% and 90% of the stacking velocity. The computational cost of LSHRTD is very similar to the cost of applying LSJIMP.

Figure 5.8 compares the results of applying LSJIMP and LSHRTD on a single CMP gather from the CGG 3-D data (CMPx=100, CMPy=4). The LSHRTD results are quite good, as we expect, given the high velocity gradient and relatively simple moveout seen in this region of the data. Spatial aliasing causes some artifacts on the LSHRTD primaries (Figure 5.8(b)), around $\tau = 4.4$ seconds. The radon primaries seem to contain a bit more spatially uncorrelated noise than the LSJIMP primaries. LSJIMP is a more "surgical" separation technique, although the model regularization operators also exploit moveout differences to separate multiples and primaries.

Figure 5.9, a stack of the LSHRTD estimated primaries, can be compared directly with the LSJIMP result, Figure 5.5. Like before, the multiples predominantly stack out, since the moveout separation is so significant. Still, a noticeable amount of multiple energy has been removed by LSHRTD, perhaps more than by LSJIMP. However, we immediately see some removed primary energy: for example, the strong primary near the bottom of the section.

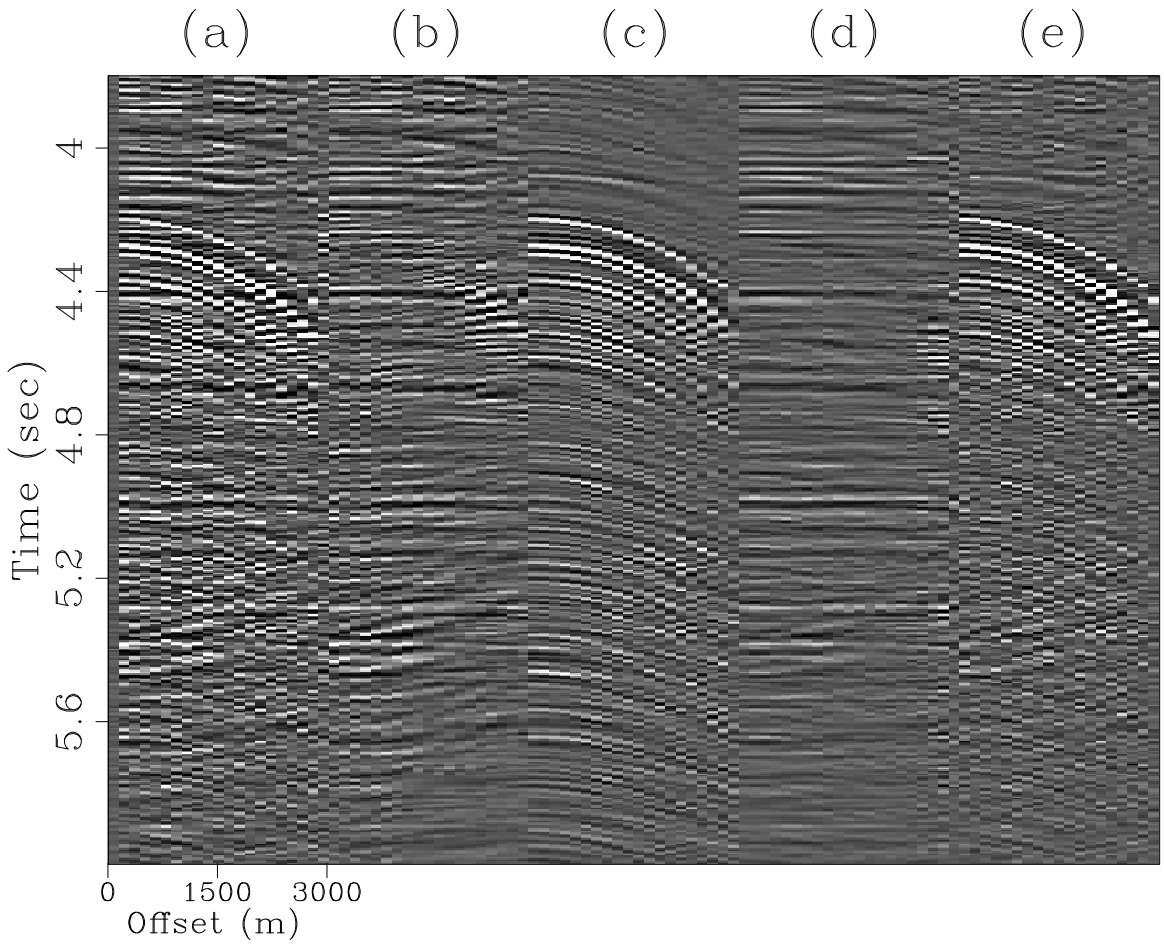

Figure 5.8: LSJIMP versus least-squares Hyperbolic Radon demultiple (LSHRTD) on one CMP gather of the CGG 3-D dataset. Panel (a): Raw data. Panel (b): LSHRTD estimated primaries. Panel (c): LSHRTD estimated multiples. Panel (d): LSJIMP estimated primaries. Panel (e): LSJIMP estimated multiples. results3d-comp.radon.gc3d.100 [CR]

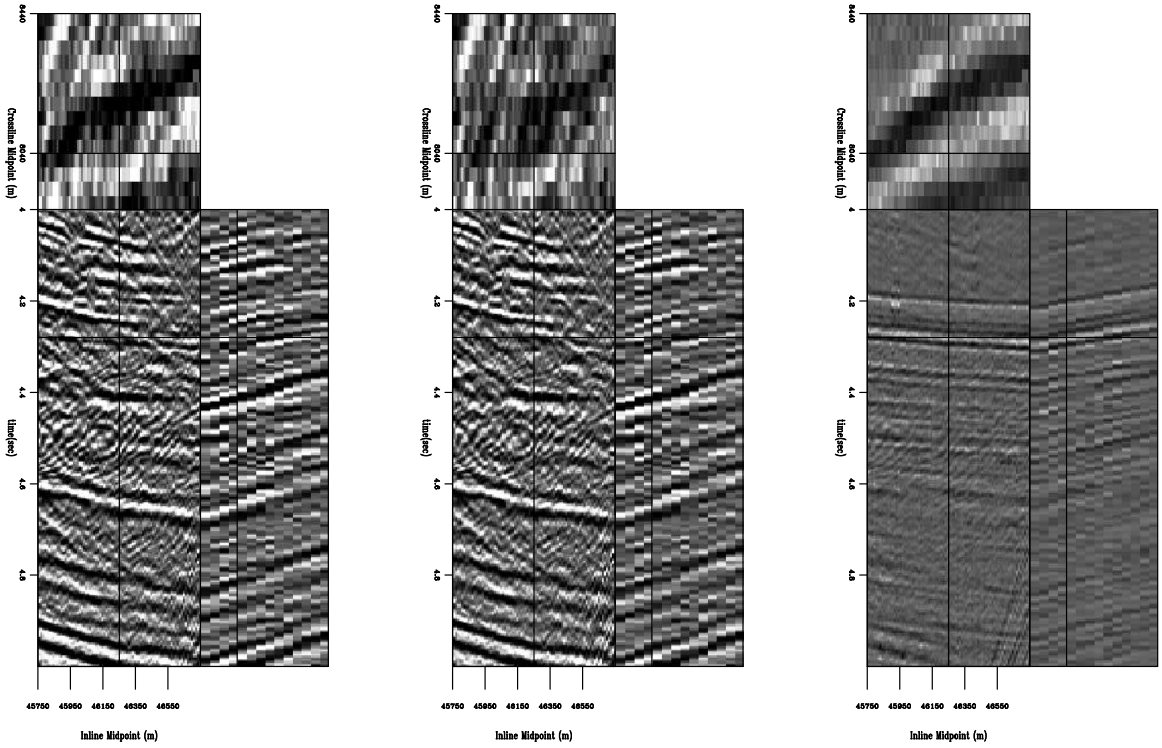

Figure 5.9: NMO/Stack comparison before and after LSHRTD. Compare directly with Figure 5.5. Left: Raw data. Center: LSHRTD estimated primaries. Right: difference. results3d-stackcomp3d.radon.zoom.gc3d [CR,M]

5.2.2 AVO Analysis Before and After LSJIMP

Amplitude-versus-offset or AVO analysis is perhaps the most commonly utilized direct hydrocarbon indicator in exploration reflection seismology today. The stacked results before and after LSJIMP on the Green Canyon 3-D dataset showed that stacking greatly attenuates multiples. However, from the prestack data, we saw that the multiples are prominent, and would surely inhibit signal processing techniques, like AVO analysis, if left intact. In this section, I illustrate how LSJIMP improves the AVO analysis of the Green Canyon 3-D data.

Shuey (1985) showed that in a 1-D earth, the measured reflection strength of an event at the surface is approximately linear with the square of its incidence angle, at angles less than 30 degrees. In a 1-D earth, the NMO equation gives an approximate relationship between offset and incidence angle. Claerbout (1995) defines the "stepout", p, as the spatial derivative of an event's traveltime curve:

$$p = \frac{dt}{dx} = \frac{\sin\theta}{V}, \tag{5.4}$$

where θ is the incidence angle and V is the velocity at the surface; in the marine case, simply water velocity. Stepout was earlier used to derive the Snell Resampling operator in Section 2.2.3. In a 1-D earth, the traveltime curve of a primary reflection is approximately given by the NMO equation (2.16). Taking the derivative of equation (2.16) with respect to offset, then substituting into equation (5.4) gives the following expression for the sine of incidence angle as a function of offset:

$$\sin\theta = \frac{V}{V^2_{\text{rms}}(\tau)} \frac{x}{\sqrt{\tau^2 + \frac{x^2}{V^2_{\text{rms}}(\tau)}}}. \tag{5.5}$$

Reflection data as a function of offset may be mapped to $\sin^2\theta$ via equation (5.5), at which point the AVO "slope" and "intercept" parameters may be estimated, usually via a linear least-squares fit to the data after resampling from offset to $\sin^2\theta$.

Figure 5.10 illustrates the estimation of AVO slope and intercept parameters on a deep reflector in the Green Canyon 3-D data, before and after application of LSJIMP. The reflector, which is well under the multiples in the data, is denoted on the zero offset section with "O" symbols. The maximum amplitude in a small time window around the reflection were picked automatically, and make up the input data to the least-squares estimation.

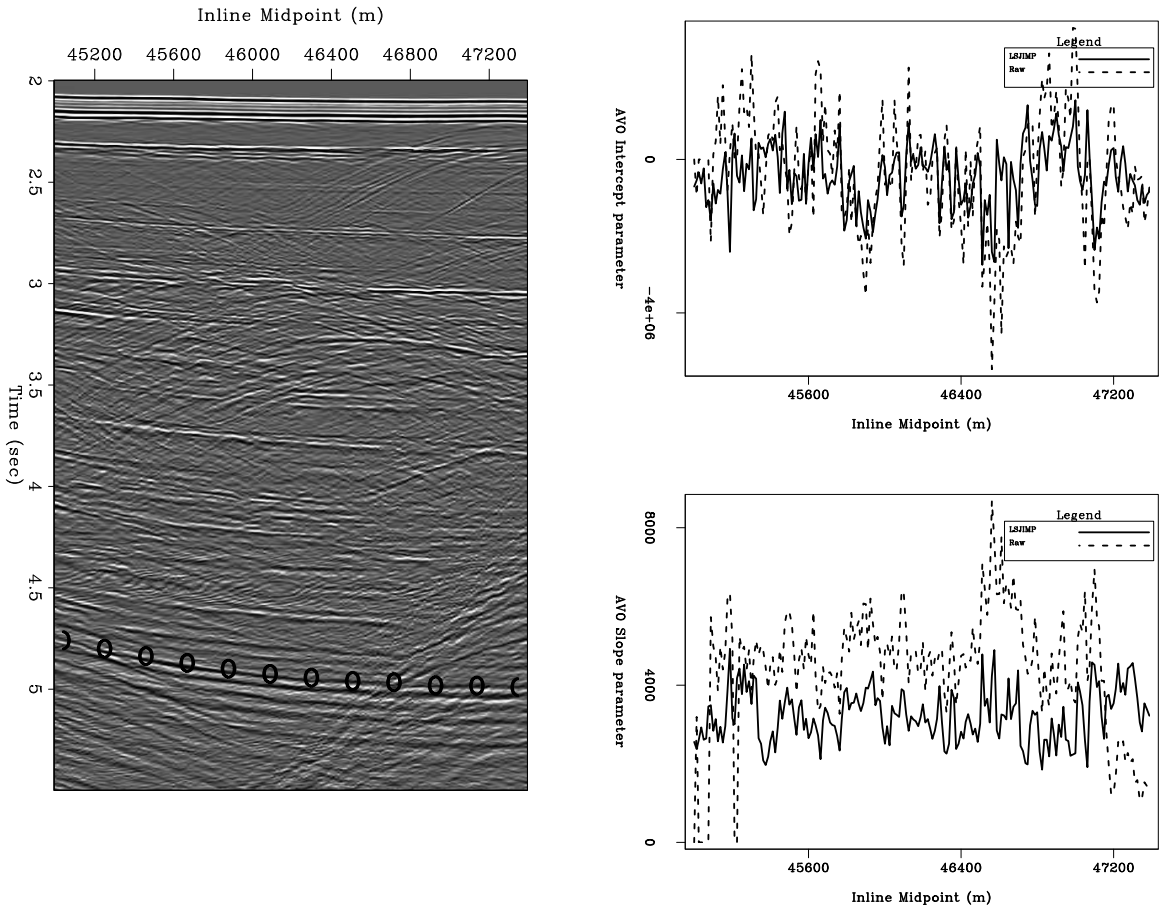

Figure 5.10: AVO parameter estimation for a deep reflector. Left: zero offset section, "O" symbols denote reflector of interest. Right, top: AVO intercept parameter before and after LSJIMP, as a function of midpoint. Right, bottom: AVO slope parameter before and after LSJIMP, as a function of midpoint. results3d-maxampl.gc3d.4-5 [CR]

We see that while the parameter estimates contain the same trends before and after LSJIMP, the LSJIMP result is more consistent and less "noisy" across midpoint. My implementation of LSJIMP works on a CMP-by-CMP basis, so the results shown in Figure 5.10 are not smoothed across midpoint. The similarity across midpoint is an expression of the true lithology – lithology which LSJIMP better reveals.

Figure 5.11 illustrates, as a function of midpoint, the small time windows taken around the deep reflector shown in Figure 5.10, before and after LSJIMP. The input data to an AVO parameter estimation are picked maximum amplitudes within the time window as a function of $\sin^2\theta$. Notice the significant increase in reflector clarity after LSJIMP. Also recall that the data residuals (e.g., in Figures 5.6 and 5.7) are quite small. Therefore, the cleaner reflection events after LSJIMP in Figure 5.11 are not only better for AVO analysis – they also fit the recorded data in a quantitative fashion. LSJIMP is not an *ad hoc* post-processing technique.

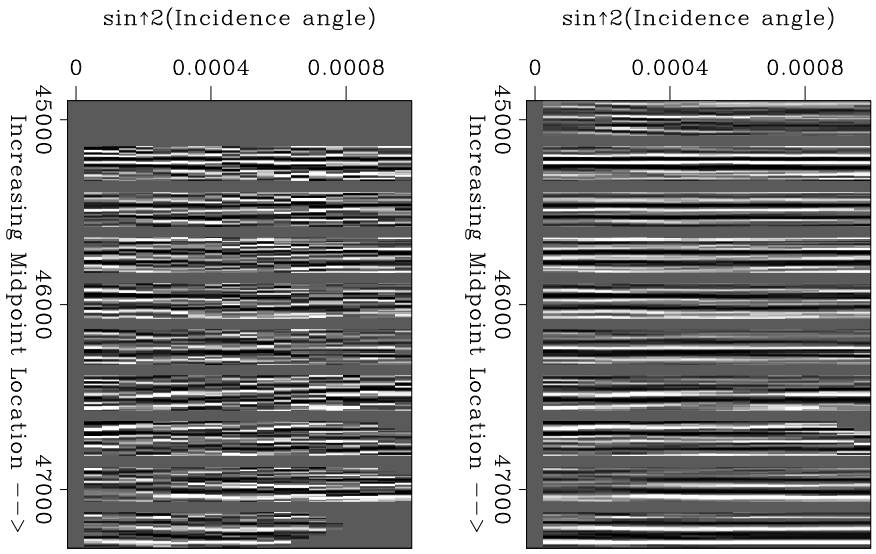

Figure 5.11: Small time windows around the deep reflector shown in Figure 5.10, before and after LSJIMP. Individual panels along the vertical axis correspond to windows taken at different midpoint locations. Left: Data windows before LSJIMP. Right: Data windows after LSJIMP. results3d-avogather.gc3d.4-5 [CR]

Chapter 6

Conclusions

I introduced the LSJIMP method, a general least-squares inversion strategy to solve the problem of how to combine information from multiple and primary images while simultaneously suppressing crosstalk noise on each image. Successful tests on real 2-D and 3-D marine seismic data confirm that LSJIMP holds great promise as a novel and useful tool in the quest for a better seismic image. While my particular implementation of LSJIMP uses a fast, but relatively inaccurate imaging methodology, the continued trend toward inexpensive parallel computing implies that we may soon have the ability to use more accurate (and expensive) prestack imaging operators in LSJIMP.

6.1 Conclusions on basic LSJIMP theory

In the following section, I discuss some potential future issues surrounding the LSJIMP method in general.

- **Which Multiples?** I cast the LSJIMP method in the fashion of explicit multiple imaging, e.g., one order, split, and multiple generator per operator. Implicit multiple imaging techniques like Guitton's (2002) or Shan's (2003) implicitly image all multiples with a reflection at the free surface. While the conceptual simplicity of the implicit methods

is enticing, they have the same problems as the SRME method of multiple modeling. Because the imaging is done by correlating events, each of which has finite bandwidth, the wavelet of the imaged multiple will change, and may complicate the combination of multiple and primary images. Furthermore, the SRME method requires dense area source coverage, which is highly uncommon in today's 3-D marine geometries.

- **Regularization:** The regularization operators presented in section 2.1.3 exploit two forms of signal multiplicity in the image space: that along offset/angle and that between multiple and primary images. An unexplored possibility is to exploit the multiplicity of signal events across nearby midpoints, in the same fashion as Prucha-Clapp and Biondi (2002), by applying a differential operator along the dominant local reflector dip. As those authors showed, however, the quality of the result is sensitive to the prior estimate of reflector dip.

- **Imaging or Inversion in Image Space?** In section 2.1.2, I discussed some requirements for and existing choices of multiple imaging operators. Out of many choices, which is the best? The answer is hardly black and white, and the "correct" answer for one user or application may not suit others. For instance, prestack depth migration produces more accurate imaging results than, for instance, normal moveout or time migration. However, it is widely known that the lack of an accurate depth velocity model negatively affects prestack depth migration. Moreover, in practice, the velocity estimation and depth imaging methods are generally intertwined tightly, and make up the final step before well selection.

  Users may (reasonably) cast LSJIMP as a multiple separation algorithm. LSJIMP outputs a multiple-free estimate of the primaries, which have been enhanced by the inversion. Conventionally, such multiple-free data is a prerequisite to velocity model building and depth migration. Stacking velocities, on the other hand, are available almost at the beginning of the processing flow, so in these situations, users may prefer to use imaging techniques which are less sensitive to velocity, like any method which uses stacking velocity instead of interval velocity.

  One important point to emphasize is this: LSJIMP is an inversion algorithm which operates in *an* image space, not simply an imaging technique or a multiple separation

technique. There are many choices of image space, but the central premises and potential of the LSJIMP method remain strong, regardless of the choice.

6.2 Conclusions on my LSJIMP implementation

In the following section, I discuss issues surrounding my particular implementation of the LSJIMP method.

- **Imaging:** Imaging of peglegs in this paper is this thesis is accomplished by HEMNO. Prestack migration implicitly scans over unknown, arbitrary reflector dips to remove the effects of wave travel between source and receiver. HEMNO is a single-CMP, analytic moveout equation that assumes known (small) reflector dips. While HEMNO may lack the accuracy and generality of high-end prestack migration methods, it retains convincing advantages in speed and memory usage. Still, improved availability of large cluster supercomputers indicates that least-squares migration methods may soon be feasible, even in 3-D.

- **Reflection Coefficient:** My modeling of the reflection coefficient of the multiple generator, outlined in Section 2.2.5, is quite simple: a single coefficient. Measuring and applying a higher-order parameterization of reflection coefficient would not be terribly difficult, but the gains might be negligible. My reflection coefficient estimation algorithm benefits from spatial regularization to filter "noise"; with more parameters, would the smoothing any longer make sense? Also, because LSJIMP is an inversion procedure, the estimated images to some extent will adapt to any unmodeled amplitude variation, though the residual will be biased.

- **Other Amplitude Effects:** Levin and Shah (1977) perform a detailed analysis of such acquisition-related amplitude effects like source directivity and the response of source arrays and receiver arrays. I have not accounted for any of these effects in this thesis, though such corrections may be straightforward to apply, given sufficient knowledge of acquisition parameters. Nontheless, deficiencies in the modeling are to some extent accounted for by the reflection coefficient.

6.3 Conclusions on the 2-D Data Results

In general, the LSJIMP method demonstrated high-quality separation results on the 2-D Mississippi Canyon data example. Primary energy was preserved and nicely uncovered from strong, shallow pegleg multiples. The method lacks somewhat in its ability to adequately model salt-related reflections, kinematically or in terms of their amplitudes. For one, the rugosity of the top of salt reflection negatively affected reflection coefficient estimation, especially since my model of reflection coefficients assumes spatial contuinuity, and thus to imperfect separation of salt-related multiples from the data.

While in some cases HEMNO could accurately model the kinematics of these multiples (see Figures 3.10 and 3.11), in cases where the salt geometry varied too fast spatially, HEMNO's performance suffered. I conclude that for moderate, spatially "smooth" dips, HEMNO works well. Failures point to migration (especially prestack depth migration) techniques to tackle the salt problem.

In section 3.2 I investigated what, if anything, the multiples add to the LSJIMP inversion. The improved separation results obtained after adding the multiples confirmed a central assertion about LSJIMP: the use of multiple reflections in a global inversion add a useful constraint to discriminate between signal and noise.

In section 3.3, I applied the LSJIMP nonlinear updating scheme outlined in section 2.1.8 and found that in particular, poorly-estimated reflection coefficients can be improved by the updating scheme, which in turn leads to improved separation results. However, I found that the result of updating the crosstalk weights was negligible to the separation results.

6.4 Conclusions on the 3-D Data Results

On the CGG Green Canyon 3-D dataset, LSJIMP again demonstrated an excellent ability to separate primaries and multiples. The data subset shown in the thesis came from a sedimentary minibasin, which boasts a simple velocity profile, high signal-to-noise ratio, and fairly mild (but non-trivial) dips. The full dataset released by CGG contains much data recorded over

salt. In preliminary tests on one salt region, NMO and HEMNO proved unable to correctly image primaries or multiples. The salt bodies often exhibit crossline dips of over 30 degrees, which, when combined with the data's inherent sparsity, severely test even the most advanced imaging techniques.

The data subset is particularly well-suited for Radon demultiple, with its large velocity gradient and gentle geology. I tested least-squares hyperbolic Radon demultiple (LSHRTD) and found that LSJIMP compares quite favorably, both in terms of computational efficiency, multiple separation, and amplitude preservation.

The quantitative study of prestack reflection amplitudes in section 5.2.2 confirmed what was suspected; LSJIMP's ability to remove multiples and random noise, as well as its ability to use multiples and other constraints to interpolate missing traces, greatly improve prestack amplitude analysis.

Appendix A

HEMNO Equivalence with Levin and Shah's Equations

In this appendix, I prove that the HEMNO equation is equivalent to Levin and Shah's traveltime equation (Levin and Shah, 1977) in the limit of small dip angle. They show that in a constant velocity medium with dipping target reflector and multiple generator, the moveout equation of the "S102G" pegleg multiple (see Figure 2.3) is:

$$t^2 = \left[\tau^* \cos\theta + \tau \cos\phi\right]^2 + \left[\frac{x\cos(\phi+\theta)}{V} - \tau^* \sin\theta - \tau \sin\phi\right]^2, \tag{A.1}$$

where ϕ and θ are the dip angle (in radians) of the multiple generator and target reflector, respectively. τ^* and τ are the zero-offset traveltimes to the two reflectors, x is offset, and V is the medium velocity. For small dip angles (i.e., less than 5 degrees), we can make the small angle approximation for angles ϕ, θ, and $\phi+\theta$ to update equation (A.1) accordingly:

$$t^2 = \left[\tau^* + \tau\right]^2 + \left[\frac{x}{V} - \tau^*\theta - \tau\phi\right]^2. \tag{A.2}$$

Multiplying out the squares in equation (A.2) and collecting terms gives:

$$t^2 = \left[\tau^* + \tau\right]^2 + \frac{x^2}{V^2} - 2\frac{\theta\tau^* x}{V} - 2\frac{\phi\tau x}{V} + (\tau^*\theta)^2 + (\tau\phi)^2. \tag{A.3}$$

The θ^2 and ϕ^2 terms are negligible for small angles, so we can ignore these terms and further simplify equation (A.3):

$$t^2 = \left[\tau^* + \tau\right]^2 + \frac{x^2}{V^2} - 2\frac{(\theta\tau^* + \phi\tau)x}{V}. \tag{A.4}$$

I will now show that the HEMNO equation (2.27) is equivalent to the Levin/Shah equation (A.1) under the constant velocity and small dip angle assumptions. First I make some preliminary definitions. In a constant-velocity medium, the expression for x_p, equation (2.21), simplifies to:

$$x_p = \frac{\tau}{\tau + \tau^*}x. \tag{A.5}$$

Then $x - x_p$, which will be needed later, simplifies to:

$$x - x_p = \frac{\tau^*}{\tau + \tau^*}x \tag{A.6}$$

Since the reflectors in this derivation are assumed planar and the velocity is assumed constant, using equations (A.5) and (A.6), we can directly write the (two-way) zero offset traveltime to the seabed and subsea reflection at any midpoint as a function of the corresponding zero-offset traveltimes at the midpoint location, y_0:

$$\begin{aligned}
\tau^*(y_0 - x_p/2) &= \tau^*(y_0) - \frac{x_p \sin\phi}{V} \\
&\approx \tau^*(y_0) - \frac{\phi\ \tau(y_0)\ x}{(\ \tau(y_0) + \tau^*(y_0)\ )\ V} \qquad \text{(A.7)} \\
\tau(y_0 - (x - x_p)/2) &= \tau(y_0) - \frac{(x - x_p)\sin\theta}{V} \\
&\approx \tau(y_0) - \frac{\theta\ \tau^*(y_0)\ x}{(\ \tau(y_0) + \tau^*(y_0)\ )\ V}, \qquad \text{(A.8)}
\end{aligned}$$

where the small angle approximation was employed as before. Substituting the zero-offset traveltimes (A.7) and (A.8) into the HEMNO equation (2.27) yields:

$$\begin{aligned}
t^2 &= \left[\tau(y_0) + \tau^*(y_0) - \frac{(\ \phi\ \tau(y_0) + \theta\ \tau^*(y_0)\ )\ x}{(\ \tau(y_0) + \tau^*(y_0)\ )\ V}\right]^2 + \frac{x^2}{V^2} \qquad \text{(A.9)} \\
&\approx \left(\tau(y_0) + \tau^*(y_0)\right)^2 - 2\frac{(\ \phi\ \tau(y_0) + \theta\ \tau^*(y_0)\ )\ x}{V} + \frac{x^2}{V^2}. \qquad \text{(A.10)}
\end{aligned}$$

Equation (A.10) is equivalent to equation (A.4). Therefore, we have proven the equivalence of the moveout equations of the true and approximate raypaths shown in Figure 2.7, subject to the small dip angle approximation. As before, ϕ^2 and θ^2 terms were dropped in going from equation (A.9) to equation (A.10). Although explicit seabed and subsea reflector dip angles, ϕ and θ, are contained in equation (A.10), they were introduced only to show equivalence to equation (A.4). Locally-planar reflectors are not required to implement equation (2.27).

Appendix B

Derivation of Snell Resampling Operator

In the following appendix, I derive the Snell resampling operation, equation (2.21). The graphical basis for the derivation is Figure 2.4. Since the pegleg multiple and primary in the figure have the same emergence angle, θ, the stepout, or spatial derivative, of the traveltime curves of the two events is the same at x and x_p. First we compute the stepout of the primary event, starting from the standard NMO equation:

$$t_p^2 = \tau + \frac{x_p^2}{V^2} \tag{B.1}$$

$$\frac{d}{dx_p}\left(t_p^2\right) = 2t_p\frac{dt_p}{dx_p} = \frac{2x_p}{V^2} \tag{B.2}$$

$$\frac{dt_p}{dx_p} = \frac{x_p}{t_p V^2}. \tag{B.3}$$

Using equations (2.18) and (2.20), we can similarly compute the stepout of the corresponding j^{th}-order pegleg multiple:

$$\frac{dt_m}{dx} = \frac{x}{t_m V_{eff}^2}. \tag{B.4}$$

Finally, we compute x_p as a function of x by squaring equations (B.3) and (B.4), setting them equal, and substituting traveltime equations (2.18) and (B.1) for t_m and t_p, respectively:

$$\frac{x_p^2}{t_p^2 V^4} = \frac{x^2}{t_m^2 V_{eff}^4}. \tag{B.5}$$

$$x^2\left[V^4\tau^2 + x_p^2 V^2\right] = x_p^2\left[V_{eff}^4(\tau + j\tau^*)^2 + x^2 V_{eff}^2\right] \tag{B.6}$$

$$x_p^2 = \frac{x^2\tau^2 V^4}{(\tau + j\tau^*)^2 V_{eff}^4 + x^2(V_{eff}^2 - V^2)}. \tag{B.7}$$

Bibliography

AAPG, 1998, Gulf of mexico petroleum systems: AAPG Bulletin, **82**, no. 5.

Berkhout, A. J., and Verschuur, D. J., 1994, Multiple technology: Part 2, migration of multiple reflections: Soc. of Expl. Geophys., 64th Ann. Internat. Mtg, 1497–1500.

Berkhout, A. J., and Verschuur, D. J., 2003, Transformation of multiples into primary reflections:, *in* 73rd Ann. Internat. Mtg Soc. of Expl. Geophys.

Berryhill, J. R., and Kim, Y. C., 1986, Deep-water peglegs and multiples - Emulation and suppression: Geophysics, **51**, no. 12, 2177–2184.

Biondi, B., and Palacharla, G., 1996, 3-D prestack migration of common-azimuth data: Geophysics, **61**, no. 06, 1822–1832.

Biondi, B., Fomel, S., and Chemingui, N., 1998, Azimuth moveout for 3-D prestack imaging: Geophysics, **63**, no. 02, 574–588.

Biondi, B., 1997, Azimuth moveout + common-azimuth migration: Cost-effective prestack depth imaging of marine data: Soc. of Expl. Geophys., 67th Ann. Internat. Mtg, 1375–1378.

Brown, M., 2002, Simultaneous estimation of two slopes from seismic data, applied to signal/noise separation: SEP–**112**, 181–194.

Claerbout, J. F., 1992, Earth Soundings Analysis: Processing Versus Inversion: Blackwell Scientific Publications.

Claerbout, J. F., 1995, Basic Earth Imaging: Stanford Exploration Project.

Fomel, S., 2001, Three-dimensional seismic data regularization: Ph.D. thesis, Stanford University.

Fomel, S., 2002, Applications of plane-wave destruction filters: Geophysics, **67**, no. 06, 1946–1960.

Foster, D. J., and Mosher, C. C., 1992, Suppression of multiple reflections using the Radon transform: Geophysics, **57**, no. 03, 386–395.

Guitton, A., Brown, M., Rickett, J., and Clapp, R., 2001, Multiple attenuation using a t-x pattern-based subtraction method: Soc. of Expl. Geophys., 71st Ann. Internat. Mtg, 1305–1308.

Guitton, A., 2002, Shot-profile migration of multiple reflections: 72nd Ann. Internat. Mtg., Soc. of Expl. Geophys., Expanded Abstracts, 1296–1299.

Hampson, D., 1986, Inverse velocity stacking for multiple elimination: J. Can. Soc. Expl. Geophys., **22**, no. 01, 44–55.

Hargreaves, N., Wombell, R., and VerWest, B., 2003, Multiple attenuation using an apex-shifted radon transform: 65th Mtg., Eur. Assoc. Geosc. Eng., Workshop: Strategies Towards Multi-Dimensional Multiple Attenuation.

He, R., and Schuster, G., 2003, Least-squares migration of both primaries and multiples:, *in* 73rd Ann. Internat. Mtg Soc. of Expl. Geophys.

Hokstad, K., and Sollie, R., 2003, 3-D surface-related multiple elimination using parabolic sparse inversion:, *in* 73rd Ann. Internat. Mtg Soc. of Expl. Geophys., 1961–1964.

Hutchinson, M., and De Hoog, F., 1985, Smoothing noisy data with spline functions: Smoothing noisy data with spline functions:, Numer. Math., 99–106.

Kabir, M. M. N., and Marfurt, K. J., 1999, Toward true amplitude multiple removal: The Leading Edge, **18**, no. 1, 66–73.

Kleemeyer, G., Pettersson, S., Eppenga, R., Haneveld, C., Biersteker, J., and Den Ouden, R., 2003, It's magic – industry first 3D surface multiple elimination and pre-stack depth migration on Ormen Lange:, *in* 65th Mtg. Eur. Assn. Geosci. Eng., Session:B–43.

Kuehl, H., and Sacchi, M., 2001, Generalized least-squares DSR migration using a common angle imaging condtion: Soc. of Expl. Geophys., 71st Ann. Internat. Mtg, 1025–1028.

Levin, F. K., and Shah, P. M., 1977, Peg-leg multiples and dipping reflectors: Geophysics, **42**, no. 05, 957–981.

Levin, F. K., 1971, Apparent velocity from dipping interface reflections: Geophysics, **36**, no. 03, 510–516.

Levin, S. A., 1996, AVO estimation using surface-related multiple prediction: Soc. of Expl. Geophys., 66th Ann. Internat. Mtg, 1366–1369.

Lomask, J., 2003, Flattening 3D seismic cubes without picking: Soc. of Expl. Geophys., 73rd Ann. Internat. Mtg., 1402–1405.

Lu, G., Ursin, B., and Lutro, J., 1999, Model-based removal of water-layer multiple reflections: Geophysics, **64**, no. 6, 1816–1827.

Morley, L., 1982, Predictive multiple suppression: Ph.D. thesis, Stanford University.

Nemeth, T., Wu, C., and Schuster, G. T., 1999, Least-squares migration of incomplete reflection data: Geophysics, **64**, no. 1, 208–221.

Ottolini, R., 1982, Migration of reflection seismic data in angle-midpoint coordinates: Ph.D. thesis, Stanford University.

Paffenholz, J., 2003, All-azimuth streamer acquisition: the impact on 3D multiple attenuation: 65th Mtg., Eur. Assoc. Geosc. Eng., Workshop: Strategies Towards Multi-Dimensional Multiple Attenuation.

Prucha, M. L., and Biondi, B. L., 2002, Subsalt event regularization with steering filters: 72nd Ann. Internat. Mtg., Soc. of Expl. Geophys., Expanded Abstracts, 1176–1179.

Prucha-Clapp, M., and Biondi, B., 2002, Subsalt event regularization with steering filters: Soc. of Expl. Geophys., 72nd Ann. Internat. Mtg, 1176–1179.

Reiter, E. C., Toksoz, M. N., Keho, T. H., and Purdy, G. M., 1991, Imaging with deep-water multiples: Geophysics, **56**, no. 07, 1081–1086.

Rickett, J., and Lumley, D. E., 2001, Cross-equalization data processing for time-lapse seismic reservoir monitoring: A case study from the Gulf of Mexico: Geophysics, **66**, no. 4, 1015–1025.

Riley, D. C., and Claerbout, J. F., 1976, 2-D multiple reflections: Geophysics, **41**, no. 04, 592–620.

Ross, W. S., Yu, Y., and Gasparotto, F. A., 1999, Traveltime prediction and suppression of 3-D multiples: Geophysics, **64**, no. 1, 261–277.

Sacchi, M. D., and Ulrych, T. J., 1995, High-resolution velocity gathers and offset space reconstruction: Geophysics, **60**, no. 04, 1169–1177.

Sava, P., and Fomel, S., 2000, Angle-gathers by Fourier Transform: SEP–**103**, 119–130.

Sava, P., and Fomel, S., 2003, Angle-domain common-image gathers by wavefield continuation methods: Geophysics, **68**, no. 3, 1065–1074.

Shan, G., 2003, Source-receiver migration of multiple reflections:, *in* 73rd Ann. Internat. Mtg Soc. of Expl. Geophys.

Shuey, R. T., 1985, A simplification of the Zoeppritz-equations: Geophysics, **50**, no. 04, 609–614.

Stoffa, P. L., Fokkema, J. T., de Luna Freire, R. M., and Kessinger, W. P., 1990, Split-step Fourier migration: Geophysics, **55**, no. 4, 410–421.

Taner, M. T., and Koehler, F., 1969, Velocity spectra - Digital computer derivation and applications of velocity functions: Geophysics, **34**, no. 06, 859–881.

Taner, M. T., 1980, Long-period sea-floor multiples and their suppression: Geophys. Prosp., **28**, no. 01, 30–48.

Tarantola, A., 1984, Inversion of seismic reflection data in the acoustic approximation: Geophysics, **49**, no. 08, 1259–1266.

Thorson, J. R., and Claerbout, J. F., 1985, Velocity stack and slant stochastic inversion: Geophysics, **50**, no. 12, 2727–2741.

Tsai, C. J., 1985, Use of autoconvolution to supress first-order long-period multiples: Use of autoconvolution to supress first-order long-period multiples:, Soc. of Expl. Geophys., Geophysics, 1410–1425.

Ursin, B., 1990, Offset-dependent geometrical spreading in a layered medium (short note): Geophysics, **55**, no. 04, 492–496.

van Borstelen, R., 2003, Optimization of marine data acquisition for the application of 3D SRME:, *in* 73rd Ann. Internat. Mtg Soc. of Expl. Geophys., 1965–1968.

van Dedem, E., and Verschuur, D., 2002, 3D surface-related multiple prediction using sparse inversion: experience with field data: Soc. of Expl. Geophys., 72nd Ann. Internat. Mtg, 2094–2097.

Verschuur, D. J., Berkhout, A. J., and Wapenaar, C. P. A., 1992, Adaptive surface-related multiple elimination: Geophysics, **57**, no. 09, 1166–1177.

Wang, J., Kuehl, H., and Sacchi, M. D., 2003, Least-squares wave-equation avp imaging of 3D common azimuth data:, *in* 73rd Ann. Internat. Mtg Soc. of Expl. Geophys.

Wang, Y., 2003, Multiple subtraction using an expanded multichannel matching filter: Geophysics, **68**, no. 1, 346–354.

Wiggins, J. W., 1988, Attenuation of complex water-bottom multiples by wave equation-based prediction and subtraction: Geophysics, **53**, no. 12, 1527–1539.

Yu, J., and Schuster, G., 2001, Crosscorrelogram migration of IVSPWD data: Soc. of Expl. Geophys., 71st Ann. Internat. Mtg, 456–459.